

HARVARD UNIVERSITY
Graduate School of Arts and Sciences



DISSERTATION ACCEPTANCE CERTIFICATE

The undersigned, appointed by the
Department of Physics
have examined a dissertation entitled

Getting Out Of A Tight Spot: Physics Of Flow Through Porous Materials

presented by Sujit Sankar Datta

candidate for the degree of Doctor of Philosophy and hereby
certify that it is worthy of acceptance.

Signature

Typed name: Professor David Weitz, Chair

Signature

Typed name: Professor David Nelson

Signature

Typed name: Professor James Rice

Date: September 4, 2013

Getting Out Of A Tight Spot: Physics Of Flow Through Porous Materials

A dissertation presented
by

Sujit Sankar Datta

to
The Department of Physics

in partial fulfillment of the requirements
for the degree of
Doctor of Philosophy
in the subject of
Physics

Harvard University
Cambridge, Massachusetts

September 2013

UMI Number: 3600154

All rights reserved

INFORMATION TO ALL USERS

The quality of this reproduction is dependent upon the quality of the copy submitted.

In the unlikely event that the author did not send a complete manuscript and there are missing pages, these will be noted. Also, if material had to be removed, a note will indicate the deletion.



UMI 3600154

Published by ProQuest LLC (2013). Copyright in the Dissertation held by the Author.

Microform Edition © ProQuest LLC.

All rights reserved. This work is protected against unauthorized copying under Title 17, United States Code



ProQuest LLC.
789 East Eisenhower Parkway
P.O. Box 1346
Ann Arbor, MI 48106 - 1346

©2013 - Sujit Sankar Datta

All rights reserved.

Getting Out Of A Tight Spot: Physics Of Flow Through Porous Materials

Abstract

We study the physics of flow through porous materials in two different ways: by directly visualizing flow through a model three-dimensional (3D) porous medium, and by investigating the deformability of fluid-filled microcapsules having porous shells.

In the first part of this thesis, we develop an experimental approach to directly visualize fluid flow through a 3D porous medium. We use this to investigate drainage, the displacement of a wetting fluid from a porous medium by a non-wetting fluid, as well as secondary imbibition, the subsequent displacement of the non-wetting fluid by the wetting fluid. We characterize the intricate morphologies of the non-wetting fluid ganglia left trapped within the pore space, and show how the ganglia configurations vary with the wetting fluid flow rate. We then visualize the spatial fluctuations in the fluid flow, both for single- and multi-phase flow. We use our measurements to quantify the strong variability in the flow velocities, as well as the pore-scale correlations in the flow. Finally, we use our experimental approach to study the simultaneous flow of both a wetting and a non-wetting fluid through a porous medium, and elucidate the flow instabilities that arise for sufficiently large flow rates.

In the second part of this thesis, we study the mechanical properties of porous spherical microcapsules. We first introduce emulsions, and describe how their rheology depends on the microscopic interactions between the drops comprising them. We then study the formation and buckling of one class of microcapsule – nanoparticle-coated emulsion drops.

Abstract

We also use double emulsions, drops within drops, as templates to form another class of microcapsule – drops coated with thin, porous, polymer shells. We investigate how, under sufficient osmotic pressure, these microcapsules buckle, and show how the inhomogeneity in the shell structure can guide the folding pathway taken by a microcapsule as it buckles. Finally, we study the expansion and rupture of microcapsules under the influence of electrostatic forces. For both buckling and expansion, we show that the deformation dynamics can be understood by coupling shell theory with Darcy's law for flow through the porous microcapsule shell.

Contents

Title Page	i
Abstract	iii
Table of Contents	v
Citations to Previously Published Work	vii
Acknowledgments	x
Dedication	xii
1 Introduction	1
1.1 Visualizing flow through a model 3D porous medium	1
1.2 Deformations of porous microcapsules	3
2 Experimental approach to visualizing multi-phase flow in a three-dimensional porous medium	5
2.1 Preparation of the medium	6
2.2 Formulating refractive index-matched fluids	6
2.3 3D visualization using confocal microscopy	8
2.4 Measurement of permeability	9
3 Drainage in a three-dimensional porous medium	10
3.1 Drainage in a homogeneous porous medium	12
3.2 Drainage in a stratified porous medium	16
4 Imbibition in a three-dimensional porous medium	26
4.1 Pore-scale dynamics of secondary imbibition	28
4.2 Trapped oil ganglia configurations	32
4.3 Physics of ganglion mobilization	38
5 Spatial fluctuations of fluid velocities in flow through a three-dimensional porous medium	45
5.1 Visualizing single-phase flow	46
5.2 Quantifying correlations in the flow	51
5.3 Visualizing multi-phase flow	55

6 Fluid breakup during simultaneous two-phase flow through a three-dimensional porous medium	58
6.1 Visualizing multi-phase flow	60
6.2 Understanding the fluid breakup	64
6.3 State diagram for the connected-to-broken up transition	67
7 Rheology of emulsions	71
7.1 Formulation of emulsions	73
7.2 Frequency-dependent mechanical response	75
7.3 Strain-dependent mechanical response	77
7.4 Time scales of the structural relaxation	84
8 Buckling and crumpling of nanoparticle-coated droplets	89
8.1 Formulation of Pickering emulsions	91
8.2 Volume-controlled morphological transitions	92
8.3 Size-dependent morphologies	98
9 Buckling of inhomogeneous microcapsules	105
9.1 Microcapsule fabrication	107
9.2 Onset of microcapsule buckling	113
9.3 Dynamics of microcapsule buckling	116
9.4 Shell inhomogeneities guide microcapsule deformations	122
10 Expansion and rupture of pH-responsive microcapsules	126
10.1 Microcapsules composed solely of a pH-responsive polymer	128
10.2 Hybrid microcapsules	133
Bibliography	141

Citations to Previously Published Work

Most of Chapters 2-10 are based on the following papers:

Chapters 2, 3, and 4:

“Visualizing multi-phase flow and trapped fluid configurations in a model three-dimensional porous medium”,
A. T. Krummel*, **S. S. Datta***, S. Munster, and D. A. Weitz,
AIChE Journal 59, 1022 (2013) *Equal contribution.

Chapter 3:

“Drainage in a model stratified porous medium”,
S. S. Datta and D. A. Weitz, *EPL* 101, 14002 (2013).

Chapters 3 and 4:

“Mobilization of a trapped non-wetting fluid from a three-dimensional porous medium”,
S. S. Datta, T. S. Ramakrishnan, and D. A. Weitz, to be submitted (2013).

Chapter 5:

“Spatial fluctuations of fluid velocities in flow through a three-dimensional porous medium”,
S. S. Datta, T. S. Ramakrishnan, and D. A. Weitz,
Physical Review Letters 111, 064501 (2013).

Chapter 6:

“Fluid breakup during simultaneous two-phase flow through a three-dimensional porous medium”,
S. S. Datta, J. B. Dupin, and D. A. Weitz, to be submitted (2013).

Chapter 7:

“Rheology of attractive emulsions”,
S. S. Datta, D. D. Gerrard, T. S. Rhodes, T. G. Mason, and D. A. Weitz,
Physical Review E, 84, 041404 (2011).

Citations to Previously Published Work

Chapter 8:

“Controlled buckling and crumpling of nanoparticle-coated droplets”,
S. S. Datta, H. C. Shum, and D. A. Weitz, *Langmuir*, 26, 18612 (2010).

Chapter 9:

“Controlling release from double emulsion-templated microcapsules”,
S. S. Datta*, A. Abbaspourrad*, E. Amstad, J. Fan, S-H Kim, M. Romanowsky,
H. C. Shum, B. J. Sun, A. S. Utada, M. Windbergs, S. Zhu, and D. A. Weitz,
to be submitted (2013) *Equal contribution.

Chapter 9:

“Delayed buckling and guided folding of inhomogeneous capsules”,
S. S. Datta*, S-H Kim*, J. Paulose*,
A. Abbaspourrad, D. R. Nelson, and D. A. Weitz,
Physical Review Letters 109, 134302 (2012) *Equal contribution.

Chapter 10:

“Expansion and rupture of pH-responsive microcapsules”,
S. S. Datta*, A. Abbaspourrad*, and D. A. Weitz,
submitted, *Materials Horizons* (2013) *Equal contribution.

Chapter 10:

“Controlling release from pH-responsive microcapsules”,
A. Abbaspourrad*, **S. S. Datta***, and D. A. Weitz,
submitted, *Langmuir* (2013) *Equal contribution.

Citations to other work co-authored during the course of the degree, not included in this thesis:

“Thermally switched release from nanoparticle colloidosomes”,
S. Zhu*, J. Fan*, **S. S. Datta**, X. Guo, M. Guo, and D. A. Weitz,
in press, *Advanced Functional Materials* (2013) *Equal contribution.

“Ultrathin shell double emulsion-templated giant unilamellar lipid vesicles
with controlled microdomain formation”,
L. R. Arriaga, **S. S. Datta**, S. H. Kim, E. Amstad,
T. E. Kodger, F. Monroy, and D. A. Weitz, submitted, *Small* (2013).

Citations to Previously Published Work

“Microfluidic fabrication of stable gas-filled microcapsules for acoustic contrast enhancement”,
A. Abbaspourrad*, W. J. Duncanson*, N. Lebedeva, S. H. Kim, A. Zhushma,
S. S. Datta, S. S. Sheiko, M. Rubinstein, and D. A. Weitz,
in press, *Langmuir* (2013) *Equal contribution.

“Controlling the morphology of polyurea microcapsules using microfluidics”,
I. Polenz, **S. S. Datta**, and D. A. Weitz, to be submitted (2013).

“The microfluidic arrayed-post device: high throughput production of viscous single drops”,
E. Amstad, **S. S. Datta**, and D. A. Weitz, to be submitted (2013).

“Wetting and energetics in nanoparticle etching of graphene”
S. S. Datta, *Journal of Applied Physics* 108, 024307 (2010).

Acknowledgments

I am lucky to have had the opportunity to interact with so many amazing people during the course of my Ph.D.

First and foremost, Dave. Thank you for introducing me to the semicolon. More importantly, thank you for teaching me how to think. I will always have your voice in my head, pushing me to be the best scientist and person I can be. Your energy and creativity will always be an inspiration as I constantly ask myself: what would Dave do?

Dave always says that if he's the only professor you interact with at Harvard, you're wasting your time. I've learned so much from a number of other professors: David Nelson, Jim Rice, Howard Stone, L. Mahadevan, Michael Brenner, Zhigang Suo, and John Hutchinson. Thank you all for taking the time to educate me and for putting up with my constant questions. I am especially grateful to Professors Nelson and Rice for taking the time to be on my thesis committee and provide enormous amounts of support.

The Weitz lab is a fantastic place to do science, and I would like to thank all the Weitz labbers with whom I've interacted over the years. I am particularly grateful to Ali Abbaspourrad, Esther Amstad, Tommy Angelini, Laura Arriaga, Oni Basu, Harry Chiang, Wynter Duncanson, Jean-Baptiste Dupin, Dustin Gerrard, Erin Hannen, Shin-Hyun Kim, Dorota Koziej, Amber Krummel, Tina Lin, Peter Lu, Anderson Shum, Joris Sprakel, Jim and Connie (and Claire!) Wilking, Huidang Zhang, and undoubtedly many other equally deserving people whose names just aren't coming to my sleep-deprived mind right now, for exciting collaborations, interesting discussions, or just making life in the lab so much more fun. I would also like to thank Laura for taking the time to go through and comment on this thesis. And Peter, for always keeping things interesting, and for inspiring the title of this thesis.

Acknowledgments

I've had a ton of fun discussing science with a number of people outside of the Weitzlab, as well: Jayson Paulose, Tom Mason, and Alberto Fernandez-Nieves. I have also benefited tremendously from fantastic collaborations and discussions with the researchers down the street at Schlumberger-Doll Research: T. S. Ramakrishnan, Jeff Paulsen, Dave Johnson, Yi-Qiao Song, and Martin Hurlimann.

Finally, I'd like to thank all of my friends for enriching my life. I would particularly like to thank the crew at Redline Fight Sports, who maintained my sanity and taught me how to be resilient by letting me beat them up (or beating me up) on a regular basis. And of course, my family, for always loving and supporting me.

Somewhere, something incredible is waiting to be known.

-Carl Sagan

Chapter 1

Introduction

1.1 Visualizing flow through a model 3D porous medium

Filtering water, squeezing a wet sponge, and brewing coffee are all familiar examples of forcing a fluid through a porous medium. This process is also crucial to many technological applications, including geological flows, the operation of packed bed reactors, chromatography, fuel cells, chemical release from colloidal capsules, and even nutrient transport through mammalian tissues [1, 2, 3, 4, 5, 6, 7]. Such flows, when sufficiently slow, are typically modeled using Darcy's law, $\Delta p = \mu q L / k$, where μ is the fluid dynamic viscosity and k is the absolute permeability of the porous medium; this law relates the pressure drop Δp across a length L of the entire medium to the flow velocity q , averaged over a sufficiently large length scale. However, while appealing, this simple continuum approach does not explicitly treat local pore-scale variations in the flow, which may arise as the fluid navigates the tortuous 3D pore space of the medium. Such flow variations can have significant practical consequences; for example, they may result in spatially heterogeneous solute

transport through a porous medium. This impacts diverse situations ranging from the drying of building materials [8], to biological flows [6, 9, 7], to geological tracer monitoring [1]. Moreover, many situations, such as groundwater aquifer remediation, geological CO₂ sequestration, oil recovery, and the operation of trickle bed reactors, involve the flows of *multiple* immiscible fluids [1]. This imparts further complexity to the flow. For example, the multi-phase flow can lead to the formation, trapping, or mobilization of discrete ganglia of a non-wetting fluid within the porous medium [10, 11, 12, 13, 14, 15, 16, 17, 18]. This phenomenon is particularly relevant to oil recovery, where over 90% of the oil within a reservoir can remain trapped after primary recovery. Understanding the physics of flow through a 3D porous medium, on scales ranging from that of an individual pore to the scale of the entire medium, is therefore both intriguing and important.

Some of this complex flow behavior can be visualized in two-dimensional (2D) micromodels [14, 19]; however, a complete understanding of the physics underlying the formation and trapping of ganglia requires experimental measurements on 3D porous media [16, 20, 13, 21]. Optical techniques typically cannot be used to directly image the flow through such media due to the light scattering caused by the differences in the indices of refraction between the different fluid phases and the solid material making up the medium itself. Instead, magnetic resonance imaging (MRI) [22, 23] and X-ray micro computer tomography (X-ray μ CT) [24, 25, 26, 27] have been used to visualize either the bulk flow dynamics, or some pore-scale behavior, within 3D porous media; however, fast visualization, both at pore-scale resolution and over the scale of the entire medium, is typically challenging. While theoretical models and numerical simulations provide crucial additional insight [28, 29, 30, 31, 32, 33, 34, 35, 36, 37, 1, 38, 39, 40], fully describing the disordered

structure of the medium can be challenging. Consequently, despite its enormous practical importance, a complete understanding of flow within a 3D porous medium remains elusive.

In the first part of this thesis, we report an approach to visualize single- and multi-phase flow through a model 3D porous medium, at scales ranging from that of individual pores to that of the entire medium. We first describe the experimental approach [Chapter 2]. We use this approach to investigate drainage, the displacement of a wetting fluid from a porous medium by a non-wetting fluid [Chapter 3], as well as secondary imbibition, the subsequent displacement of the non-wetting fluid by the wetting fluid [Chapter 4]. We characterize the intricate morphologies of the non-wetting fluid ganglia left trapped within the pore space, and show how the ganglia configurations vary with the wetting fluid flow rate. We then visualize the spatial fluctuations in the fluid flow, both for single- and multi-phase flow [Chapter 5]. We use our measurements to quantify the strong variability in the flow velocities, as well as the pore-scale correlations in the flow. Finally, we use our experimental approach to study the simultaneous flow of both a wetting and a non-wetting fluid through a porous medium [Chapter 6], and elucidate the flow instabilities that arise for sufficiently large flow rates.

1.2 Deformations of porous microcapsules

A microcapsule is a micrometer-scale liquid drop surrounded by a solid shell; because this shell acts as a barrier separating the core from the external environment, microcapsules are promising candidates for encapsulating and controllably releasing many important active materials. These include surfactants for enhanced oil recovery [41], agricultural chemicals [42, 43, 44, 45, 46, 47], food additives [48, 49, 50, 51], pharmaceuticals

[52, 53, 54, 55, 56, 57, 58, 59, 60, 61], cosmetic components [62, 63, 64, 65, 66], cells [67, 68, 69, 70, 71, 72], biochemical sensors [73, 74, 75, 76], catalysts for chemical reactions [77, 78], restorative agents for self-healing materials [79, 80], inks for carbonless copy paper [81], and electronic inks [82, 83, 84]. These applications often require microcapsules to have unique mechanical properties, such as the ability to withstand large deformations. Thus, studies of the mechanical properties of microcapsules are essential. Because microcapsule shells are often porous, understanding their deformations requires an understanding of fluid flow through them.

In the second part of this thesis, we investigate the deformability of fluid-filled spherical microcapsules having porous shells. We first introduce emulsions, and describe how their rheology depends on the microscopic interactions between the drops comprising them [Chapter 7]. We then describe the formation and mechanical instabilities of one class of microcapsule: nanoparticle-coated emulsion drops [Chapter 8]. We also describe how double emulsions, drops within drops, can also be used to template the formation of microcapsules with precisely-controlled geometries [Chapter 9]. We investigate how, under sufficient osmotic pressure, these microcapsules buckle [Chapter 10], and show how the inhomogeneity in the shell structure can guide the folding pathway taken by the microcapsule as it buckles. Finally, we study the expansion and rupture of microcapsules under the influence of electrostatic forces [Chapter 11]. For both buckling and expansion, we show that the deformation dynamics can be understood by coupling shell theory with Darcy's law for flow through the porous microcapsule shell.

Chapter 2

Experimental approach to visualizing multi-phase flow in a three-dimensional porous medium

In this Chapter¹, we describe the experimental approach by which we visualize single- and multi-phase flow through a model 3D water-wet porous medium. We match the refractive indices of the wetting fluid, the non-wetting oil, and the porous medium; this enables us to directly image the structure of the medium, and the multi-phase flow within it, in 3D using confocal microscopy.

¹Based on “Visualizing multi-phase flow and trapped fluid configurations in a model three-dimensional porous medium”, A. T. Krummel*, S. S. Datta*, S. Munster, and D. A. Weitz, *AICHE Journal* 59, 1022 (2013) *Equal contribution.

2.1 Preparation of the medium

We prepare rigid 3D porous media by lightly sintering [85] densely-packed hydrophilic glass beads, with polydispersity $\approx 4\text{--}6\%$, in thin-walled rectangular quartz capillaries [schematic in Figure 2.1]; these have cross-sectional areas $A \approx 1 \text{ mm} \times 1 \text{ mm}$, $1 \text{ mm} \times 3 \text{ mm}$, $2 \text{ mm} \times 2 \text{ mm}$, or $3 \text{ mm} \times 3 \text{ mm}$. The beads have average radius $a = 19, 32, 36, 60$, or $75 \mu\text{m}$, and the packings have lengths $L \sim 1 - 30 \text{ mm}$. The media thus have lateral dimensions ranging from approximately 7 to several hundred beads.

2.2 Formulating refractive index-matched fluids

Scattering of light from the interfaces between the wetting and non-wetting fluids, as well as from the interfaces between the fluids and the beads, typically precludes direct observation of the multi-phase flow in 3D. We overcome these limitations by matching the refractive indices of the wetting fluid, the non-wetting oil, and the beads, enabling full visualization of the multi-phase flow in 3D [86, 87, 88, 89, 90, 91].

We formulate two different wetting fluids of differing viscosities: the less viscous is a mixture of 91.4 wt% dimethyl sulfoxide and 8.6 wt% water, while the more viscous is a mixture of 82 wt% glycerol, 12 wt% dimethyl sulfoxide, and 6 wt% water. The viscosities are $\mu_w = 2.7 \text{ mPa s}$ or $\mu_w = 110 \text{ mPa s}$, respectively, as measured using a strain-controlled rheometer, and the densities are $\rho_w \approx 1.1 \text{ g cm}^{-3}$ or $\rho_w \approx 1.2 \text{ g cm}^{-3}$, respectively. To visualize the wetting fluid using confocal microscopy, we add 0.01 vol% fluorescein dye buffered at pH = 7.2. We formulate another non-wetting fluid comprised of a mixture of aromatic and aliphatic hydrocarbon oils, obtained from Cargille Labs. This fluid is undyed,

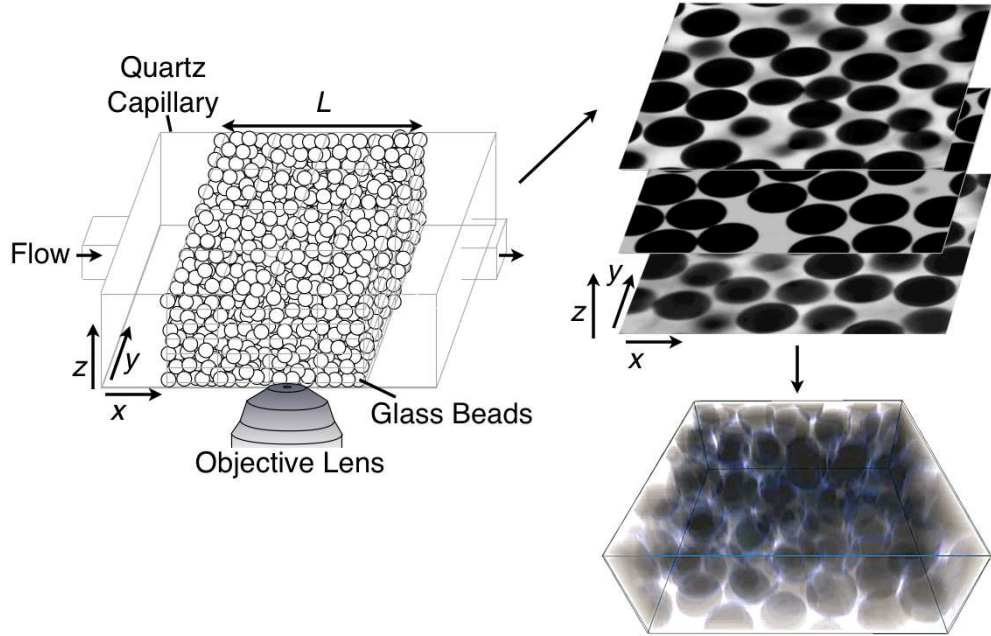


Figure 2.1: Overview of the experimental approach. (Left) Schematic illustrating the structure of a typical 3D porous medium and imaging of flow within it using confocal microscopy. (Top Right) Three optical slices, of thickness $2.0 \mu\text{m}$ and lateral area $912 \mu\text{m} \times 912 \mu\text{m}$, taken at three different depths within a medium comprised of beads with average radius $a = 75 \mu\text{m}$. The medium has been saturated with dyed wetting fluid; the black circles show the beads, while the bright space in between shows the imaged pore volume. (Bottom Right) 3D reconstruction of a porous medium comprised of beads with average radius $a = 75 \mu\text{m}$, with cross-sectional area $910 \mu\text{m} \times 910 \mu\text{m}$; the image shows the reconstruction of a section $350 \mu\text{m}$ high for clarity.

has a viscosity $\mu_{nw} = 16.8 \text{ mPa s}$, and a density $\rho_{nw} \approx 0.8 \text{ g cm}^{-3}$. The interfacial tension between the wetting and non-wetting fluids is $\gamma \approx 13.0 \text{ mN m}^{-1}$, as measured using a du Noüy ring; this value is similar to the interfacial tension between crude oil and water [92]. We use confocal microscopy to estimate the three-phase contact angle made between the wetting fluid and a clean glass slide in the presence of the non-wetting fluid, $\theta \approx 5^\circ$.

2.3 3D visualization using confocal microscopy

We exploit the close match between the refractive indices of the fluorescently-dyed wetting fluid and the glass beads to visualize the structure of the porous medium in 3D. Prior to each experiment, the porous medium is evacuated under vacuum and saturated with CO₂ gas; this gas is soluble in the wetting fluid, preventing the formation of any trapped gas bubbles. We then fill the medium with the fluorescently-dyed wetting fluid by imbibition; a similar approach is used to saturate a rock core prior to core-flood experiments. We use a confocal microscope to image an optical slice, either 2 μm , 7 μm , or 11 μm thick, spanning a lateral area of 912 $\mu\text{m} \times 912 \mu\text{m}$ within the medium, and identify the glass beads by their contrast with the dyed wetting fluid, as exemplified by the slices shown in Figure 2.1. To visualize the pore structure in 3D, we acquire a 3D image stack of multiple slices, each spaced by several micrometers along the z direction, within the porous medium, as shown in 2.1. We use these slices to reconstruct the 3D structure of the medium [Figure 2.1]. The packing of the beads is disordered; to quantify the porosity, ϕ , of this packing, we integrate the fluorescence intensity over all slices making up a stack. To visualize the pore structure of the entire medium, we acquire additional stacks, at the same z positions, but at multiple xy locations spanning the entire width and length of the medium. We find $\phi = 41 \pm 3\%$ independent of position along the length of the medium, as shown in Figure 2.2; this is comparable to the porosity of highly porous sandstone [93]. Moreover, ϕ is similar for different realizations of a porous medium, as shown by the different symbols in Figure 2; this illustrates the reproducibility of our protocol.

We repeatedly acquire these image stacks during the multi-phase flow. The non-wetting oil is undyed; we thus visualize its flow using its additional contrast in the measured pore

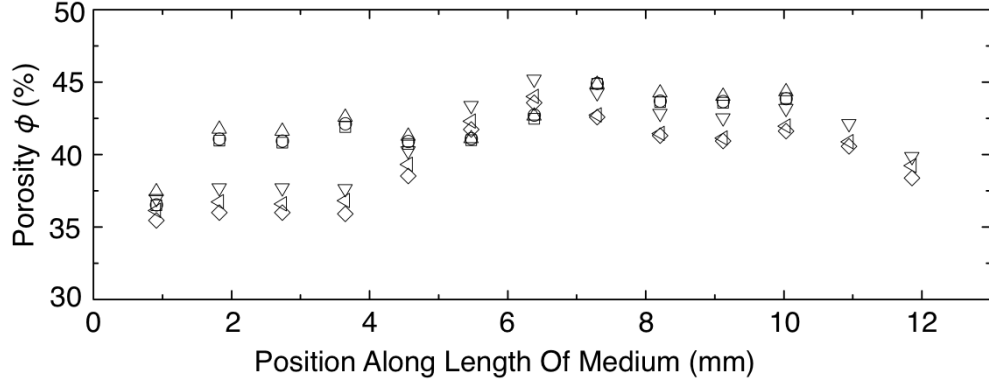


Figure 2.2: **Porosity ϕ of porous media is the same for different positions and realizations.** We find $\phi = 41 \pm 3\%$ at multiple positions along the length of the porous media, and for different porous media prepared in the same way (different symbols).

volume. Moreover, in some cases, we take movies of multiple optical slices, acquired at the same xyz position, with ~ 10 ms time resolution.

2.4 Measurement of permeability

To quantify the bulk transport behavior, we use differential pressure sensors to measure the pressure drop ΔP across a porous medium. We saturate the medium with the wetting fluid and vary the volumetric flow rate Q_w over the range $\sim 0.2 - 50$ mL h $^{-1}$; by measuring the proportionate variation in ΔP , we determine the single-phase permeability of the medium, $k \equiv \mu_w(Q_w L/A)/\Delta P$; for example, for a medium composed of $a = 19$ μm radius beads in a capillary with cross-sectional area $A = 9$ mm 2 , we measure $k = 1.67$ μm^2 . The permeability of a disordered packing of monodisperse spheres is typically estimated using the Kozeny-Carman relation, $k = \frac{1}{45} \frac{\phi^3 a^2}{(1-\phi)^2}$ [94]; this yields $k = 1.59$ μm^2 , in excellent agreement with our measured value.

Chapter 3

Drainage in a three-dimensional porous medium

One important class of multi-phase flow is drainage, the displacement of a wetting fluid from a porous medium by an immiscible non-wetting fluid. To displace the wetting fluid from a pore, the pressure in the non-wetting fluid at the pore entrance must exceed the pressure in the wetting fluid, as schematized in Figure 3.1; this pressure difference is given by $P_\gamma \sim \gamma/a_t$, where γ is the interfacial tension between the fluids and a_t is the radius of the pore entrance [95, 96, 97]. For a homogeneous porous medium, characterized by pores of a single average size, P_γ is typically much larger than the viscous pressure associated with flow into a pore, $\sim \mu_{nw}(Q_{nw}/\phi A)/a_t$, where μ_{nw} is the viscosity of the non-wetting fluid, Q_{nw} is the imposed volumetric flow rate of the non-wetting fluid, A is the medium cross-sectional area, and ϕ is the medium porosity. Consequently, the flow path taken during drainage depends primarily on the slight pore-scale variations of a_t [98, 99, 100, 101, 102]. However, many porous media are stratified, consisting of parallel strata characterized by

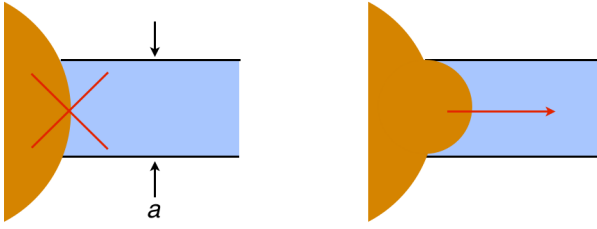


Figure 3.1: Schematic showing invasion of a pore by the non-wetting fluid, shown in orange. The pore is initially filled with the wetting fluid, shown in blue. If the non-wetting fluid pressure is too small, the fluid interface is not sufficiently curved, and the non-wetting fluid does not invade the pore (left). If the non-wetting fluid exceeds a threshold, the curvature of the fluid interface is sufficient for the non-wetting fluid to invade the pore, displacing the wetting fluid in the process (right).

different average pore sizes [1, 103, 104]. Such additional variation in the pore structure, on scales much larger than a single pore, may strongly modify the flow behavior [105, 106, 107, 108, 109, 110, 111, 101]. Despite its enormous practical importance, a clear picture of how the subtle interplay between capillary and viscous forces determines the flow through a 3D stratified porous medium remains elusive. This requires direct visualization of the multi-phase flow, both at the scale of the individual pores and the overall strata. Unfortunately, the medium opacity typically precludes such visualization. As a result, knowledge of how exactly drainage proceeds within a stratified porous medium is missing.

In this Chapter², we use confocal microscopy to investigate drainage within a 3D porous medium. We first study drainage within a homogeneous porous medium. We then study drainage within a heterogeneous porous medium having parallel strata oriented along the flow direction. For the heterogeneous case, we find that for sufficiently small capillary

²Based on “Drainage in a model stratified porous medium”, S. S. Datta and D. A. Weitz, *EPL* 101, 14002 (2013), “Mobilization of a trapped non-wetting fluid from a three-dimensional porous medium”, S. S. Datta, T. S. Ramakrishnan, and D. A. Weitz, to be submitted (2013), and “Visualizing multi-phase flow and trapped fluid configurations in a model three-dimensional porous medium”, A. T. Krummel*, S. S. Datta*, S. Munster, and D. A. Weitz, *AIChE Journal* 59, 1022 (2013) *Equal contribution.

numbers, Ca , the non-wetting fluid flows only through the coarsest stratum of the medium. By contrast, above a threshold Ca , the non-wetting fluid is also forced laterally into part of the adjacent, finer strata. By balancing the viscous pressure driving the flow with the capillary pressure required to invade a pore, we show how both the threshold Ca and the spatial extent of the invasion depend on the pore sizes, cross-sectional areas, lengths, and relative positions of the strata. Our results thus help elucidate how the path taken by the non-wetting fluid is altered by stratification in a 3D porous medium.

3.1 Drainage in a homogeneous porous medium

To mimic the migration of a non-wetting fluid into a homogeneous geological formation, we first drain a homogeneous 3D porous medium [schematized in Figure 3.2(a)], initially saturated with the dyed low-viscosity wetting fluid, with the undyed non-wetting oil at a volumetric flow rate $Q_{nw} = 1 \text{ mL h}^{-1}$. To quantify the competition between the viscous and capillary forces at the pore scale, we calculate the corresponding capillary number, $Ca \equiv \mu_{nw}(Q_{nw}/A)/\gamma \sim 4.0 \times 10^{-5}$. This definition of Ca frequently occurs in the literature, and we therefore use it in this and the next Chapter to facilitate comparison between our results and previous work. However, we note that a more accurate representation of the viscous force would also incorporate the medium porosity ϕ : the ratio of the viscous and capillary pressures then scales as $\frac{\mu_{nw}(Q_{nw}/\phi A)/a_t}{\gamma/a_t} = \mu_{nw}(Q_{nw}/\phi A)/\gamma$ instead. We use this more accurate definition of Ca in Chapter 6.

For $Ca \sim 4.0 \times 10^{-5}$, the oil displaces the wetting fluid through a series of intermittent, abrupt bursts into the pores; this indicates that a threshold capillary pressure difference must build up in the oil before it can invade a pore [112]. This pressure is given by $2\gamma \cos \theta / a_t$,

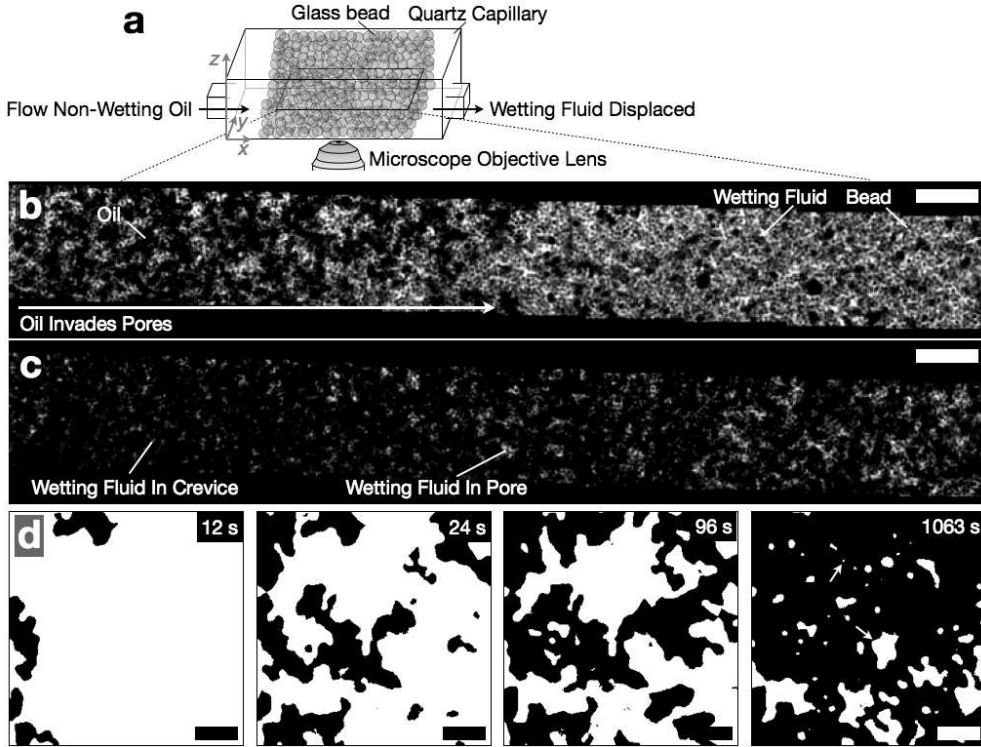


Figure 3.2: Visualizing drainage within a 3D porous medium (a) Schematic of experimental setup. We directly visualize the flow within the medium using confocal microscopy. The pore space is initially saturated with the fluorescently-dyed wetting fluid, which is displaced by the undyed non-wetting oil. (b) Optical section through part of the medium, taken as the oil displaces the wetting fluid at $Q_{nw} = 1 \text{ mL h}^{-1}$. Section is obtained at a fixed z position, away from the lateral boundaries of the medium. Bright areas show the pore space, saturated with the fluorescently-dyed wetting fluid, and the black circles show cross-sections of the beads making up the medium. Additional black areas show the invading oil. The path taken by the oil varies spatially, as seen in the region spanned by the arrow. (c) Optical section through the same part of the medium, taken after invasion by ≈ 9 pore volumes of the oil. Some wetting fluid remains trapped in the crevices and pores of the medium, as indicated. (d) Time sequence of zoomed confocal micrographs, with the pore space subtracted; binary images thus show oil in black as it bursts into the pores. Time stamp indicates time elapsed after subtracted frame. Upper and lower arrows in the last frame show wetting fluid trapped in a crevice or in a pore, respectively. Scale bars in (b-c) and (d) are $500 \mu\text{m}$ and $200 \mu\text{m}$, respectively. Imposed flow direction in all images is from left to right.

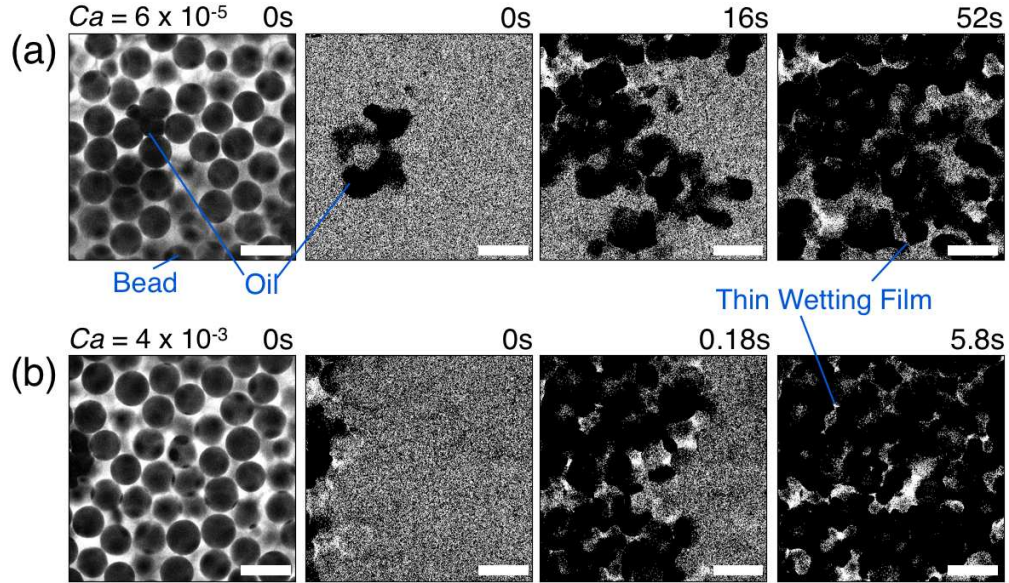


Figure 3.3: Pore-scale dynamics of drainage depend strongly on Ca . Images show multiple frames, taken at different times, of a single optical slice. The slice is $11 \mu\text{m}$ thick and is imaged within a porous medium comprised of beads with average radius $a = 75 \mu\text{m}$, with cross-sectional width 3 mm and height 1 mm . The first frame in each sequence shows the imaged pore space, saturated with dyed wetting fluid; the dark circles are the beads, while the additional dark areas show the invading undyed oil. The beads, and the saturated pore space in between them, are subtracted from the subsequent frames in each sequence; thus, the dark areas in the subsequent frames only show the invading oil. Direction of bulk oil flow is from left to right. The final frame shows the unchanging steady state. Labels show time elapsed after first frame. (a) At low $Ca = 6 \times 10^{-5}$, the oil menisci displace the wetting fluid through a series of abrupt bursts into the pores, and the invading fluid interface is ramified over the scale of multiple pores. (b) At high $Ca = 4 \times 10^{-3}$, the oil bursts occur simultaneously, and the invading fluid interface is more compact over the scale of multiple pores. In both cases, we observe a $\sim 1 \mu\text{m}$ -thick layer of the wetting fluid coating the bead surfaces after oil invasion, indicated in the last frame of each sequence. Scale bars are $200 \mu\text{m}$.

where $a_t \approx 0.16a$ is the typical radius of a pore entrance, a is the average bead radius, and θ is the three-phase contact angle [14, 97, 96, 113, 114]. The bursts are typically only one pore wide [115], but can span many pores in length along the direction of the local flow [third frame of Figure 3.3(a)]; moreover, the oil remains continually connected during flow. Because the packing of the beads is disordered, a_t varies from pore to pore, forcing the path taken by the invading oil to similarly vary spatially, as exemplified by the optical sections in Figures 3.2(b, d) and 3.3 [98, 100, 99, 101, 102]. Consequently, the interface between the oil and the displaced wetting fluid interface is ramified [tip of the arrow in Figure 3.2(b)].

As the oil continues to drain the medium, it eventually fills most of the pore space, as shown in Figure 3.2(c); however, the smallest pores remain filled with the wetting fluid [rightmost indicator in Figure 3.2(c) and lower arrow in Figure 3.2(d)]. Thin layers of the wetting fluid, $\approx 1 \mu\text{m}$ thick, remain trapped in the crevices of the medium, surrounding the oil in the pores [shown by the leftmost indicator in Figure 3.2(c), the upper arrow in Figure 3.2(d), and the indicator in Figure 3.3(a)]; because we use optical imaging, we can resolve this layer to within hundreds of nanometers. This observation provides direct confirmation of the predictions of a number of theoretical calculations and numerical simulations [14, 116, 117, 118, 17, 119, 120, 121, 122, 123, 124, 125, 18, 126].

As the oil bursts into a pore at a speed v , it displaces the wetting fluid, initially contained within the pore, over a length l through the porous medium. This length can be estimated by balancing the threshold capillary pressure, approximately $2\gamma/a_t$, with the viscous pressure required to displace the wetting fluid over the length l , approximately $\mu_w \phi v l/k$, where μ_w is the viscosity of the wetting fluid and k is the medium permeability; this yields $l \approx (2\gamma k)/(\mu_w \phi v a_t)$. Our experimental approach enables us to directly visual-

ize, and quantify the speed of, individual bursts. For a porous medium with $a = 75 \mu\text{m}$, $k = 75 \mu\text{m}^2$, $\phi = 0.41$, and cross-sectional width $w = 3 \text{ mm}$, we measure a maximum burst speed $v \approx 10 \text{ mm s}^{-1}$; this corresponds to wetting fluid flow over $l \approx (2\gamma k)/\mu_w \phi v a_t \sim 10 \text{ mm}$. While the details of this flow are complex, this simple scaling estimate suggests that the wetting fluid is displaced over a length scale comparable to the width of the porous medium, spanning many pores in size; this observation is consistent with previous measurements of pressure fluctuations during drainage [127], as well as imaging of drainage through a monolayer of glass beads [128].

To explore the dependence of the water displacement on flow conditions, we visualize the drainage for varying Ca . Unlike the low Ca case, the oil bursts are not successive during drainage at higher values of $Ca \sim 10^{-4} - 10^{-2}$; instead, neighboring bursts occur simultaneously, typically in the bulk flow direction [Figure 3.3(b)]. As a result, over the scale of multiple pores, the interface between the invading oil and the wetting fluid is more compact; this behavior reflects the increasing contribution of the viscous pressure in the invading oil at higher Ca [98, 129, 128]. As in the low Ca case, we do not observe evidence for oil pinch off or subsequent reconnection; interestingly, this behavior is in contrast to the prediction that the oil can be pinched off during drainage [130, 131, 132]. Similar to the low Ca case, we observe a $\sim 1 \mu\text{m}$ thick layer of the wetting fluid coating the bead surfaces after oil invasion [18, 15, 133, 17], as indicated in the rightmost panels of Figure 3.3.

3.2 Drainage in a stratified porous medium

To create stratified porous media, we arrange the beads into parallel strata characterized by different bead sizes and the same length L ; the interface between the strata runs along

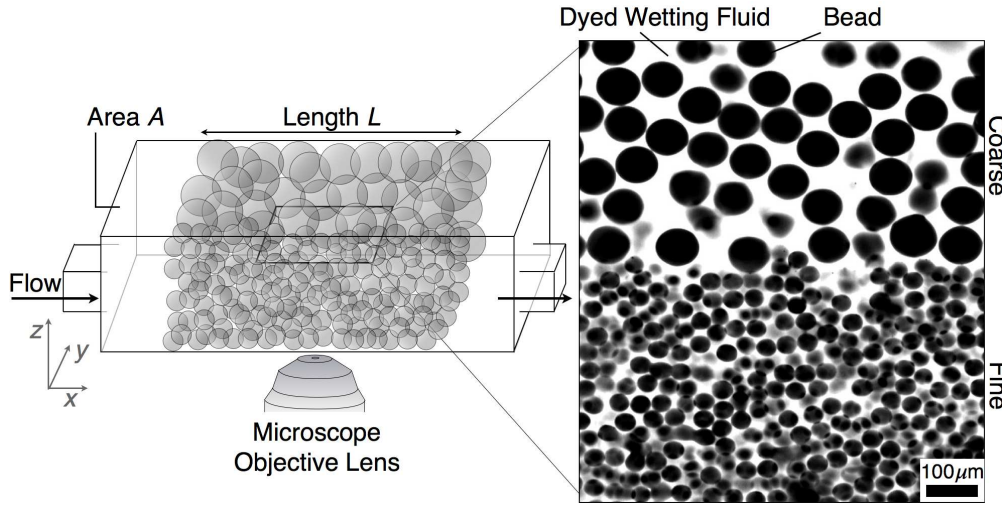


Figure 3.4: Geometry of a stratified 3D porous medium. (Left) Schematic of a stratified porous medium, with parallel strata comprised of differently-sized beads. (Right) Optical section acquired within a porous medium with a coarse and a fine stratum; the pore space is saturated with the fluorescently-dyed wetting fluid, and the black circles show cross sections of the beads making up the medium.

the direction of fluid flow. The effect of stratification on the flow behavior is exemplified by flowing the non-wetting oil through a wetting-fluid saturated porous medium with a coarse and a fine stratum, comprised of beads with radius $a_c = 38 \mu\text{m}$ and $a_f = 19 \mu\text{m}$, respectively [Figure 3.4]. The medium has length $L = 4.2 \text{ mm}$ and a total cross-sectional area $A = 1 \text{ mm}^2$; the coarse stratum occupies an area $A_c = 0.44A$. We flow the oil at a constant rate $Q_{nw} = 0.2 \text{ mL h}^{-1}$, corresponding to a capillary number $Ca = 7.2 \times 10^{-5}$. Similar to the case discussed in the previous section, the oil invades the medium through a series of abrupt bursts into the pores, indicating that a threshold capillary pressure must build up in the oil before it can invade a pore. Interestingly, the oil flows *exclusively* through the coarse stratum, as shown by the optical slice in Figure 3.5(a), over an observation time of 30 min.

To further explore the drainage process, we increase the oil flow rate to $Q_{nw} = 0.3 \text{ mL h}^{-1}$, corresponding to $Ca = 1.1 \times 10^{-4}$. Surprisingly, in contrast to the $Ca = 7.2 \times 10^{-5}$ case, the oil invades the fine stratum, although only partially, over a limited distance, L_f , from the inlet, as shown in Figure 3.5(b). After an unchanging steady state is reached, we flow the oil at even higher flow rates and probe the resulting steady state invasion patterns. Interestingly, the fine stratum remains only partially invaded for the entire range of Ca explored; however, we find that L_f increases with increasing Ca , as shown in Figure 3.5(b-c). This observation contradicts the idea that the fine stratum is completely impervious to the oil [134].

To quantify the partial oil invasion into the fine stratum, we integrate the fluorescence intensity in the fine stratum along both the y and z directions, for each position x . Two examples, corresponding to the invasion patterns shown in Figure 3.5(b) and (c), are shown by the upper and lower traces in Figure 3.5(d), respectively. To determine the distance invaded by the oil into the fine stratum, L_f , we apply a low-pass filter to these data and determine the distance from the inlet to the inflection point of each filtered curve [points in Figure 3.5(d)]. Consistent with the optical slices shown in Figure 3.5(b-c), we find that L_f increases steadily with increasing Ca , as shown in the inset to Figure 3.8.

To understand this complex flow behavior, we analyze the distribution of pressures in the oil as it displaces the wetting fluid. For the oil to invade a pore formed by beads of radius a , the capillary pressure at the oil-wetting fluid interface must exceed $P_\gamma = 2\gamma \cos \theta / a_t$, where $a_t \approx 0.16a$ [96, 97, 135, 136]. The capillary pressure required to invade a pore of the coarse stratum, $P_{\gamma,c} \sim 1/a_c$, is thus smaller than that required to invade a pore of the fine stratum, $P_{\gamma,f} \sim 1/a_f$; consequently, we expect the coarse stratum to be drained first. This

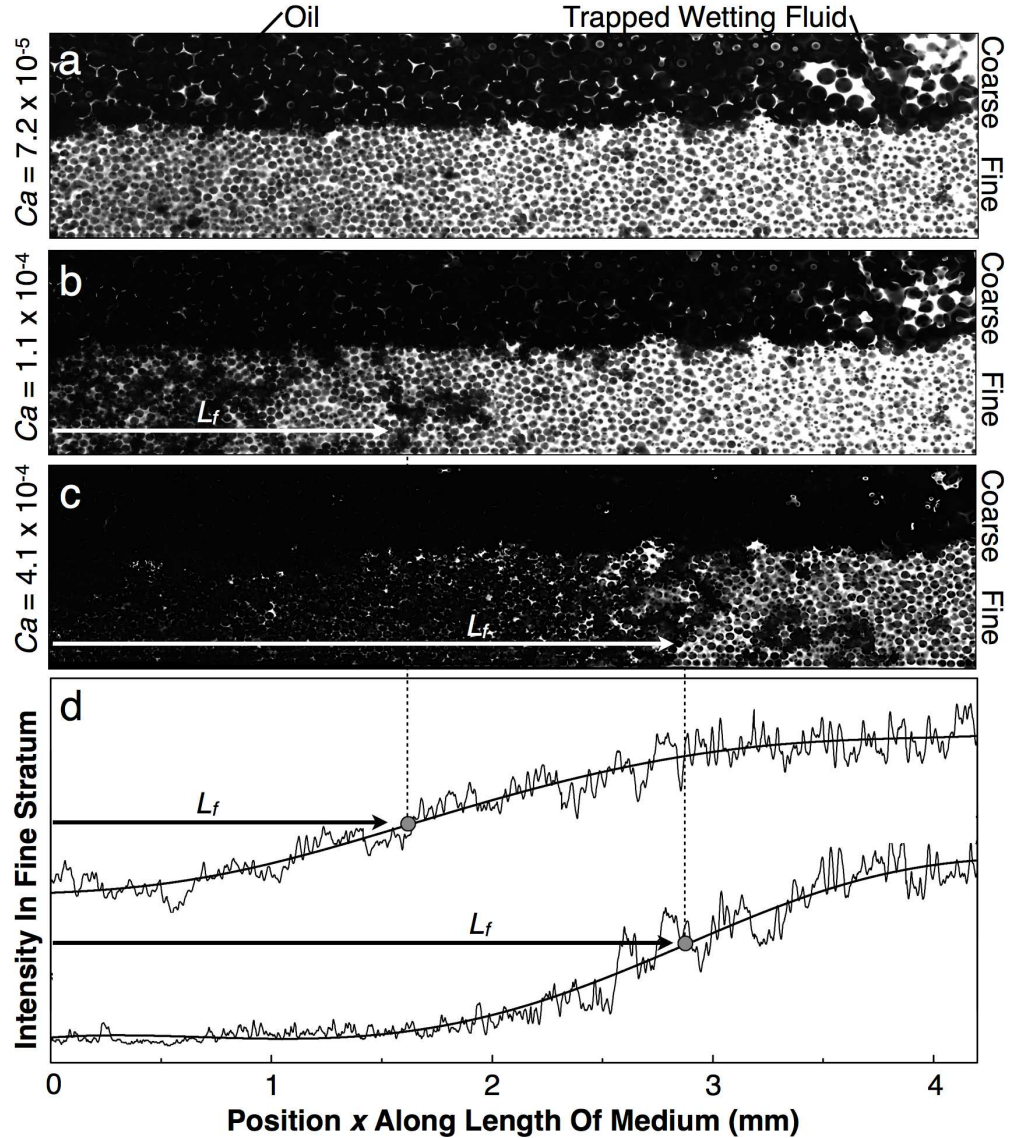


Figure 3.5: Optical sections through an entire porous medium with a coarse and a fine stratum, obtained after flow has reached an unchanging steady state. Imposed flow direction is from left to right. (a) Oil flows exclusively through the coarse stratum for $Ca = 7.2 \times 10^{-5}$; (b-c) oil also invades part of the fine stratum, up to a length L_f from the inlet, for $Ca = 1.1 \times 10^{-4}$ and 4.1×10^{-4} , respectively. The pore space is initially saturated with the fluorescently-dyed wetting fluid; black circles are the beads comprising the medium, while additional black fluid is the invading oil. Inlet is at position $x = 0$. (d) Fluorescence intensity in the fine stratum, integrated along y and z , as it varies with x for $Ca = 1.1 \times 10^{-4}$ and 4.1×10^{-4} as shown by the top and bottom traces, respectively. Smooth curves show filtered data, and arrows show distance invaded by the oil L_f , determined from the inflection points of the curves. The two traces, and corresponding curves, are vertically shifted for clarity.

expectation is in direct agreement with the observed drainage behavior, shown in Figure 3.5(a).

An additional viscous pressure, P_v , drives the continued flow of oil through the coarse stratum; we use Darcy's law to estimate this as $P_v(x) = \mu_o(Q/A_c)(L-x)/k_c$. We estimate the permeability of the coarse stratum to the oil, k_c , using the Kozeny-Carman relation $k_c \approx \frac{\kappa}{45} \frac{\phi^3}{(1-\phi)^2} a_c^2$ [94]; the relative permeability κ quantifies the permeability reduction resulting from trapping of the wetting fluid within the crevices of the medium, as visible in Figure 3.5(a). We independently measure $\kappa \approx 0.16$ using a homogeneous porous medium constructed and drained in a manner similar to the experiments reported here.

We hypothesize that the oil begins to invade the fine stratum when the flow rate is sufficiently large for the viscous pressure at the inlet, $P_v(0)$, to balance the capillary pressure required to invade a pore of the fine stratum $P_{\gamma,f}$. In non-dimensional form, this criterion is

$$Ca \approx Ca^* \equiv \frac{2a_c \cos \theta}{0.16a_f} \frac{a_c}{L} \frac{\kappa}{45} \frac{\phi^3}{(1-\phi)^2} \frac{A_c}{A} \quad (3.1)$$

We therefore expect drainage through only the coarse stratum for $Ca < Ca^*$; for Ca above this threshold, the oil can also begin to invade the adjacent fine stratum, in agreement with our observations [Figure 3.5(a-c)]. To test this prediction quantitatively, we repeat the experiments on many different stratified porous media, varying the bead sizes a_c and a_f , medium length L , and the cross-sectional areas A and A_c ; this enables us to vary Ca^* over one order of magnitude, $Ca^* \sim 10^{-5} - 10^{-4}$. For all of the media tested, we observe exclusive drainage through the coarse stratum below a threshold value of Ca , while above this threshold, the oil also begins to invade the adjacent fine stratum, as shown by the open and filled symbols in Figure 3.6, respectively. We find that the threshold for invasion into

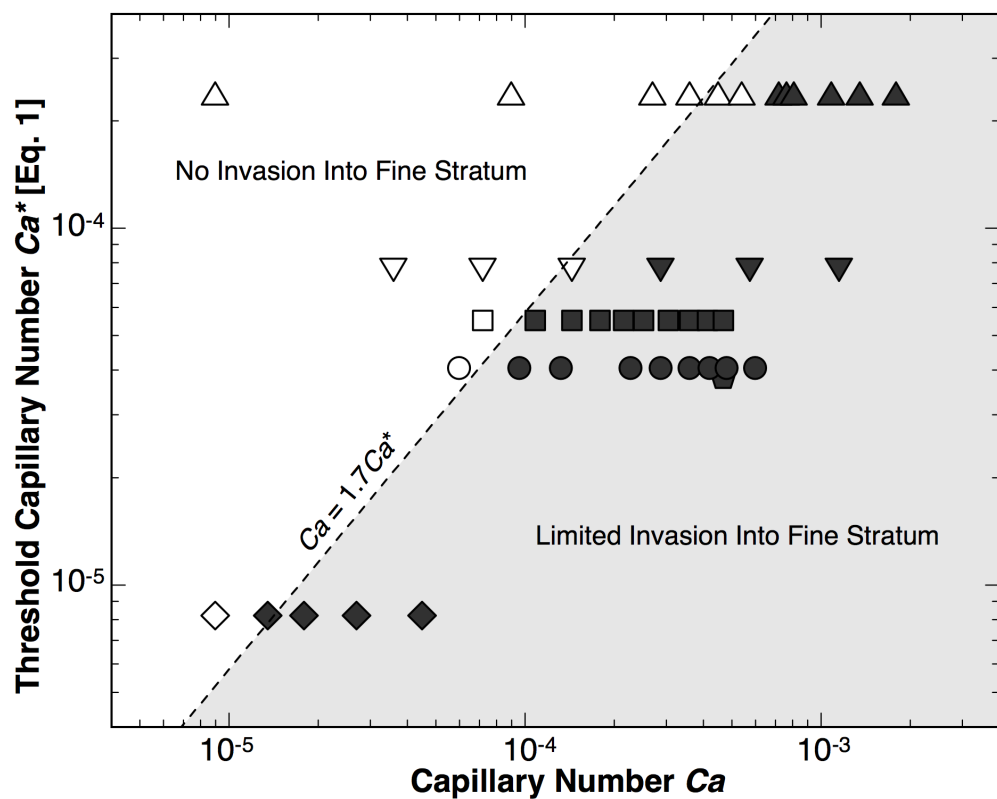


Figure 3.6: **For sufficiently small Ca , oil does not invade into fine stratum (open symbols), while for sufficiently large Ca , oil partially invades the fine stratum as well (filled symbols).** Data are shown for different porous media, with different cross-sectional areas, lengths, and bead sizes; these are thus characterized by different values of Ca^* , defined in Equation 3.1. The threshold for invasion into the fine stratum is approximately $Ca = 1.4Ca^*$ (dashed line).

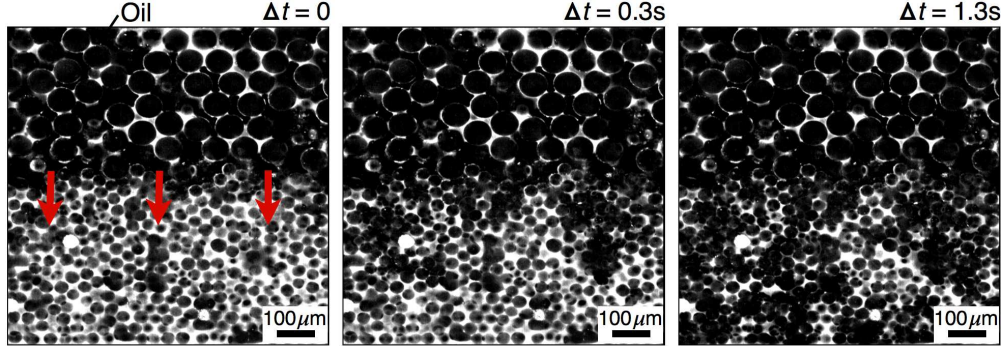


Figure 3.7: Time sequence of confocal micrographs, taken at $Ca > Ca^*$, showing flow of oil (black) from the coarse stratum laterally into the fine stratum, indicated by arrows in first panel. The flow is characterized by $Ca = 4.7 \times 10^{-4}$ and $Ca^* = 3.8 \times 10^{-5}$. Imposed flow direction is from left to right.

the fine stratum is given by $Ca \approx 1.4Ca^*$ over a broad range of Ca^* [Figure 3.6, dashed line], in close agreement with our prediction [Equation 3.1].

Within this picture, for sufficiently large Ca , oil is forced into the fine stratum not only from the inlet, but also laterally, from the adjacent coarse stratum [137, 138, 139]. By directly visualizing the drainage dynamics at $Ca > Ca^*$, we confirm this lateral flow, as indicated by the arrows in Figure 3.7. We therefore expect that the oil invades the fine stratum for all $x \leq L_f$, where P_v exceeds $P_{\gamma,f}$. Balancing these pressures yields

$$L_f/L = 1 - Ca^*/Ca \quad (3.2)$$

We test this prediction by measuring the variation of L_f with Ca for the different stratified porous media, characterized by $Ca^* \sim 10^{-5} - 10^{-4}$. For all of the experiments, we find that L_f/L increases with increasing Ca [inset to Figure 3.8], consistent with our expectation. Moreover, the data for different porous media collapse when Ca is rescaled by Ca^* , as shown in Figure 3.8, in agreement with Equation 3.2. The findings presented in Figure 3.6 suggest that Ca^* should be replaced by $1.4Ca^*$ in Equation 3.2; this yields an excellent fit

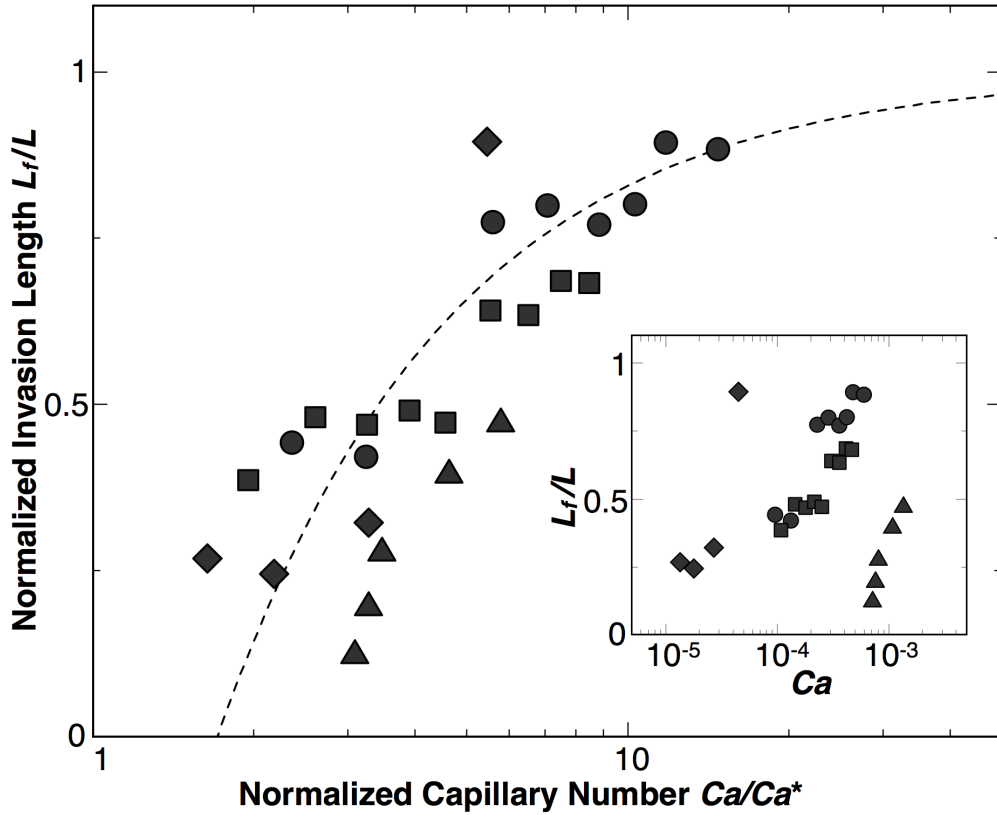


Figure 3.8: Geometry of invasion. (Inset) Distance invaded into the fine stratum, L_f , increases with increasing Ca ; different symbols represent different media characterized by different values of Ca^* . Symbols are the same as in Figure 3. L is the length of the medium. (Main panel) Data collapse when Ca is rescaled by Ca^* , and agree well with the theoretical prediction $L_f/L = 1 - 1.4Ca^*/Ca$ (dashed line).

to the data, as shown by the dashed line in Figure 3.8. Our model thus captures both the onset and the spatial extent of oil invasion into the fine stratum.

To test the generality of our results, we also study media with three different strata: a coarse stratum, comprised of beads with radius $a_c = 75\mu\text{m}$, a fine stratum, comprised of beads with radius $a_f = 19\mu\text{m}$, and an intermediate stratum separating the two, comprised of beads with radius $a_m = 38\mu\text{m}$. We observe flow behavior similar to the case of two strata: for $Ca = 1.8 \times 10^{-5}$ and 4.8×10^{-5} , the oil flows through the entire coarse stratum, and also

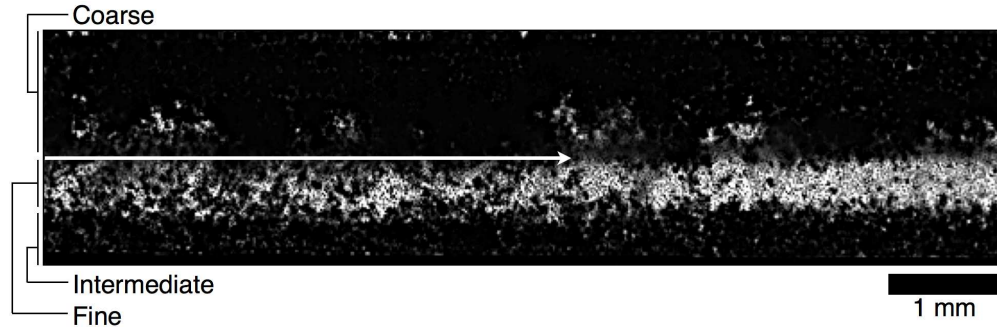


Figure 3.9: Optical section through part of a porous medium with three strata, obtained after the flow has reached an unchanging steady state. Both coarse and intermediate strata are completely invaded by the oil (black), while the fine stratum is only partially invaded, as indicated by the arrow. Imposed flow direction is from left to right; $Ca = 9.0 \times 10^{-5}$. The threshold $Ca^* = 2.4 \times 10^{-5}$ and 5.5×10^{-5} for the intermediate and fine strata, respectively.

partially invades the intermediate stratum; the spatial extent of this invasion increases with increasing Ca . Moreover, at an even higher $Ca = 9.6 \times 10^{-5}$, the oil also partially invades the fine stratum. The partial invasion into the intermediate stratum requires the lateral flow of oil from the coarse stratum; we thus expect that, if the positions of the intermediate and fine strata are switched, the intermediate stratum becomes *completely*, not partially, invaded above a threshold Ca . To test this idea, we study a medium with the fine stratum separating the coarse and the intermediate strata. At a $Ca = 4.5 \times 10^{-5}$, the oil completely invades both coarse and intermediate strata, in contrast with the previous case, and in direct agreement with our expectation [top and bottom strata in Figure 3.9]. Moreover, at an even higher $Ca = 9.0 \times 10^{-5}$, the oil partially invades the fine stratum [arrow in Figure 3.9], consistent with the picture presented here. These observations confirm that the flow path taken by the oil depends not only on the geometry of the individual strata, but also on their relative positions.

Using direct visualization by confocal microscopy, we demonstrate how stratification alters the path taken by a non-wetting fluid as it drains a 3D porous medium. For sufficiently small Ca , drainage proceeds only through the coarsest stratum of the medium; above a threshold Ca , the non-wetting fluid is also forced laterally, into part of the adjacent, finer strata. Our results highlight the essential role played by pore-scale capillary forces, which are frequently neglected from stratum-scale models of flow, in determining this behavior. Because geological formations are frequently stratified, we expect that our work will be relevant to a number of important applications, including understanding oil migration [140, 141], preventing groundwater contamination [142, 143], and sub-surface storage of CO₂ [144].

Chapter 4

Imbibition in a three-dimensional porous medium

The previous Chapter described drainage, the displacement of a wetting fluid from a porous medium by an immiscible non-wetting fluid. Another important class of multi-phase flow is imbibition, the displacement of a non-wetting fluid from a porous medium by an immiscible wetting fluid. When the 3D pore space is highly disordered, the fluid displacement during imbibition is complex; this can lead to the formation and trapping of discrete ganglia of the non-wetting fluid within the porous medium [10, 11, 12, 13, 14, 15, 16, 17, 18]. Some of this trapped non-wetting fluid can become mobilized as the capillary number characterizing the continued flow of the wetting fluid, $Ca \equiv \mu_w(Q_w/A)/\gamma$, is increased [145, 146, 19, 147, 148, 149]; μ_w is the viscosity of the wetting fluid, A is the cross-sectional area of the medium, and γ is the interfacial tension between the two fluids. The pore-scale physics underlying this phenomenon remains intensely debated. Visual inspection of the exterior of a porous medium, as well as some simulations, suggest that

as Ca increases, the ganglia are not immediately mobilized; instead, they break up into smaller ganglia only one pore in size [150, 151]. These then remain trapped within the medium, becoming mobilized only for large Ca . By contrast, other simulations, as well as experiments on individual ganglia, suggest that the ganglia do not break up; instead, all ganglia larger than a threshold size, which decreases with increasing Ca , become mobilized [86, 152, 153, 154]. The differences between these conflicting pictures, such as the geometrical configurations of the trapped ganglia, can have significant practical consequences: for example, smaller ganglia present a higher surface area per unit volume, potentially leading to their enhanced dissolution in the wetting fluid [155, 156]. This behavior impacts diverse situations ranging from the spreading of contaminants in groundwater aquifers to the storage of CO₂ in brine-filled formations. Elucidating the physics underlying ganglion trapping and mobilization is thus critically important; however, despite its enormous industrial relevance, a clear understanding of this phenomenon remains lacking. Unfortunately, systematic experimental investigations of it are challenging, requiring direct measurements of the pore-scale ganglia configurations within a 3D porous medium, as well as of the bulk transport through it, over a broad range of flow conditions.

In this Chapter³, we use confocal microscopy to directly visualize the formation and intricate morphologies of the trapped non-wetting fluid ganglia within a model 3D porous medium. The ganglia vary widely in their sizes and shapes. Intriguingly, these configurations do not vary for sufficiently small Ca ; by contrast, as Ca increases above a threshold value $\approx 2 \times 10^{-4}$, the largest ganglia start to become mobilized from the medium. Both the

³Based on “Mobilization of a trapped non-wetting fluid from a three-dimensional porous medium”, S. S. Datta, T. S. Ramakrishnan, and D. A. Weitz, to be submitted (2013) and “Visualizing multi-phase flow and trapped fluid configurations in a model three-dimensional porous medium”, A. T. Krummel*, S. S. Datta*, S. Munster, and D. A. Weitz, *AICHE Journal* 59, 1022 (2013) *Equal contribution.

size of the largest trapped ganglion, and the total amount of trapped non-wetting fluid, decrease with increasing Ca . We do not observe significant effects of ganglion breakup in our experiments. By combining our 3D visualization with measurements of the bulk transport properties of the medium, we show that the variation of the ganglia configurations with Ca can instead be understood using a mean-field model balancing the viscous forces exerted on the ganglia with the capillary forces that keep them trapped within the medium.

4.1 Pore-scale dynamics of secondary imbibition

To mimic discontinuous core-flood experiments on reservoir rocks, we first drain a wetting-fluid saturated 3D porous medium with 15 pore volumes of the non-wetting oil at a prescribed volumetric flow rate $Q_{nw} = 1 \text{ mL h}^{-1}$ through the porous medium. We then flow dyed wetting fluid at a fixed volumetric flow rate Q_w , as schematized in Figure 4.1; this process is known as secondary imbibition. To quantify the competition between the viscous and capillary forces at the pore scale, we calculate the corresponding capillary number, $Ca \equiv \mu_w(Q_w/A)/\gamma \sim 6.4 \times 10^{-7}$. This definition of Ca frequently occurs in the literature, and we therefore use it in this and the previous Chapter to facilitate comparison between our results and previous work. However, we note that a more accurate representation of the viscous force would also incorporate the medium porosity ϕ : the ratio of the viscous and capillary pressures then scales as $\mu_{nw}(Q_{nw}/\phi A)/\gamma$ instead. We use this more accurate definition of Ca in Chapter 6.

The presence of the thin layers of the wetting fluid profoundly changes the flow dynamics: unlike the case of drainage, discussed in the previous Chapter, the invading fluid does not simply burst into the pores. Instead, we observe that the wetting fluid first flows

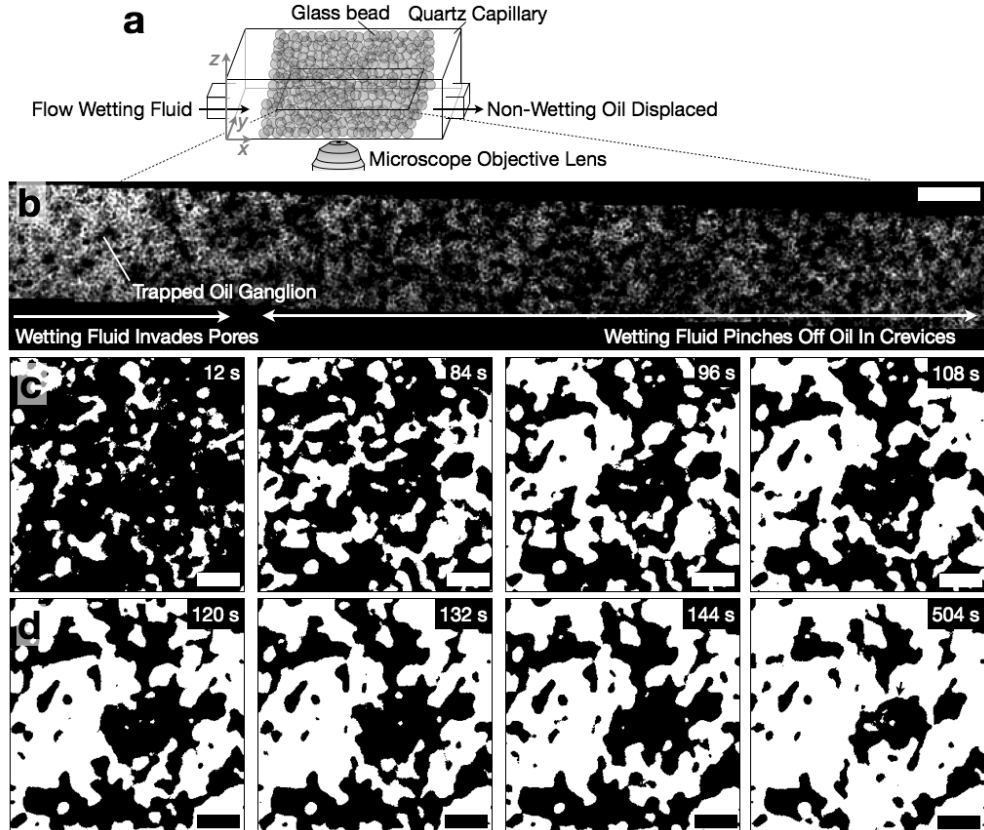


Figure 4.1: Visualizing secondary imbibition within a 3D porous medium. (a) Schematic of experimental setup. We directly visualize the flow within the medium using confocal microscopy. The fluorescently-dyed wetting fluid displaces the undyed non-wetting oil. (b) Optical section through part of the medium, taken as the wetting fluid displaces the oil at $Ca = 6.4 \times 10^{-7}$. Section is obtained at the same fixed z position, away from the lateral boundaries of the medium, as in Figure 3.1(b-c). Bright areas show the fluorescently-dyed wetting fluid, and the black circles show cross-sections of the beads making up the medium. Additional black areas show the oil. The wetting fluid first pinches off oil in crevices throughout the medium, as seen in the region spanned by the double-headed arrow, and then bursts into the pores of the medium, starting at the inlet, as seen in the region spanned by the single-headed arrow. Some oil ganglia remain trapped within the medium, as indicated. (c-d) Time sequence of zoomed confocal micrographs, with the oil-filled pore space subtracted; binary images thus show wetting fluid in white as it (c) initially pinches off oil in the crevices, and then (d) invades the pores. Time stamps indicate time elapsed after subtracted frame. Last frame shows unchanging steady state; arrow indicates a trapped oil ganglion. Scale bars in (b) and (c-d) are $500 \mu\text{m}$ and $200 \mu\text{m}$, respectively. Imposed flow direction in all images is from left to right.

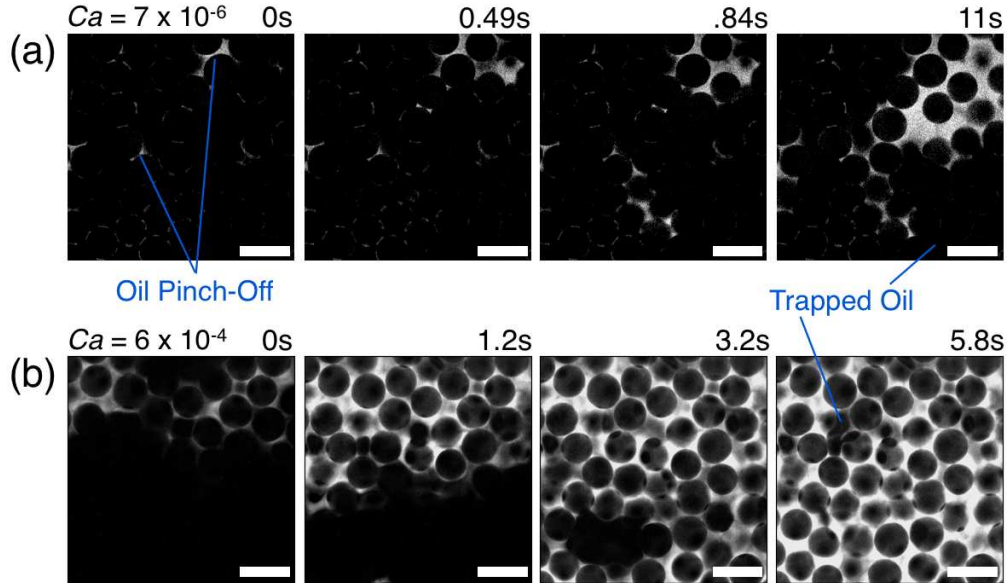


Figure 4.2: Pore-scale dynamics of secondary imbibition depend strongly on Ca . Images show multiple frames, taken at different times after drainage, of a single optical slice. The slice is $11\ \mu\text{m}$ thick and is imaged within a porous medium comprised of beads with average radius $a = 75\ \mu\text{m}$, with cross-sectional width 3 mm and height 1 mm. The bright areas show the dyed wetting fluid; the dark circles are the beads, while the additional dark areas are the undyed oil being displaced from the pore volume. Direction of bulk wetting fluid flow is from left to right. The final frame shows the unchanging steady state. Labels show time elapsed after first frame. (a) At low $Ca = 7 \times 10^{-6}$, the wetting fluid pinches off the oil at multiple nonadjacent constrictions, then displaces the oil from the surrounding pores. The wetting fluid eventually flows through a tortuous, continuous network of filled pores, forming many trapped oil ganglia. (b) At high $Ca = 6 \times 10^{-4}$, the occurrence of oil pinch-off is reduced, and the wetting fluid displaces the oil from the pores, leaving a few small oil ganglia trapped within the medium. Scale bars are $200\ \mu\text{m}$.

through the thin layers, pinching off the oil in multiple nonadjacent crevices throughout the entire medium [112, 157, 158] over a period of approximately 60 s, as seen in the region spanned by the double-headed arrow in Figure 4.1(b), in the time sequence shown in Figure 4.1(c), and in the time sequence shown in Figure 4.2(a). This behavior agrees with the predictions of recent numerical simulations [159]. The wetting fluid then also begins to invade the pores through a series of intermittent, abrupt bursts, starting from the inlet, as seen in the region spanned by the single-headed arrow in Figure 4.1(b) and in the time sequence shown in Figure 4.1(d). Interestingly, as the wetting fluid invades the medium, it bypasses many of the pores, leaving discrete oil ganglia of varying sizes in its wake. Many of these ganglia remain trapped within the pore space, as indicated in Figure 4.1(b).

To explore the dependence of oil displacement on flow conditions, we visualize secondary imbibition for varying Ca . Unlike the low Ca case, we do not observe oil pinch-off at higher $Ca \sim 10^{-4} - 10^{-3}$; instead, the wetting fluid displaces the oil from the pores, as shown in Figure 4.2(b). This indicates that flow through the thin wetting layers becomes less significant as Ca is increased. This observation confirms the predictions of recent simulations [129, 125]. However, some of the oil is still bypassed by the wetting fluid, forming disconnected oil ganglia [160]; in several cases, the ganglia break up into smaller ganglia. Many of these ganglia are mobilized from the medium; however, a few smaller ganglia remain trapped [last frame in Figure 4.2(b)]. For sufficiently long times, these ganglia cease to move, and the pressure drop across the medium does not appreciably change, indicating that a steady state is reached. These results thus highlight the important role played by the wetting layers in influencing the flow behavior.

4.2 Trapped oil ganglia configurations

We use our confocal micrographs to measure the total amount of oil trapped within the porous medium; this is quantified by the residual oil saturation, $S_{or} \equiv V_o/\phi V$, where V_o is the total volume of oil imaged within a region of volume V and ϕ is the porosity of the medium. After secondary imbibition at $Ca = 6.4 \times 10^{-7}$, we find $S_{or} \approx 9\%$. To mimic discontinuous core-flood experiments on reservoir rocks, we then explore the variation of S_{or} in response to progressive increases in the wetting fluid Ca . For each value of Ca , we flow at least 13 pore volumes of the wetting fluid, thus establishing a new steady state, before reacquiring an additional set of 3D stacks. By comparing each set of stacks with that obtained during the initial pore structure characterization, we obtain the 3D morphologies of the oil ganglia left trapped at each Ca . The Reynolds number characterizing the pore-scale flow is given by $Re \equiv \rho_w(Q_w/\phi A)a_t/\mu_w \approx 8 \times 10^{-6} - 8 \times 10^{-2}$, where ρ_w is the density of the wetting fluid, $a_t \approx 0.16a$ is the typical radius of a pore entrance, and a is the average bead radius; our experiments are therefore characterized by laminar flow. The Bond number characterizing the influence of gravity relative to capillary forces at the pore scale is given by $Bo \equiv g(\rho_w - \rho_{nw})a_t^2/\gamma \approx 10^{-6}$, where ρ_{nw} is the density of the non-wetting fluid, indicating that gravity only becomes appreciable on the vertical length scale of the entire medium. We therefore neglect gravity from our subsequent theoretical analysis.

We find that S_{or} does not vary significantly for sufficiently small Ca ; however, as Ca is increased above 2×10^{-4} , S_{or} decreases precipitously, as shown in Figure 4.3, ultimately reaching only $\approx 7\%$ of its initial value. These results are consistent with the results of previous core-flood experiments, which show similar behavior for fluids of a broad range of viscosities and interfacial tensions [149].

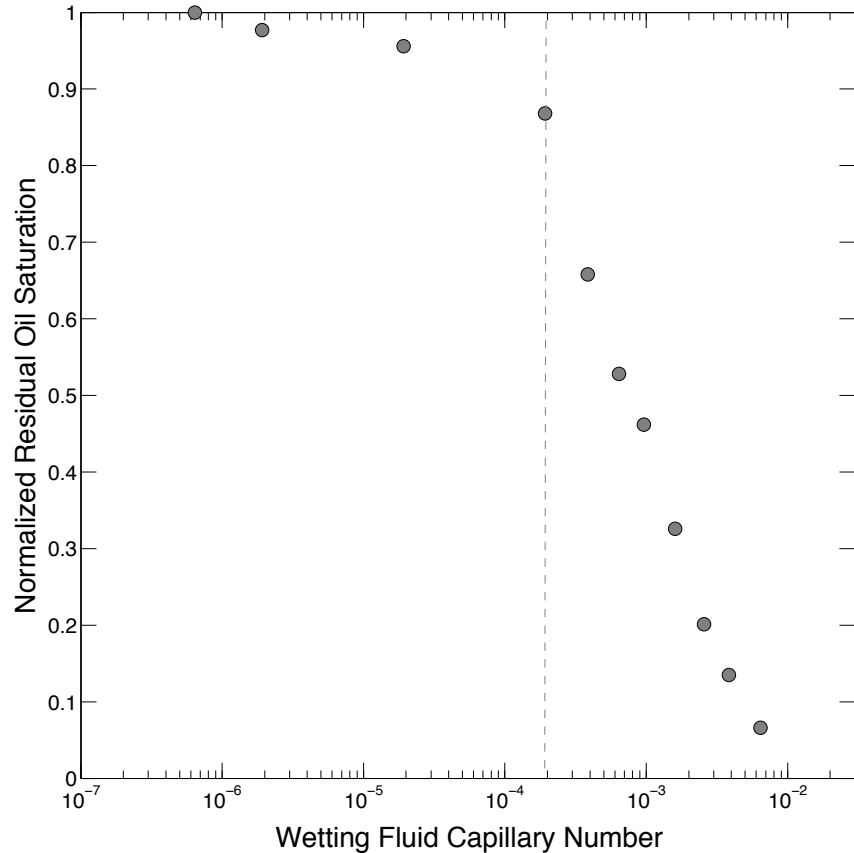


Figure 4.3: Variation of residual oil saturation S_{or} with wetting fluid capillary number Ca . We normalize S_{or} by its maximum value; we find that S_{or} does not vary significantly for small Ca , but decreases precipitously as Ca increases above 2×10^{-4} (dashed grey line). Residual oil saturation is measured using 3D confocal micrographs.

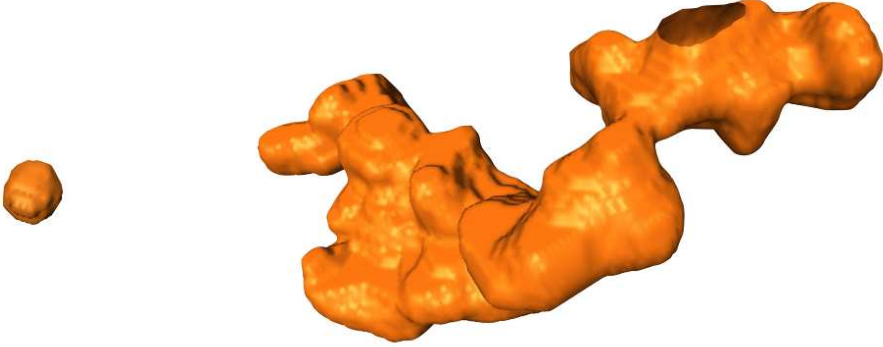


Figure 4.4: **3D renderings of oil ganglia trapped after secondary imbibition at $Ca = 6.4 \times 10^{-7}$.** The left ganglion is spherical and only spans ≈ 0.3 beads in diameter, whereas the right ganglion is more ramified and spans multiple beads. Renderings are produced using 3D confocal micrographs.

To better understand this behavior, we inspect the reconstructed 3D morphologies of the individual ganglia for each Ca investigated. At the smallest $Ca \approx 6 \times 10^{-7} - 2 \times 10^{-4}$, the ganglia morphologies vary widely, as exemplified by the 3D renderings shown in Figure 4.4. The smallest ganglia are spherical, only occupying single pores, and span ≈ 0.3 beads in size [left, Figure 4.4]; in stark contrast, the largest ganglia are ramified, occupying multiple pores, and span many beads in size [right, Figure 4.4]. To quantify the significant variation in their morphologies, we measure the length L of each ganglion along the flow direction, and plot 1-CDF(L), where $CDF = \sum_0^L Lp(L) / \sum_0^\infty Lp(L)$ is the cumulative distribution function of ganglia lengths and $p(L)$ is the number fraction of ganglia having a length L . Consistent with the variability apparent in the 3D renderings, we find that the ganglia lengths are broadly distributed, as indicated by the circles in Figure 4.5.

Percolation theory predicts that the number fraction of ganglia with volume s is, for large s , given by $p(s) \propto s^{-\tau}$, where $\tau \approx 2.2$ is a scaling exponent [161, 162, 163]. More-

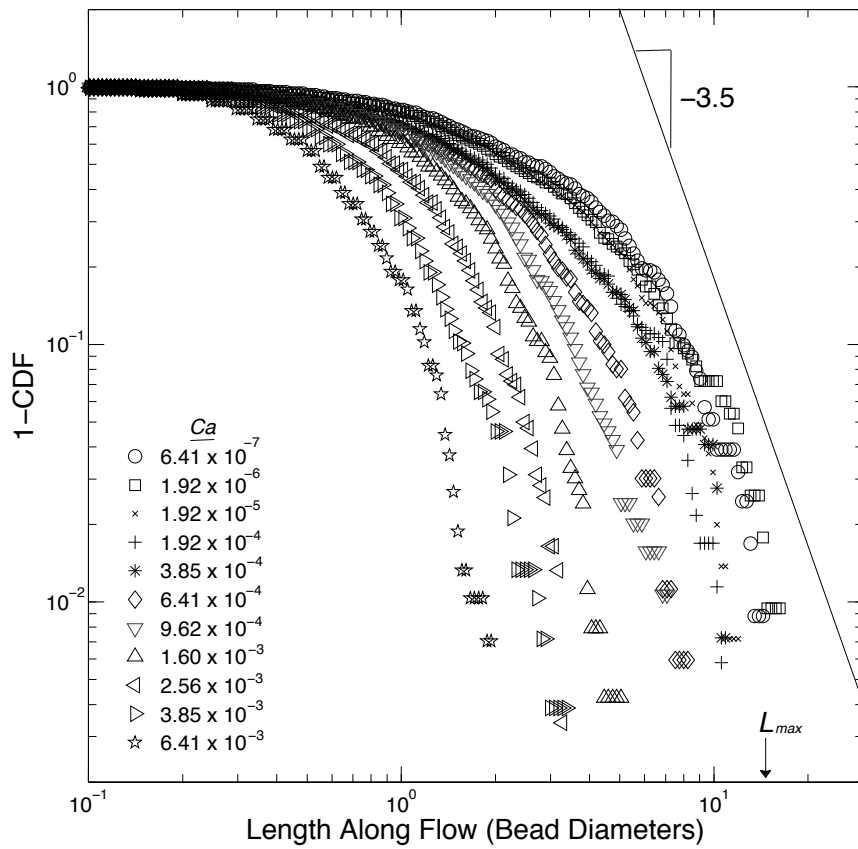


Figure 4.5: Quantifying variability in ganglion sizes. Complementary cumulative distribution functions 1-CDF of ganglia lengths L , measured along the flow direction using 3D confocal micrographs, after secondary imbibition at a range of wetting fluid capillary numbers Ca . Solid line shows $\sim L^{-3.5}$ scaling. Arrow indicates maximum ganglion length L_{max} at the lowest $Ca = 6.41 \times 10^{-7}$.

over, the volume of a ganglion varies with its length as $s \propto L^{3/(\tau-1)}$. Combining these two relations yields $p(L) \propto L^{-3\tau/(\tau-1)}$, and therefore, $Lp(L) \propto L^{-3\tau/(\tau-1)+1}$. In our experiments, we measure the complementary cumulative distribution function of ganglia lengths, $1-CDF(L) = \sum_L^\infty Lp(L) / \sum_0^\infty Lp(L)$. The percolation theory prediction is thus $1-CDF(L) \propto L^{-3\tau/(\tau-1)+2} \propto L^{-3.5}$, using $\tau \approx 2.2$; this prediction is in good agreement with the large L tail of our data, as shown by the solid line in Figure 4.5. This result also agrees with recent X-ray microtomography experiments [26, 164]. We also find that the largest trapped ganglion has a length $L_{max} \approx 13$ bead diameters [arrow in Figure 4.5]; while we cannot exclude the influence of boundary effects or the limited imaging volume, this value is in good agreement with the prediction of percolation theory, incorporating a non-zero viscous pressure: $L_{max} \approx \alpha(a^2 Ca/\kappa k)^{-\nu/(1+\nu)} \approx 9\alpha$ bead diameters, where $\nu \approx 0.88$ is a scaling exponent, α is a constant of order unity, and we use the value of κ measured at the lowest Ca [165]. Taken together, these results suggest that the configurations of the ganglia left trapped after secondary imbibition can be understood using percolation theory.

As Ca increases, we do *not* observe significant effects of ganglia breakup; this observation is contrary to some previous suggestions [151], and confirms the predictions of other numerical simulations [153]. Instead, the ganglia configurations remain the same for all $Ca < 2 \times 10^{-4}$ [\circ , \square , and \times in Figure 4.5]. Moreover, we find that the largest ganglia start to become mobilized from the porous medium, concomitant with the observed decrease in S_{or} , once Ca increases above 2×10^{-4} [Figure 4.5]. We quantify this behavior by plotting the variation of L_{max} with Ca . While L_{max} remains constant at small Ca , it decreases precipitously as Ca increases above 2×10^{-4} , as shown by the circles in Figure 4.6. Remarkably, this behavior closely mimics the observed variation of S_{or} with Ca [Figure 4.3].

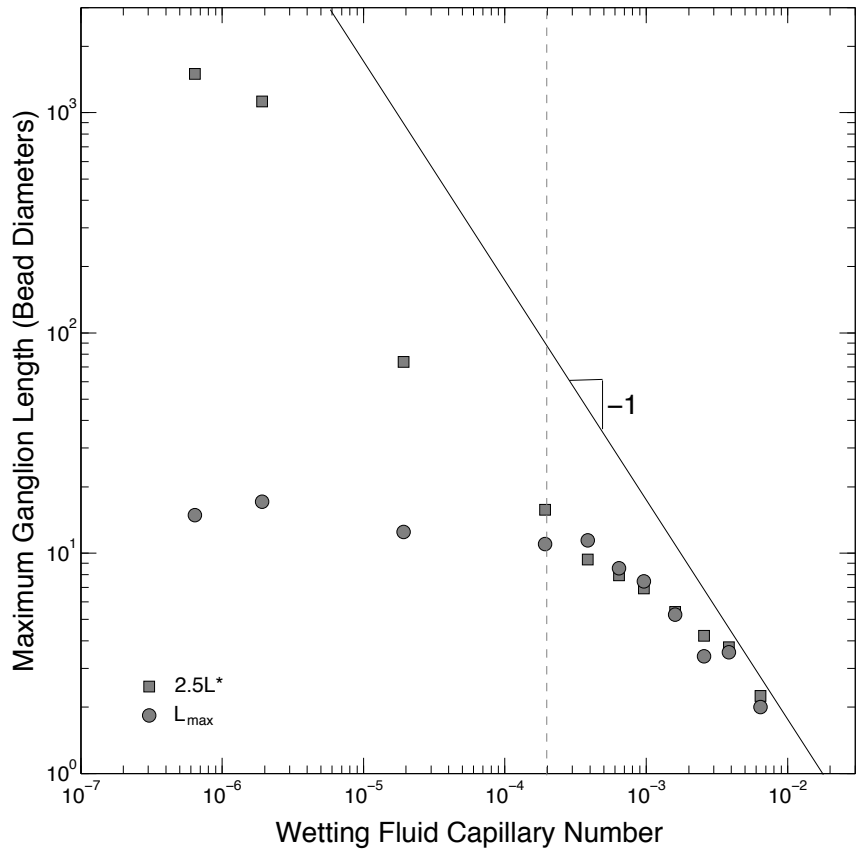


Figure 4.6: **Quantifying variation in ganglion sizes with Ca .** Variation of maximum trapped oil ganglion length L_{max} , measured along the flow direction using 3D confocal micrographs, and 2.5 times the theoretical L^* , calculated using Equation 4.3, with the wetting fluid capillary number Ca . Similar to the variation of the residual oil saturation S_{or} , shown in Figure 3, L_{max} does not vary significantly for small wetting fluid capillary number Ca , but decreases precipitously as Ca increases above 2×10^{-4} (dashed grey line). Both L_{max} and L^* do not scale as $\sim Ca^{-1}$, indicated by the solid line.

These results thus suggest that the variation of S_{or} with increasing Ca is not determined by the breakup of the trapped ganglia; instead, it may reflect the mobilization of the largest ganglia from the medium.

4.3 Physics of ganglion mobilization

To understand the ganglia mobilization, we analyze the distribution of pressures in the wetting fluid as it flows through the porous medium. Motivated by previous studies of this flow [166, 86, 19], we make the mean-field assumption that the viscous pressure drop across a ganglion of length L is given by Darcy's law,

$$P_v = \frac{\mu_w Q_w}{\kappa k} L \quad (4.1)$$

The relative permeability $\kappa \leq 1$ quantifies the modified transport through the medium due to the presence of the trapped oil. To determine P_v at each Ca investigated, we use pressure transducers to directly measure the variation of κ with Ca for a porous medium constructed in a manner similar to, and following the same flow procedure as, that used for visualization of the ganglia configurations. Interestingly, κ does not vary significantly for sufficiently small Ca ; however, as Ca increases above 2×10^{-4} , κ quickly increases, concomitant with the observed decreased in S_{or} , as shown in Figure 4.7. This observation suggests that the bulk transport behavior of the medium depends strongly on the trapping of oil within it. To quantify the close link between the variation of κ and S_{or} with Ca [149], we plot κ as a function of the wetting fluid saturation, $1 - S_{or}$. Consistent with our expectation [167], we find that κ increases monotonically with increasing wetting fluid saturation, as shown in Figure 4.8.

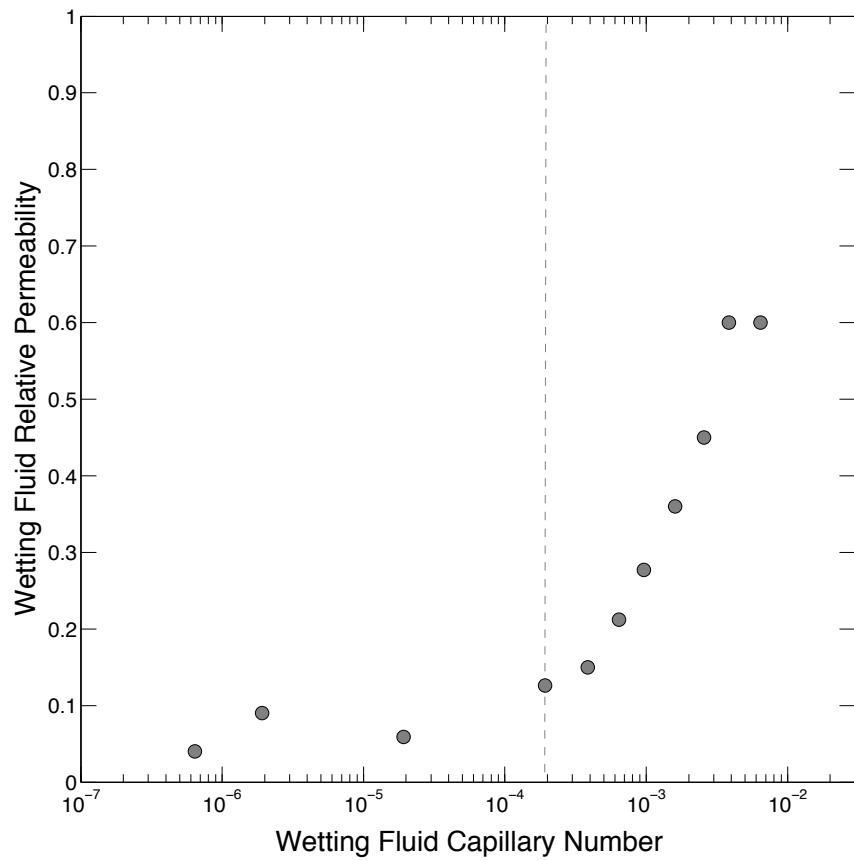


Figure 4.7: Variation of wetting fluid relative permeability κ , measured using pressure transducers, with the wetting fluid capillary number Ca . Similar to the variation of the residual oil saturation S_{or} , shown in Figure 3, κ does not vary significantly for small wetting fluid capillary number Ca ; however, it increases dramatically as Ca increases above 2×10^{-4} (dashed grey line).

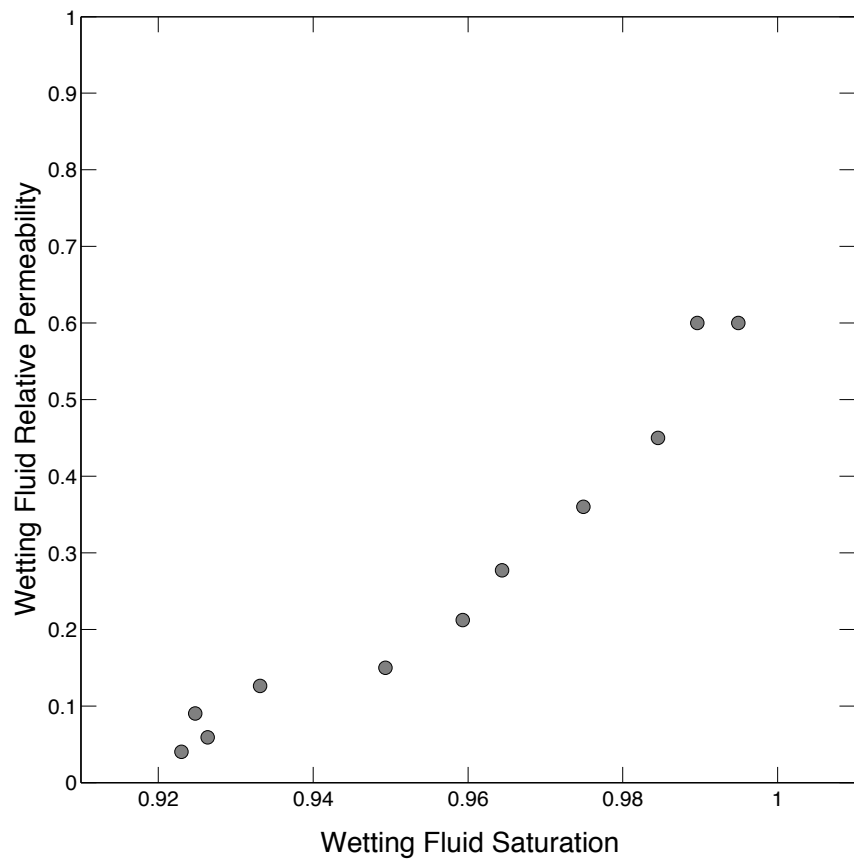


Figure 4.8: Variation of wetting fluid relative permeability κ , measured using pressure transducers, with the saturation of wetting fluid in the pore space, $1 - S_{or}$. We find that κ increases monotonically as the amount of trapped oil is decreased.

For a ganglion to squeeze through the pores of the medium, it must simultaneously displace the wetting fluid from a downstream pore, and be displaced by the wetting fluid from an upstream pore. To displace the wetting fluid from a downstream pore, a threshold capillary pressure must build up at the pore entrance, as schematized by the right set of arrows in Figure 4.9; this threshold is given by $P_t = 2\gamma \cos \theta / a_t$, where a_t is the radius of the pore entrance [15, 97, 96], with an average value $\approx 0.16a$ for a 3D packing of glass beads [113, 114]. Similarly, for the trapped oil to be displaced from an upstream pore, the capillary pressure within the pore must fall below a threshold, as schematized by the left set of arrows in Figure 4.9; this threshold is given by $P_b = 2\gamma \cos \theta / a_b$, where a_b is instead the radius of the pore itself, with an average value $\approx 0.24a$ [114, 113]. Thus, to mobilize a ganglion from the porous medium, the total viscous pressure drop across it must exceed a capillary pressure threshold,

$$P_t - P_b = \frac{2\gamma \cos \theta}{a_b} \left(\frac{a_b}{a_t} - 1 \right) \quad (4.2)$$

Balancing Equations 4.1 and 4.2, we therefore expect that, at a given Ca , the smallest ganglia remain trapped within the medium; however, the viscous pressure in the wetting fluid is sufficiently large to mobilize all ganglia larger than

$$L_{max} = L^* \equiv \frac{2 \cos \theta}{Ca} \left(\frac{a_b}{a_t} - 1 \right) \frac{\kappa k}{a_b} \quad (4.3)$$

To critically test this prediction, we compare the variation of both L_{max} , directly measured using confocal microscopy, and L^* , calculated using the measured values of θ , k , and κ , with Ca . For small Ca , we find $L_{max} < L^*$, as shown by the first three points in Figure 4.6; this indicates that the viscous pressure in the wetting fluid is too small to mobilize any ganglia. Consequently, S_{or} does not vary significantly for this range of Ca , consistent with

the measurements shown in Figure 4.3. As Ca increases, L_{max} remains constant; however, L^* steadily decreases, eventually becoming comparable to L_{max} at $Ca \approx 2 \times 10^{-4}$, shown by the dashed line in Figure 4.6. Strikingly, as Ca increases above this value, we find that both L_{max} and L^* decrease in a similar manner, with $L_{max} \approx 2.5L^*$; this indicates that the viscous pressure in the wetting fluid is sufficient to mobilize more and more of the largest ganglia. Consequently, we expect S_{or} to also decrease with Ca in this range, in excellent agreement with our measurements [Figure 4.3]. The similarity in the variation of L_{max} and S_{or} with Ca , and the close agreement between our measured L_{max} and the predicted L^* for $Ca > 2 \times 10^{-4}$, thus confirm that the reduction in S_{or} reflects the mobilization of the largest ganglia.

Using confocal microscopy, we directly visualize the dynamics of secondary imbibition, as well as the intricate morphologies of the resultant trapped non-wetting fluid ganglia, within a 3D porous medium, at pore-scale resolution. The wetting fluid first flows through thin layers coating the solid surfaces, pinching off the non-wetting fluid in crevices throughout the medium. It then displaces the non-wetting fluid from the pores of the medium through a series of intermittent, abrupt bursts, starting from the inlet, leaving ganglia of the non-wetting fluid in its wake. These vary widely in their sizes and shapes, consistent with the predictions of percolation theory. We do not observe significant effects of ganglion breakup, contrary to some previous suggestions. Instead, for small Ca , the ganglia configurations do not appreciably change, while as Ca is increased above a threshold value, more and more of the largest ganglia become mobilized from the medium. We emphasize that, due to the concomitant variation of the wetting fluid permeability with Ca , the measured L_{max} does *not* decrease as Ca^{-1} [solid line in Figure 4.6]; this is in contra-

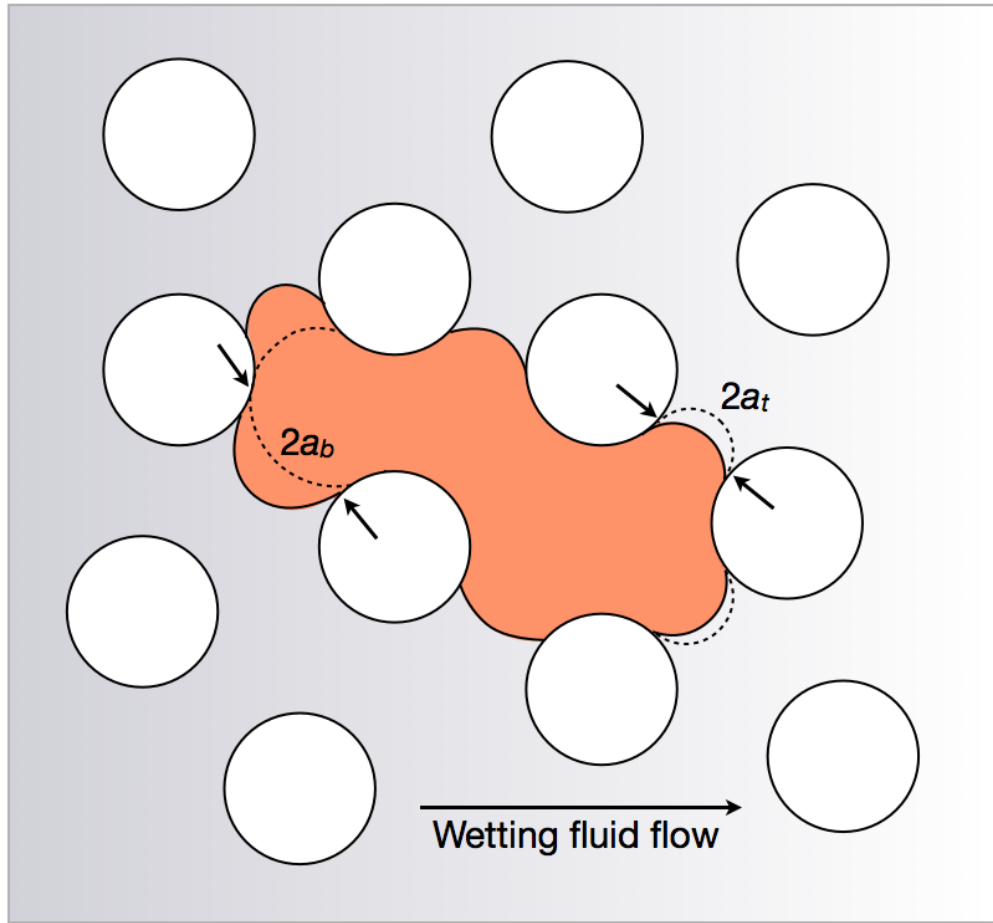


Figure 4.9: **Physics of ganglion mobilization.** 2D schematic showing an oil ganglion (orange) trapped within the pore space, with wetting fluid flowing from left to right; beads are shown by white circles. Dashed lines show threshold curvatures required for the ganglion to invade the downstream pores or be displaced from the upstream pores.

diction to results obtained for an isolated ganglion [86], for which the permeability is a constant, which are often assumed to also apply to a population of many ganglia. By coupling the 3D visualization and bulk transport measurement, we show that the variation of the ganglia configurations can be understood by balancing the viscous forces exerted on the ganglia with the pore-scale capillary forces that keep them trapped within the medium. This work thus helps elucidate the fluid dynamics underlying the mobilization of a trapped non-wetting fluid from a 3D porous medium.

Our results provide direct visualization of the multi-phase flow and the ganglia configurations within a 3D porous medium; moreover, they highlight the applicability of a mean-field picture in understanding the mobilization of the trapped non-wetting fluid. This work may thus help guide theoretical models or numerical simulations (e.g. [168, 169]). Moreover, because many geophysical flows give rise to residual trapping, we expect that our work will be relevant to a number of important applications, including enhancing oil recovery, understanding the distribution of contaminants in groundwater aquifers, or the storage of CO₂ in sub-surface formations.

Chapter 5

Spatial fluctuations of fluid velocities in flow through a three-dimensional porous medium

The flow of a single fluid through a 3D porous medium, when sufficiently slow, is typically modeled using Darcy's law, which relates the pressure drop across the entire medium to the flow velocity, averaged over a sufficiently large length scale. However, while appealing, this simple continuum approach neglects local pore-scale variations in the flow, which may arise as the fluid navigates the tortuous 3D pore space of the medium. Experimental measurements using optical techniques [170, 171, 172, 173, 174, 175, 176, 177, 178, 179, 180, 181] and nuclear magnetic resonance imaging [182, 183, 28, 29, 184, 185] confirm that the fluid speeds are broadly distributed. However, these measurements often provide access to only one component of the velocity field, and only for the case of single-phase flow; moreover, they typically yield limited statistics, due to the difficulty of probing the

flow in 3D, both at pore scale resolution and over large length scales. While theoretical models and numerical simulations provide crucial additional insight [28, 29, 30, 31, 32, 33, 34, 35, 36, 37, 1, 38, 39, 40], fully describing the disordered structure of the medium can be challenging. Consequently, despite its enormous practical importance, a complete understanding of flow within a 3D porous medium remains elusive.

In this Chapter⁴, we use confocal microscopy to directly visualize the highly variable flow within a 3D porous medium over a broad range of length scales, from the scale of individual pores to the scale of the entire medium. We find that the velocity magnitudes and the velocity components both along and transverse to the imposed flow direction are exponentially distributed, even when a second immiscible fluid is trapped within the medium. Moreover, we find underlying pore-scale correlations in the flow, and show that these correlations are determined by the geometry of the medium. The pore space is highly disordered and complex; nevertheless, our results indicate that fluid flow through it is not completely random.

5.1 Visualizing single-phase flow

We prepare a rigid 3D porous medium composed of beads with radii $32 \pm 2 \mu\text{m}$, in a thin-walled square quartz capillary of cross-sectional area $A = 9 \text{ mm}^2$. The packing has length $L \approx 8 \text{ mm}$ and porosity $\phi \approx 0.41$. To visualize the single-phase flow, we formulate the viscous wetting fluid described in Chapter 2, suspending 0.01 vol% of $1 \mu\text{m}$ diameter fluorescent latex microparticles within it. Prior to each experiment, the porous medium is

⁴Based on “Spatial fluctuations of fluid velocities in flow through a three-dimensional porous medium”, **S. S. Datta**, T. S. Ramakrishnan, and D. A. Weitz, *Physical Review Letters* 111, 064501 (2013).

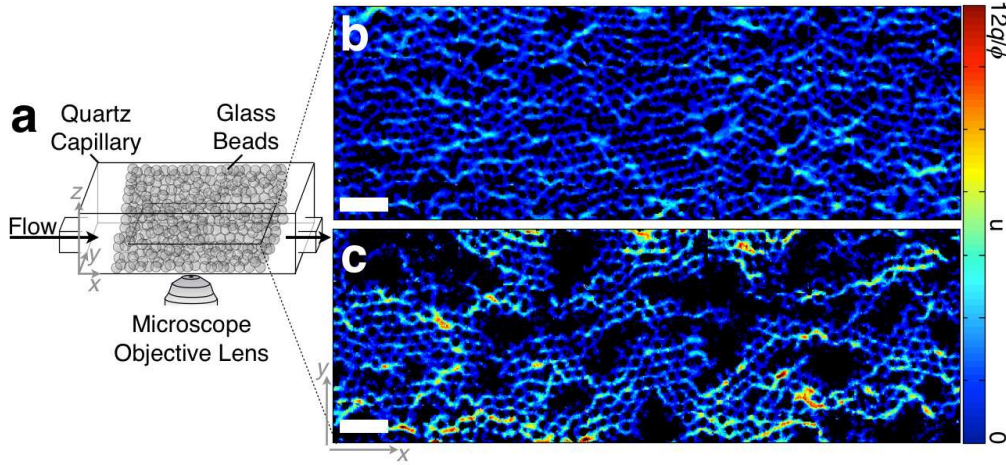


Figure 5.1: Visualizing flow speeds within a 3D porous medium. (a) Schematic showing porous medium and imaging geometry. A portion of the 2D map of velocity magnitudes within the medium is shown for (b) single-phase flow, and (c) flow with trapped residual oil. Black circles in (b) show beads making up the medium, while additional black regions in (c) show residual oil. Scale bars are 500 μm long, while color scale shows speeds ranging from 0 (blue) to $12q/\phi$ (red).

evacuated under vacuum and saturated with CO₂ gas, which is soluble in the tracer-laden fluid; this procedure eliminates the formation of trapped bubbles. We then saturate the pore space with the tracer-laden fluid, imposing a constant volumetric flow rate $Q = 0.2 \text{ mL/hr}$; the average interstitial velocity is thus given by $q/\phi \equiv (Q/A)/\phi = 15 \text{ } \mu\text{m/s}$.

To directly visualize the steady-state pore-scale flow, we use a confocal microscope to acquire a movie of 100 optical slices in the xy plane, collecting 15 slices/s, at a fixed z position several bead diameters deep within the porous medium. Each slice is 11 μm thick along the z axis and spans a lateral area of 912 $\mu\text{m} \times 912 \mu\text{m}$ in the xy plane [Figure 5.1(a)]. To visualize the flow at the scale of the entire medium, we acquire additional movies, at the same z position, but at multiple locations in the xy plane spanning the entire width and length of the medium. We restrict our analysis to an area several beads away from each edge of the medium to minimize boundary effects. To reduce image noise, we threshold

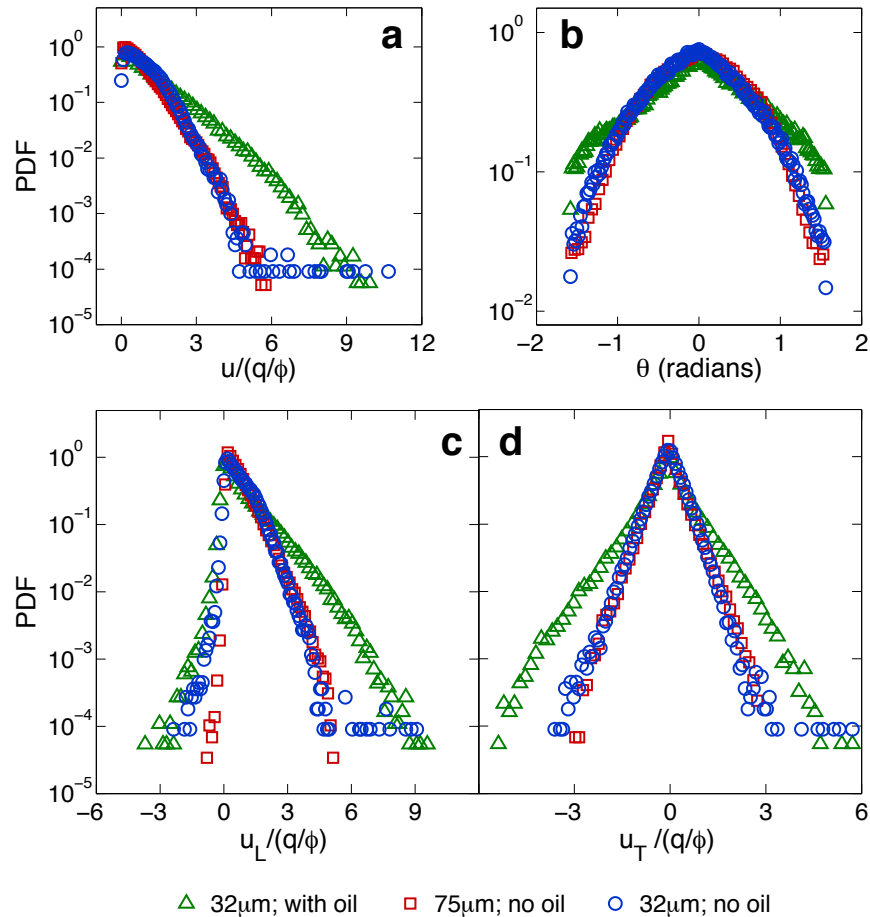


Figure 5.2: Quantifying the variability in the flow. Probability density functions of 2D (a) normalized velocity magnitudes, $u/(q/\phi)$, (b) velocity orientation angles, θ , (c) normalized velocity component along the imposed flow direction, $u_L/(q/\phi)$, and (d) normalized velocity component transverse to the imposed flow direction, $u_T/(q/\phi)$. Blue circles and red squares show statistics of single-phase flow through media comprised of $32 \mu\text{m}$ and $75 \mu\text{m}$ radius beads, respectively, while green triangles show statistics of flow through the medium comprised of $32 \mu\text{m}$ radius beads, with trapped residual oil.

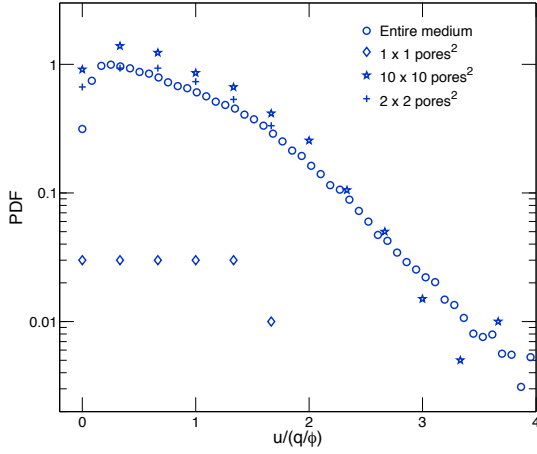


Figure 5.3: Dependence of statistics on window size. Probability density functions of normalized 2D velocity magnitudes, $u/(q/\phi)$, for single-phase flow without residual oil trapping through a medium comprised of beads with average radius $32 \mu\text{m}$, for square windows approximately one (diamonds), two (crosses), and ten (stars) pores across; circles show data for the entire porous medium. Data are vertically offset for clarity.

and apply a median filter to each optical slice. We have verified that the results presented do not significantly change depending on how the images are filtered. We have also verified that the results do not change with depth (z position), for the imaging parameters used.

The ratio of viscous forces to gravitational forces on the tracer particles is given by $9\mu_w(q/\phi)/2(\rho_w - \rho_p)ga_p^2 \approx 10^4 - 10^5$, where g is gravitational acceleration, and $\rho_w \approx 1.23 \text{ g cm}^{-3}$ and $\rho_p \approx 1.01 \text{ g cm}^{-3}$ are the densities of the fluid and the particles, respectively; moreover, the time required for a particle to settle a vertical distance of $11 \mu\text{m}$, equal to the thickness of the optical slice, is $< 10^4 \times 11 \mu\text{m}/(q/\phi) \sim 10 \text{ min}$, approximately 100 times larger than the time required to acquire one movie. The time for a tracer particle to diffuse its own size is approximately $\pi\mu_w a_p^3/k_B T \approx 6 \text{ s}$, where k_B is Boltzmann's constant and $T \approx 300 \text{ K}$ is temperature; this is almost 100 times larger than the time between two successive frames of the movies. We thus conclude that the tracer particles are faithfully advected

with the flow. We note that measurements in two dimensional micromodels suggest that the tracer particles may not fully sample the smallest fluid velocities near the bead surfaces. However, we do not expect this to significantly affect the measured distribution of the larger fluid velocities, which are the primary focus of our work. Moreover, we do not observe significant differences between the data for porous media comprised of 32 μm and 75 μm beads. The tracer Peclet number, quantifying the importance of advection relative to diffusion in determining the particle motion, is $(q/\phi)/(k_B T/6\pi a_p) > 10^3$; thus, our experiments only probe the advection motion of the fluid, in contrast to other measurements that measure the combined effects of advection and diffusion.

We use the PIVLab package for MATLAB to characterize the flow field using particle image velocimetry, dividing each optical slice into 16129 interrogation windows, and calculating the displacement of tracer particles in each window by cross-correlating successive slices of each movie. By combining the displacement field thus obtained for all the positions imaged, and dividing the displacements by the fixed time difference between slices, we generate a map of the 2D fluid velocities, \mathbf{u} , over the entire extent of the porous medium. This protocol thus enables us to directly visualize the flow field, both at the scale of the individual pores and at the scale of the overall medium. For calibration, we use this protocol to visualize and confirm the parabolic Poiseuille flow profile within a square capillary of cross-sectional width 550 μm . Moreover, we confirm that PIV performed using interrogation windows 0.75 and 0.5 times the size of those used here yield similar results.

The flow within the porous medium is highly variable, as illustrated by the map of velocity magnitudes shown in Figure 5.1(b). To quantify this behavior, we calculate the probability density functions (pdfs) of the 2D velocity magnitudes, $u = |\mathbf{u}|$, velocity orientation

angles relative to the imposed flow direction, θ , and the velocity components both along and transverse to the imposed flow direction, $u_L = u \cos \theta$ and $u_T = u \sin \theta$, respectively. Consistent with the variability apparent in Figure 5.1(b), we find that both the velocity magnitudes and orientations are broadly distributed, as shown by the blue circles in Figure 5.2(a-b). Interestingly, the pdf of u decays nearly exponentially, with a characteristic speed $\approx 0.5q/\phi$, consistent with the results of recent numerical simulations [186].

The pore space is highly disordered and complex; as a result, we expect flow through it to be random, and thus, the motion of the fluid transverse to the imposed flow direction to be Gaussian distributed [40, 187]. As expected, the measured pdf of u_T is symmetric about $u_T = 0$; however, we find that it is strikingly non-Gaussian, again exhibiting an exponential decay over nearly four decades in probability, with a characteristic speed $\approx 0.25q/\phi$ [blue circles in Figure 5.2(d)]. The pdf of u_L similarly decays exponentially, consistent with results from previous NMR measurements [183]; moreover, the characteristic speed along the imposed flow direction is $\approx 0.5q/\phi$, double the characteristic speed in the transverse direction [blue circles in Figure 5.2(c)]. These results indicate that flow within a 3D porous medium may, remarkably, not be completely random.

5.2 Quantifying correlations in the flow

To elucidate this behavior, we characterize the spatial structure of the flow by examining the length scale dependence of the statistics shown in Figure 5.2. We do this by calculating the velocity pdfs for observation windows, centered on the same pore, of different sizes. Similar to the pdfs for the entire medium, the pdfs for windows one pore in size are broad; however, they have a different shape, as exemplified by the diamonds in Figure 5.3. By

contrast, the pdfs for larger observation windows, even those just a few pores in size, are similar to those for the entire medium; two examples are shown by the crosses and stars in Figure 5.3, corresponding to windows two and ten pores across, respectively. This suggests that the variability of flow within the entire porous medium reflects a combination of the flow variability within the individual pores and the geometry of the pore space.

Another clue to the physical origin of this non-random behavior comes from close inspection of the flow field in Figure 5.1(b): we observe tortuous “fingers”, approximately one pore wide and extending several pores along the imposed flow direction, over which the velocity magnitudes appear to be correlated. To quantify these correlations, we subtract the mean velocity from each 2D velocity vector to focus on the velocity fluctuations, $\delta\mathbf{u}$; we then calculate a spatial correlation function that averages the scalar product of all pairs of velocity fluctuation vectors separated by a distance $R = |\mathbf{R}|$,

$$C_{\mathbf{uu}}(R) \equiv \left\langle \frac{\sum_j \delta\mathbf{u}(\mathbf{r}_j) \cdot \delta\mathbf{u}(\mathbf{r}_j + \mathbf{R})}{\sum_j \delta\mathbf{u}(\mathbf{r}_j) \cdot \delta\mathbf{u}(\mathbf{r}_j)} \right\rangle \quad (5.1)$$

The angle brackets signify an average over all xy directions, and the sums are taken over all positions \mathbf{r}_j [189, 190]. For small R , $C_{\mathbf{uu}}(R)$ decays precipitously from one, as shown by the blue circles in Figure 5.4; this decay is nearly exponential [Figure 5.4, inset], with a characteristic length scale of order one pore [191]. Intriguingly, however, we also observe weak oscillations in $C_{\mathbf{uu}}(R)$ at even larger R ; this indicates the presence of slight, but non-zero, correlations in the flow that persist up to distances spanning several pores. We hypothesize that these oscillations reflect the geometry of the pore space formed by the packing of the beads. To test this idea, we compare the shape of $C_{\mathbf{uu}}(R)$ with that of the pore-space pair correlation function, $f(R)$, of a random packing of beads similar to that comprising our porous medium; this function describes the probability of finding a point of

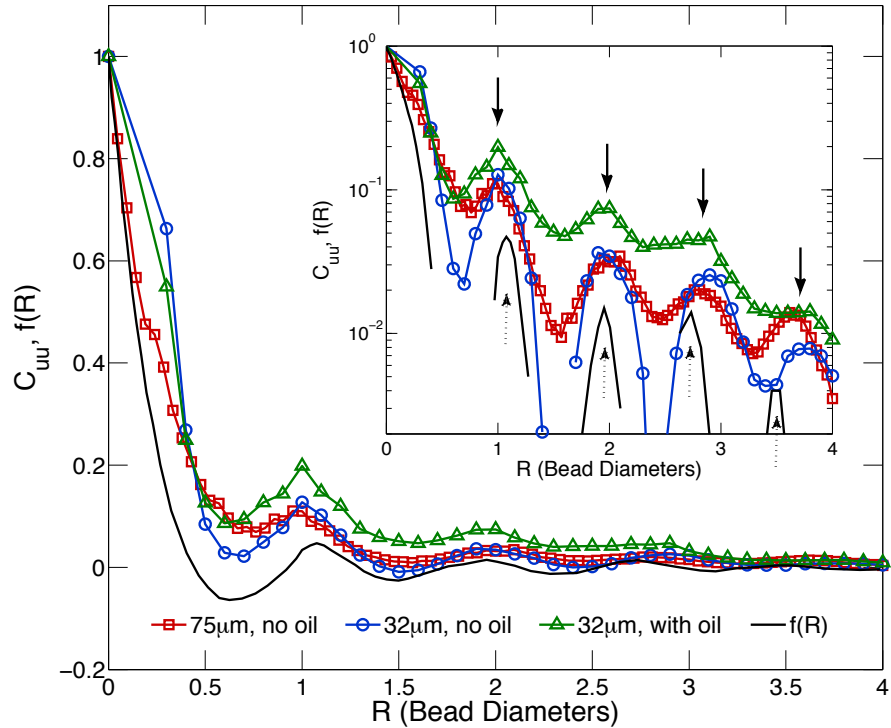


Figure 5.4: Correlations in the flow reflect the geometry of the pore space. Variation of spatial correlation function of velocity fluctuation vectors, $C_{uu}(R)$, or pore-space pair correlation function, $f(R)$, with distance R . Blue circles and red squares are for single-phase flow through media comprised of $32 \mu\text{m}$ and $75 \mu\text{m}$ radius beads, respectively, while green triangles are for flow through the medium comprised of $32 \mu\text{m}$ radius beads, with trapped residual oil. Data for $f(R)$ are taken from [188]. Inset shows the same data, plotted with semilogarithmic axes. Solid arrows indicate positions of peaks in C_{uu} at $R \approx 1, 2, 2.8$, and 3.7 bead diameters, while dashed arrows indicate positions of peaks in $f(R)$ at $R \approx 1.1, 2, 2.7$, and 3.5 bead diameters. Both C_{uu} and $f(R)$ show similar oscillatory behavior, with peaks and troughs at similar locations.

the pore space at a distance R away from another point in the pore space. Similar to $C_{\mathbf{uu}}(R)$, $f(R)$ also shows oscillations [188]; these reflect the local packing geometry of the spherical beads [192]. Moreover, the peaks in $C_{\mathbf{uu}}(R)$ occur at $R \approx 1, 2, 2.8$, and 3.7 bead diameters, as indicated in the inset to Figure 5.4, in excellent coincidence with those observed in $f(R)$. This close agreement confirms that the correlations in the flow are determined by the geometry of the pore space.

This disordered geometry forces each fluid element to follow a tortuous path through the medium, traveling a total distance larger than L . Averaging the distances traveled by all the fluid elements yields an effective distance traveled $\sqrt{\alpha}L$, where $\alpha > 1$, often referred to as the hydrodynamic tortuosity, provides an important and commonly-used measure of the variability of the flow. Acoustic [193], electrical [193], pressure [194], NMR [195, 196, 197], and dispersion [198] measurements, as well as a theoretical calculation [199], yield $\alpha \approx 2$ for a porous medium similar to ours. Within the picture presented here, the distance traveled by each fluid element is approximately $L/\cos^2 \theta$; we thus use our measured velocity orientations [blue circles in Figure 5.2(b)] to directly calculate the tortuosity. We find $\alpha = 1.80$, in good agreement with the previously obtained values. This provides additional confirmation of the validity of our picture.

To test the generality of our results, we perform similar measurements on another 3D porous medium with beads of larger radii, $75 \pm 4 \mu\text{m}$. The average interstitial velocity of the imposed flow is $q/\phi = 34 \mu\text{m/s}$. Similar to the case of the smaller beads, we observe broad, exponentially-decaying velocity pdfs [red squares in Figure 5.2]; moreover, the pdfs for both porous media collapse when the velocities are rescaled by q/ϕ . We again quantify the spatial correlations in the flow using the function $C_{\mathbf{uu}}(R)$. As in the case of

the smaller beads, $C_{\mathbf{uu}}(R)$ decays exponentially for $R < 1$ bead diameter, and also exhibits slight oscillations at even larger R , as shown by the red squares in Figure 5.4. The close agreement between the measurements on both porous media confirms that our results are more general.

5.3 Visualizing multi-phase flow

As described in the previous Chapter, many important situations, such as oil recovery, groundwater contamination, and geological CO₂ storage, involve flow around discrete ganglia of a second, immiscible, fluid trapped within the pore space [1]. This trapping dramatically alters the continuum transport, presumably due to modifications in the pore scale flow [200, 201]. However, investigations of this behavior are woefully lacking; scattering of light from the ganglia surfaces typically precludes direct visualization of the tracer-laden fluid flow around them. We overcome this challenge by formulating a second non-wetting fluid composed of a mixture of hydrocarbon oils, as described in Chapter 2. To trap residual ganglia of the oil, we flow it for 30 min at a rate of 10 mL/hr through the porous medium comprised of the smaller beads; we then reflow the tracer-laden fluid at a rate of 0.1 mL/hr, corresponding to a capillary number $Ca \equiv \mu q / \gamma \approx 10^{-5}$, where $\gamma \approx 13$ mN/m is the interfacial tension between the two fluids. This protocol leads to the formation of discrete ganglia that remain trapped within the pore space, as described in Chapter 4; the ganglia are indicated in Figure 5.1(c) [149]. The tracer-laden fluid continues to flow around these ganglia; we directly visualize this steady-state flow using confocal microscopy, re-acquiring movies of optical sections at the same positions as those obtained prior to oil trapping.

Similar to the previous case without residual trapping, the flow is highly variable, as

illustrated by the map of velocity magnitudes shown in Figure 5.1(c). Because the ganglia occlude some of the pore space, the characteristic speed of the tracer-laden fluid is larger, $\approx 1.2q/\phi$ [green triangles in Figure 5.2(a)]; moreover, because the tracer-laden fluid must flow around the ganglia, more velocities are oriented transverse to the flow direction [green triangles in Figure 5.2(b)]. As in the case without residual trapping, we observe broad, exponentially-decaying pdfs for the velocity components [green triangles in Figure 5.2(c-d)]; however, these pdfs are significantly broader, indicating that residual trapping introduces additional variability to flow within a 3D porous medium. We again use the measured velocity orientations [green triangles in Figure 5.2(b)] to directly calculate the tortuosity, α . Consistent with previous indirect measurements [202], we find $\alpha = 2.24$, higher than the tortuosity measured in the previous case of single-phase flow; this further reflects the additional flow variability introduced by residual trapping.

We quantify the spatial correlations in this flow using the function $C_{\mathbf{uu}}(R)$. Interestingly, as in the previous case without residual trapping, $C_{\mathbf{uu}}(R)$ decays exponentially for $R < 1$ bead diameter, also exhibiting slight oscillations for even larger R at the same positions, as shown by the green triangles in Figure 5.4. This indicates that the flow remains correlated, even when a second immiscible fluid is trapped within the medium; moreover, the structure of these correlations is again determined by the geometry of the pore space.

Our measurements quantify the strong velocity variations in single- and multi-phase flow within a 3D porous medium. We find that the velocity magnitudes and the velocity components both along and transverse to the imposed flow direction are exponentially distributed. Moreover, we present direct evidence that the flow is correlated at the pore scale, and that the structure of these correlations is determined by the geometry of the medium.

The pore space is highly disordered and complex; nevertheless, our results suggest that flow through it is not completely random.

Finally, we note that our measurements of the velocity field within a porous medium may provide a way to predict the mechanical dispersion of molecules dissolved in the flowing fluid; an important example of such a solute is a contaminant that dissolves in a groundwater aquifer. Due to the strong variability in the flow velocities, as the solute molecules are advected along with the fluid, they spread out [1].

Chapter 6

Fluid breakup during simultaneous two-phase flow through a three-dimensional porous medium

In Chapters 3 and 4, we describe one important class of multi-phase flows: forcing one fluid to displace another immiscible fluid from a 3D porous medium. Another important class of multi-phase flows involves the *simultaneous* flow of both a wetting and a non-wetting fluid through the tortuous 3D pore space of the medium. Due to the interfacial tension between the two fluids, they are typically thought to flow through distinct, unchanging, connected pathways [203, 204]; indeed, this idea underlies the interpretation of many multi-phase transport measurements [205]. However, the validity of this assumption remains intensely debated. Experimental measurements on a 2D porous medium suggest that, in some cases, the non-wetting fluid may not simply flow through a connected pathway; instead, it can break up into discrete ganglia, often as small as one pore in size, which

are then advected through the medium by the flowing wetting fluid [206, 207, 208, 209]. However, the pore space of a 2D medium is considerably less connected than that of a 3D medium [20]; this enhances the propensity of the non-wetting fluid to break up in the 2D case [210], and thus, the applicability of such measurements to 3D porous media is unclear. Unfortunately, probing the flow in 3D, at pore-scale resolution, is enormously challenging, due to the opacity of the medium. Consequently, despite its enormous practical importance, a complete understanding of the physics underlying simultaneous two-phase flow through a 3D porous medium remains elusive.

In this Chapter⁵, we use confocal microscopy to directly visualize the simultaneous flow of both a wetting and a non-wetting fluid through a 3D porous medium, at pore-scale resolution. For small flow rates, both fluids flow through unchanging, distinct, connected 3D pathways. At higher flow rates, however, the non-wetting fluid continually breaks up into discrete ganglia; these are then advected through the medium. We find that the transition between connected flow and breakup of the non-wetting fluid is characterized by a state diagram that depends on the capillary numbers of both the wetting and the non-wetting fluids, Ca_w and Ca_{nw} , respectively; these parameters describe the magnitude of the viscous forces exerted by the wetting and the non-wetting fluids, respectively, compared to capillary forces. Our results thus reveal and help elucidate the diversity of behavior that arises in two-phase flow through a 3D porous medium.

⁵Based on “Fluid breakup during simultaneous two-phase flow through a three-dimensional porous medium”, **S. S. Datta**, J. B. Dupin, and D. A. Weitz, to be submitted (2013).

6.1 Visualizing multi-phase flow

We prepare a 3D porous medium composed of beads with radii $a = 36 \pm 2 \mu\text{m}$, in a thin-walled square quartz capillary of cross-sectional area $A = 9 \text{ mm}^2$; the typical radius of a pore is thus $a_p \approx 6 \mu\text{m}$ [113, 114]. The packing has length $L \approx 2 \text{ cm}$ and porosity $\phi \approx 0.41$. We use the non-wetting fluid and the low-viscosity wetting fluid described in Chapter 2 in our experiments.

We first evacuate the porous medium under vacuum and saturate it with CO_2 gas, which is soluble in the wetting fluid, thereby eliminating the formation of trapped bubbles. We then saturate the pore space with the dyed wetting fluid, and first visualize the pore structure within the 3D medium using a confocal microscope. We do this by acquiring optical slices at a fixed z position several bead diameters deep within the medium; each slice is $11 \mu\text{m}$ thick along the z axis and spans a lateral area of $912 \mu\text{m} \times 912 \mu\text{m}$ in the xy plane. We repeatedly acquire slices at multiple locations in the xy plane spanning the entire width and length of the medium; by combining these, we obtain a map of the pore structure over the entire extent of the porous medium. We identify the glass beads by their contrast with the dyed wetting fluid.

To investigate the multi-phase flow, we simultaneously flow both the wetting fluid and the oil at independently-controlled volumetric flow rates, $Q_w = 0.2 \text{ mL h}^{-1}$ and $Q_{nw} = 5.0 \text{ mL h}^{-1}$, respectively; the experimental geometry is schematized in Figure 6.1(a) and Figure 6.2. Because the oil is undyed, we identify it by its additional contrast with the dyed wetting fluid in the imaged pore space. The oil initially flows into the medium through a series of abrupt bursts into the pores, remaining connected as it flows; this behavior indicates that a threshold capillary pressure $\sim \gamma/a_p$ must build up in the oil before it can invade

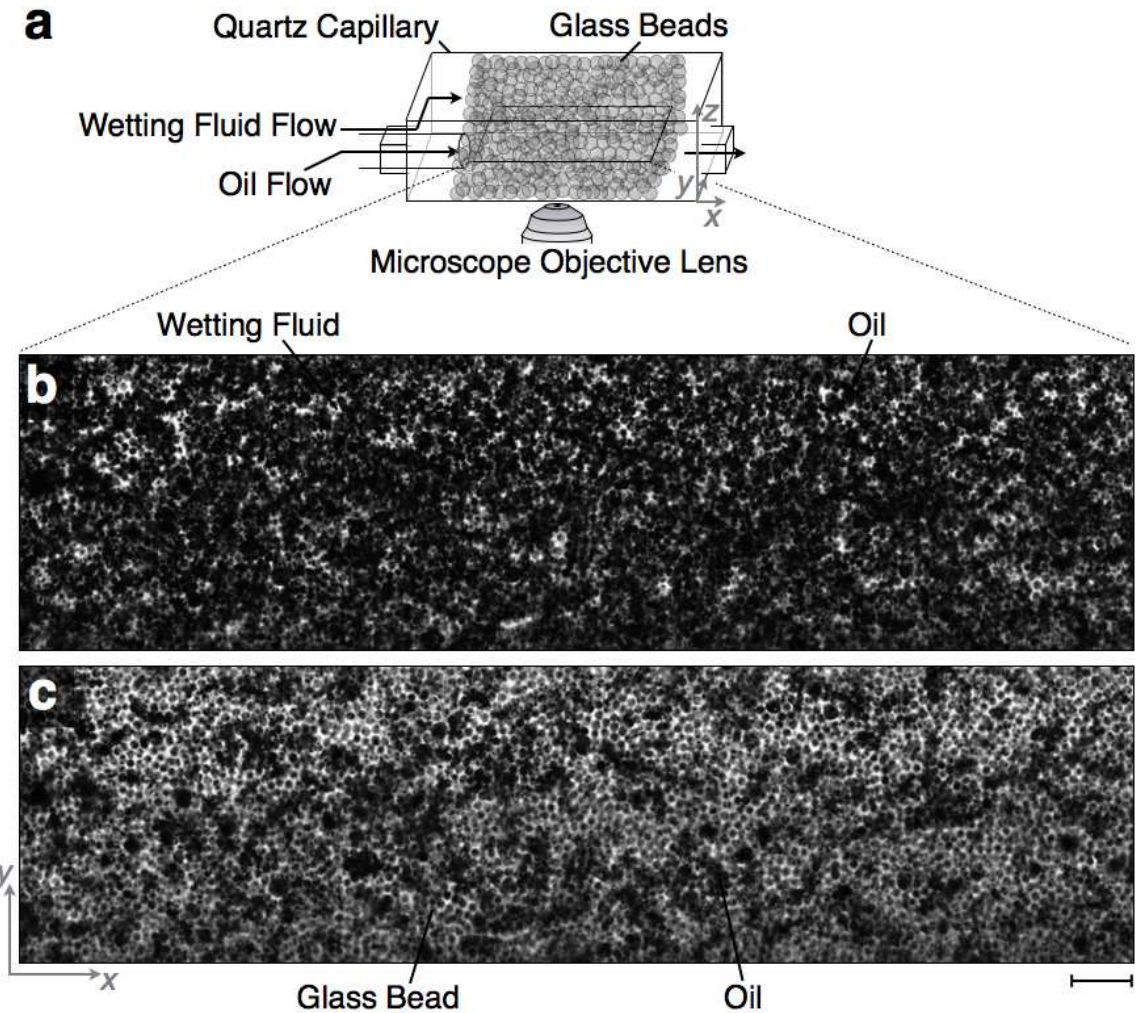


Figure 6.1: Connected flow at low flow rates during simultaneous two-phase flow through a 3D porous medium. (a) Schematic showing porous medium and imaging geometry. The oil flows at a rate Q_{nw} through a circular tube inserted coaxially in a larger square quartz capillary, whereas the wetting fluid flows at a rate Q_w through the interstitial space between the circular tube and the square capillary. A portion of a 2D confocal section within the medium is shown for (b) $Q_w = 0.2 \text{ mL h}^{-1}$ and $Q_{nw} = 5.0 \text{ mL h}^{-1}$, and (c) $Q_w = 50.0 \text{ mL h}^{-1}$ and $Q_{nw} = 5.0 \text{ mL h}^{-1}$. Black circles show beads making up the medium, while additional black regions show a section through the flowing oil. Scale bar is $500 \mu\text{m}$ long. The oil flows through an unchanging, tortuous, connected 3D pathway in both cases; an example of a 3D reconstruction is shown in Figure 6.3. The imposed flow direction is from left to right.

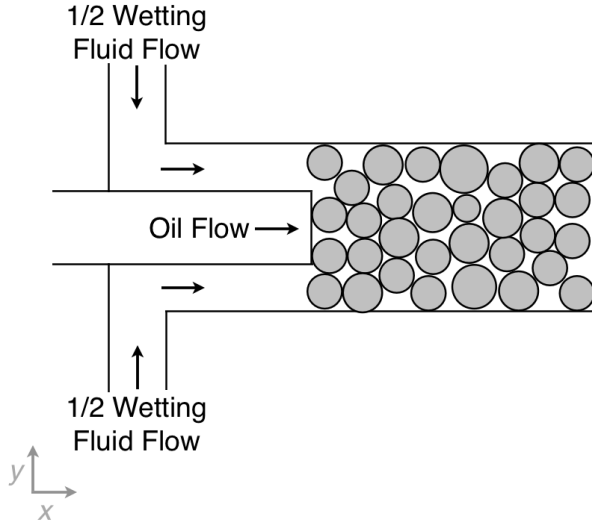


Figure 6.2: Schematic showing inlet geometry used in the experiments. The non-wetting fluid flows through a tube inserted coaxially in the quartz capillary, while the wetting fluid flows in the crevices between the tube and the quartz capillary.

a pore. Because the packing of the beads is disordered, the path taken by the oil is tortuous; once it traverses the entire medium, the oil continues to flow through this unchanging, connected 3D pathway, as exemplified in Figures 6.1(b) and 6.3. We verify that the oil flows through this pathway by monitoring its ejection at the outlet of the porous medium.

To further explore the two-phase flow, we progressively increase the wetting fluid flow rate. For $Q_w < 125.0 \text{ mL h}^{-1}$, the oil slightly reconfigures its flow path each time Q_w is changed [Figure 6.1 (b-c)]; it then continues to flow through this connected 3D pathway. We observe dramatically different behavior at even larger flow rates: instead of simply flowing through a connected 3D pathway, the oil continually breaks up into discrete ganglia, several pores in size, as shown in Figure 6.4(a). The ganglia are then advected through the pore space by the flowing wetting fluid. This is a dynamic process [206, 207]: the oil ganglia continually break up and coalesce, temporarily becoming immobilized at some



Figure 6.3: 3D reconstruction of tortuous, connected oil pathway, during simultaneous flow of oil and a wetting fluid through a 3D porous medium. The beads are not shown for clarity; the red shows the oil as it flows through the pore space. Perspective is looking along the $+x$ direction.

pore entrances and eventually being pushed through others, ultimately becoming mobilized from the medium. These observations contradict the idea that the oil flows through an unchanging, connected pathway [203, 204, 205].

We next investigate the influence of increasing the oil flow rate. We progressively increase Q_{nw} , starting at 0.2 mL h^{-1} , fixing the wetting fluid flow rate at $Q_w = 25.0 \text{ mL h}^{-1}$. The oil again flows through an unchanging, connected 3D pathway, similar to those shown in Figures 6.1(b-c) and 6.3. Similar to the increasing Q_w case, the oil slightly reconfigures its flow path each time Q_{nw} is changed; it then continues to flow through this connected 3D pathway. Intriguingly, at $Q_{nw} = 5.0 \text{ mL h}^{-1}$, sections of this connected 3D pathway intermittently break up into discrete ganglia, several pores in size. At even higher flow rates, we again observe that the oil continually breaks up into discrete ganglia, as shown in Figure 6.4(b). Similar to the breakup observed in the case of increasing Q_w , these ganglia are advected through the pore space by the flowing wetting fluid, and are ultimately mobilized from the medium. Our experiments thus demonstrate that, for sufficiently large fluid flow rates, the two fluids do *not* flow through distinct, unchanging, connected 3D pathways, as is often assumed [203, 204, 205]; instead, we observe a transition to a state in which the oil is continuously broken up into discrete ganglia.

6.2 Understanding the fluid breakup

The first class of connected-to-broken up transition occurs for increasing Q_w . We observe that, as the oil flows into the porous medium, it is quickly broken up into large ganglia, many pores in size; a representative example is shown in the first frame of Figure 6.4(a). The wetting fluid pushes part of this ganglion forward [arrows, first two frames of

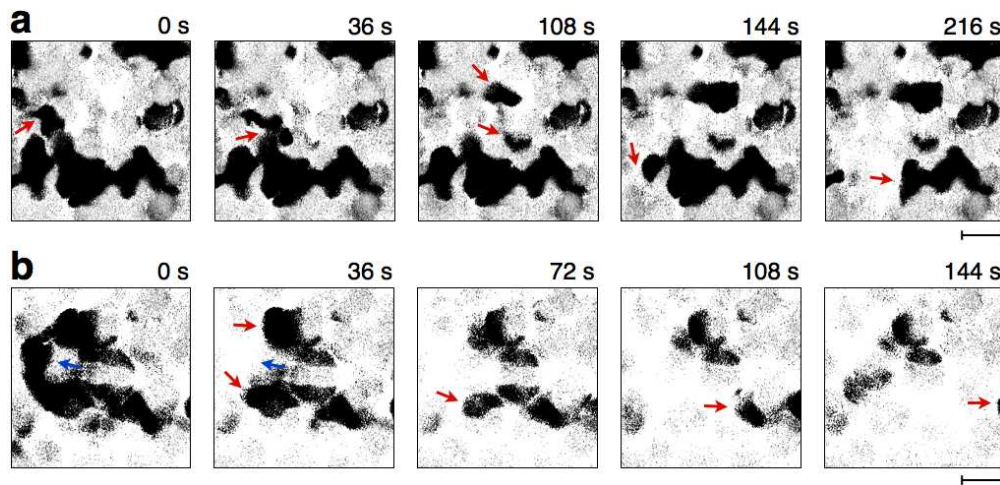


Figure 6.4: Oil breaks up for sufficiently large flow rates during simultaneous two-phase flow through a 3D porous medium. Images show multiple frames, taken at different times, of a single optical slice, with the beads and the pore space subtracted; thus, the dark regions in each frame only show the oil as it flows. The imposed flow direction is from left to right. (a) At $Q_w = 125.0 \text{ mL h}^{-1}$ and $Q_{nw} = 5.0 \text{ mL h}^{-1}$, the wetting fluid breaks the oil up into smaller, discrete ganglia. (b) At $Q_w = 50.0 \text{ mL h}^{-1}$ and $Q_{nw} = 25.0 \text{ mL h}^{-1}$, the oil breaks up as it flows around the beads forming the porous medium. Labels show time elapsed after first frame. Scale bars are $50 \mu\text{m}$ long.

Figure 6.4(a)], ultimately breaking it off. This process forms additional, smaller ganglia [arrows, third frame of Figure 6.4(a)]. The ganglia are eventually advected through the pore space by the flowing wetting fluid [arrows, last two frames of Figure 6.4(a)]. This behavior is reminiscent of drop formation in a microfluidic channel [211, 212], in which the viscous drag exerted by a flowing wetting fluid tears discrete drops off a coflowing oil stream. Moreover, similar to the case of drop formation, we observe that the size of the oil ganglia formed decreases with increasing Q_w . We thus hypothesize that a similar mechanism drives this connected-to-broken up transition. We estimate the pore-scale viscous drag force as $\sim \mu_w q_w a_p$, where $q_w \equiv Q_w / \phi A$ is the average interstitial velocity in the case of single-phase wetting fluid flow. The oil breakup is resisted by the capillary force $\sim \gamma a_p$; balancing these two forces yields a criterion for breakup, $Ca_w \equiv \mu_w q_w / \gamma \geq Ca_w^*$, where Ca_w^* is a threshold capillary number. We thus expect the oil to break up at sufficiently large values of Ca_w , consistent with our experimental observations.

The second class of connected-to-broken up transition occurs for increasing Q_{nw} . This transition is particularly counterintuitive: increasing the flow rate of a non-wetting fluid in a coflowing stream typically *impedes* its breakup into drops [211, 213, 212]. A clue to the physical origin of this transition comes from close inspection of the oil breakup process; a representative example is shown in Figure 6.4(b). As the oil flows, it collides with a bead making up the porous medium, indicated by the blue arrow in the first two frames of Figure 6.4(b). It then flows around the entire bead, breaking up into two smaller ganglia in the process [leftmost red arrows, second frame of Figure 6.4(b)]. These smaller ganglia continue to be advected through the pore space by the flowing wetting fluid [arrows, last three frames of Figure 6.4(b)]. This behavior is reminiscent of the breakup of a non-wetting

fluid as it flows past an obstacle in a microfluidic channel [214, 215]; in such a situation, for small fluid flow rates, the capillary force causes the non-wetting fluid to squeeze into one the gaps around the obstacle, moving past it with breaking. By contrast, at sufficiently large flow rates, the viscous force driving the flow of the non-wetting fluid causes it to flow around the entire obstacle, and the fluid breaks up in the process. We hypothesize that a similar mechanism drives this connected-to-broken up transition. We estimate the pore-scale viscous force driving the oil flow as $\sim \mu_{nw} q_{nw} a_p$, where $q_{nw} \equiv Q_{nw}/\phi A$ is the average interstitial velocity in the case of single-phase oil fluid flow. The pore-scale capillary force is again given by $\sim \gamma a_p$; balancing these two forces yields another criterion for breakup, $Ca_{nw} \equiv \mu_{nw} q_{nw} / \gamma \geq Ca_{nw}^*$, where Ca_{nw}^* is a threshold capillary number. We thus expect the oil to break up at sufficiently large values of Ca_{nw} , consistent with our experimental observations.

6.3 State diagram for the connected-to-broken up transition

Within the picture presented here, the breakup of the oil occurs for sufficiently large values of the wetting fluid and non-wetting fluid capillary numbers, Ca_w and Ca_{nw} , respectively. To rigorously test this hypothesis, we perform similar measurements over a broad range of flow rates ranging from 0.2-250.0 mL h⁻¹, using different fluids characterized by viscosities ranging from 2-110 mPa s, on different 3D porous media characterized by cross-sectional areas ranging from 4-9 mm² and bead radii ranging from 36-60 μ m; we thus vary the capillary numbers over the range $Ca_w \sim 10^{-6} - 10^{-1}$ and $Ca_{nw} \sim 10^{-5} - 10^{-1}$. We

summarize our observations using the state diagram shown in Figure 6.5. In all cases, we observe that the oil flows through an unchanging, connected 3D pathway for small values of Ca_w and Ca_{nw} , shown by the unfilled symbols in Figure 6.5; however, as either Ca_w or Ca_{nw} increase, this pathway begins to intermittently break up, shown by the grey symbols in Figure 6.5. At the largest values of Ca_w or Ca_{nw} , the oil continually breaks up into discrete ganglia, as shown by the black symbols in Figure 6.5. All the data appear to collapse, supporting the validity of our picture.

The first class of connected-to-broken up transition occurs when Ca_w exceeds a threshold value, Ca_w^* ; we use our measurements to estimate this value, $Ca_w^* = 7 \times 10^{-4}$. Interestingly, this value is much smaller than the threshold for drop formation in a microfluidic channel, $Ca_w^* \sim 1$. We speculate that this difference reflects the disordered packing of the beads. Indeed, direct visualization using confocal microscopy shows that, even in the case of single-phase flow, the velocity of the flowing wetting fluid can be over an order of magnitude larger than q_w , due to the tortuosity of the pore space [216]. In our experiments, the co-flowing oil phase occupies a large portion of the pore space, imparting even more variability to the wetting fluid flow. We thus expect that the pore-scale viscous drag forces can be significantly larger than the value we use in our simple estimate, $\mu_w q_w a$; this leads to a corresponding reduction in Ca_w^* .

The second class of connected-to-broken up transition occurs when Ca_{nw} exceeds a threshold value, Ca_{nw}^* ; we use our measurements to estimate this value, $Ca_{nw}^* = 5 \times 10^{-3}$. Interestingly, this value is comparable to the threshold for the breakup of a non-wetting fluid as it flows around an obstacle in a microfluidic channel [214, 215].

Motivated by the collapse of the data in Figure 6.5, we suggest that the connected-

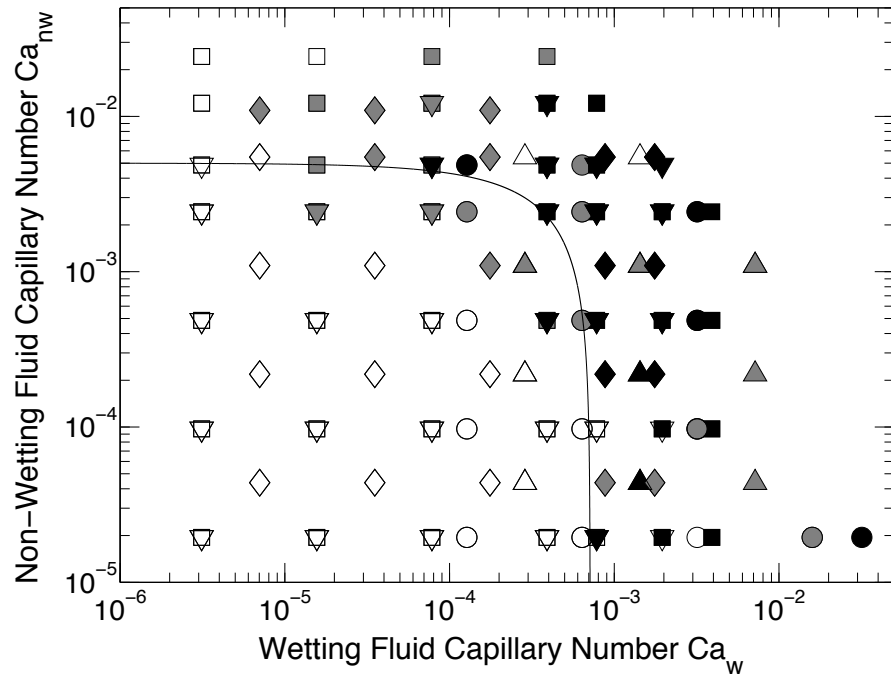


Figure 6.5: State diagram of the connected-to-broken up transition for simultaneous two-phase flow through a 3D porous medium as a function of Ca_w and Ca_{nw} . Open symbols represent flow of the non-wetting fluid through a connected 3D pathway, grey symbols represent intermittent breakup of this pathway, and black symbols represent continual breakup of the oil into discrete ganglia, which are advected through the pore space. Each symbol shape represents a different viscosity, bead size, or porous medium cross-sectional area. Circles: $\mu_w = 110.0 \text{ mPa s}$, $a = 36 \mu\text{m}$, $A = 9 \text{ mm}^2$. Squares: $\mu_w = 2.7 \text{ mPa s}$, $a = 36 \mu\text{m}$, $A = 9 \text{ mm}^2$. Upward triangles: $\mu_w = 110.0 \text{ mPa s}$, $a = 36 \mu\text{m}$, $A = 4 \text{ mm}^2$. Diamonds: $\mu_w = 2.7 \text{ mPa s}$, $a = 36 \mu\text{m}$, $A = 4 \text{ mm}^2$. Downward triangles: $\mu_w = 2.7 \text{ mPa s}$, $a = 60 \mu\text{m}$, $A = 9 \text{ mm}^2$.

to-broken up transition occurs when the sum of the viscous forces exerted on the flowing oil exceeds capillary forces at the pore scale; this can be summarized as $Ca_w/Ca_w^* + Ca_{nw}/Ca_{nw}^* \sim 1$. We find good agreement between this relation and our experimental measurements, as shown by the curve in Figure 6.5. This further supports the validity of the picture presented here.

Our measurements reveal and help clarify the rich behavior that arises when both a wetting and a non-wetting fluid are forced to flow through the pore space simultaneously. Using direct visualization by confocal microscopy, we show that, for sufficiently low fluid flow rates, both fluids flow via distinct, unchanging, connected 3D pathways through the medium, as is typically assumed. At sufficiently large flow rates, however, the non-wetting fluid is continuously broken up into discrete ganglia, which are then advected through the pore space by the wetting fluid. We suggest that this transition occurs when the viscous forces exerted on the flowing non-wetting fluid exceed capillary forces at the pore scale. Such a transition may arise in multi-phase transport measurements, which are often performed at capillary numbers comparable to those explored here [203, 204, 217, 218].

Chapter 7

Rheology of emulsions

Emulsions are suspensions of droplets of one immiscible fluid in another. They are widely used in technological applications requiring the transport and flow of the dispersed fluid; these include oil recovery, food products, pharmacology, coatings, and cosmetics. The droplets are typically stabilized by a surfactant adsorbed on their interfaces; this ensures that there is a short-range repulsive interaction between them, which prevents their coalescence. Such a repulsive emulsion becomes a disordered elastic solid as it is compressed: this behavior can be characterized by the complex shear modulus, $G^*(\omega) = G'(\omega) + iG''(\omega)$, where G' is the storage modulus, G'' is the loss modulus, and ω is the angular frequency. For droplet volume fractions, ϕ , approaching random close packing of spheres, $\phi_{RCP} \approx 0.64$, from below, a repulsive emulsion exhibits a weak elasticity that arises from thermal fluctuations [219]. By contrast, if ϕ is increased above ϕ_{RCP} , the droplets are forced to deform; as a result, the elasticity is determined by the Laplace pressure scale of the droplets, σ/a , where σ is the interfacial tension between the dispersed and continuous phases and a is the average droplet size [219]. Even though it can act as an elastic

solid, such an emulsion can nevertheless be made to flow quite easily: the imposition of sufficiently large shear causes it to yield. This behavior can be elucidated using oscillatory measurements of G' and G'' performed at constant ω and varying maximum strain amplitude γ . The viscoelastic moduli of a repulsive emulsion above ϕ_{RCP} become strain-dependent for sufficiently large γ as the emulsion yields. For increasing γ , the nonlinear G'' exhibits a single, well-defined peak at a strain γ_r^* before falling as $\gamma^{-\nu_r''}$; G' concomitantly decreases as $\gamma^{-\nu_r'}$ with $\nu_r'' \approx \nu_r'/2$ [219, 220, 221]. The pronounced peak in G'' is a characteristic feature of soft glassy materials; it is a direct consequence of a structural relaxation process and thus provides an effective way to characterize yielding [221]. This approach is particularly useful for repulsive emulsions above ϕ_{RCP} , for which the peak in G'' reflects the irreversible rearrangements of the densely-packed droplets [220, 222].

Another widely-encountered class of emulsions is characterized by droplets with additional attractive interactions between them. In stark contrast to the repulsive case, such an attractive emulsion can form an elastic solid even for ϕ well below ϕ_{RCP} [223]; the bonds between droplets result in a connected network of aggregates that can support a shear stress [223, 224, 225, 226]. As a result, an attractive emulsion must exhibit different flow and yielding behavior [227]. However, despite its broad industrial applications, exactly how this behavior occurs is unknown. Thus, measurements of the characteristic γ -dependent yielding of attractive emulsions are essential to elucidate how emulsion rheology depends on interdroplet interactions.

In this Chapter⁶, we explore the rheology of attractive emulsions using oscillatory measurements over a range of ϕ . For increasing γ , $G''(\gamma)$ of attractive emulsions below ϕ_{RCP}

⁶Based on “Rheology of attractive emulsions”, **S. S. Datta**, D. D. Gerrard, T. S. Rhodes, T. G. Mason, and D. A. Weitz, *Physical Review E*, 84, 041404 (2011).

exhibits a single peak at a strain $\gamma_1^* \ll \gamma_r^*$ that increases with ϕ . By contrast, $G''(\gamma)$ of attractive emulsions above ϕ_{RCP} exhibits two peaks at γ_1^* and $\gamma_2^* \approx \gamma_r^*$, unlike the repulsive case; these reflect two distinct structural relaxation processes. The time scales of both of these processes vary with shear rate as $\dot{\gamma}^{-\nu}$ with $\nu \approx 0.8 - 1$. Our results provide insight into the elasticity and yielding of attractive emulsions and highlight the sensitivity of emulsion rheology to attractive interactions.

7.1 Formulation of emulsions

We use emulsions comprised of silicone oil droplets dispersed in formamide, a solvent with negligible evaporation; the droplets are sterically stabilized by Pluronic P105, a non-ionic amphiphilic copolymer [228]. The mechanical measurements are performed at $T = 23^\circ\text{C}$ on strain- or stress-controlled rheometers (TA ARES G2 or Anton Paar Physica MCR 501, respectively) using a parallel-plate geometry. The sample environment is controlled using a solvent trap. The plates are roughened to eliminate wall-slip, and we verify that measurements are independent of the gap size; furthermore, the results are similar to those obtained using a cone-and-plate geometry, indicating that they are not significantly influenced by the non-uniform strain field characteristic of a parallel-plate geometry. We pre-shear the samples prior to each measurement by imposing a 50s^{-1} constant shear-rate flow for 30s, followed by oscillatory shear of γ decreasing from 300% to 0.01% over a period of 230s. We do not observe sample creaming over the measurement duration.

At the temperature and concentrations used here, P105 forms freely-dispersed globular micelles in formamide with radius $a_m = 6.5\text{nm}$, aggregation number $v_m = 31$ and critical micelle concentration $c^* = 20.2\text{mM}$ [229]. These micelles induce attractive depletion

interactions between emulsion droplets [230], whose magnitude at interdroplet contact U we calculate using the Vrij model [231]: $U/k_B T = 4\pi a a_m^2 N_A (c - c^*)/\nu_m$, where a is the average droplet radius, c is the P105 concentration, k_B is Boltzmann's constant, T is temperature, and N_A is Avogadro's number. These interactions preserve a lubricating layer of formamide between the droplets, and hence are pairwise centrosymmetric and do not resist bending. Because ions do not appreciably self-dissociate in formamide, and because we use a non-ionic surfactant, we do not expect electrostatics to play a significant role [232].

To investigate the influence of attraction on the rheology of emulsions, we prepare repulsive emulsions with $U = 0$ ($c = 7\text{mM} < c^*$) and attractive emulsions with $U = 7 - 9k_B T$ ($c = 26.8 - 28.7\text{mM}$) over a range of ϕ using high-shear rate homogenization or sonication with a probe tip. We densify the emulsions using centrifugation and verify that they are stable against coalescence and Ostwald ripening [233]. We measure $\sigma = 6 - 9\text{mN/m}$ using a du Noüy ring. The oil volume fraction ϕ is determined by measuring the masses of all components making up a sample. The droplets have $a = 100, 106, \text{ or } 128\text{nm}$ and relatively low polydispersity $\sim 30 - 35\%$ as measured using dynamic light scattering. We also account for the thickness t of the surfactant layer adsorbed at the droplet surfaces to obtain the effective volume fraction $\phi_{eff} \approx \phi(1 + t/(a - t))^3$. We estimate $t \approx 3.1\text{nm}$ based on neutron scattering data [229, 228] and further verify this by fitting viscosity measurements of dilute repulsive samples to simulation data appropriate for emulsions [220, 234]. This estimate for t is likely to be unchanged even at the highest ϕ studied: the pressure required to compress the surfactant layer $\sim k_B T/s^3$, where πs^2 is the interfacial area per polymer molecule, is approximately two orders of magnitude larger than the maximum osmotic pressure exerted on the droplets $\sim 0.1\sigma/a$ [235, 219].

To test the generality of our results, we also study silicone oil-in-water emulsions stabilized by an ionic surfactant, SDS. All of the data presented in this Chapter are for the oil-in-formamide emulsions stabilized by P105, with the exception of Figures 7.7 and 7.8, which present data for the oil-in-water emulsions stabilized by SDS. These are well-defined and stable model systems characterized by very weak ($< 1k_B T$) or strong ($> 1k_B T$) attractive interdroplet interactions using an SDS concentration only slightly greater than or significantly greater than the critical micelle concentration ($c^* \approx 8\text{mM}$), respectively [230, 219, 236]. We prepare the emulsions using depletion fractionation; the droplets have $a = 250\text{nm}$ and have low polydispersity $\sim 10\%$. To investigate the influence of attraction on the rheology of emulsions, we study repulsive emulsions with $U < 1k_B T$ ($c = 10\text{mM}$) and attractive emulsions with $U \approx 21k_B T$ ($c = 200\text{mM}$). The effective volume fraction ϕ_{eff} is defined to incorporate the effects of the thin liquid film between adjacent droplets due to their electrostatic repulsion. We study the emulsions using oscillatory rheology on a strain-controlled rheometer using a roughened cone-and-plate geometry with a vapor trap. Further details and the rheology data for the SDS-stabilized repulsive emulsions are presented in [219, 236].

7.2 Frequency-dependent mechanical response

The elastic behavior of emulsions is characterized by a ω -independent regime of $G'(\omega)$; two examples, a repulsive emulsion with $\phi_{eff} = 0.70$ and an attractive emulsion with $\phi_{eff} = 0.73$, are shown in the top curves of Figures 7.1 and 7.2, respectively. Repulsive emulsions are solid-like when packed above ϕ_{RCP} but become fluid-like as ϕ_{eff} is decreased below ϕ_{RCP} [Figure 7.1] [219]. By contrast, attractive emulsions are solid-like over a wider

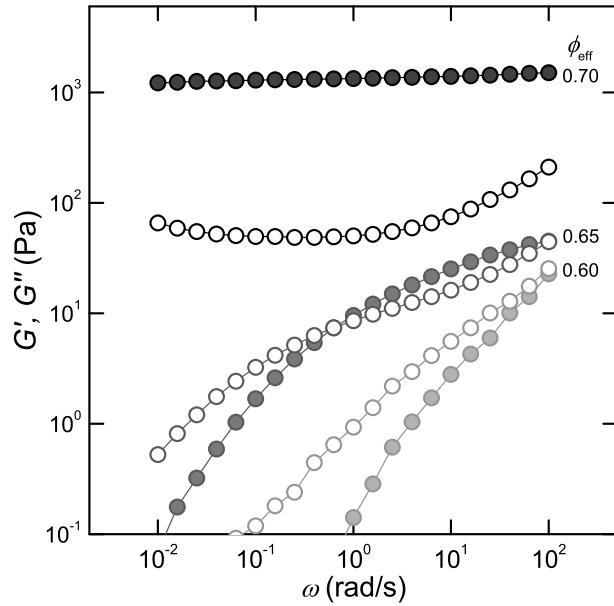


Figure 7.1: Repulsive emulsions become fluid-like below random close packing. Linear storage and loss moduli, $G'(\omega)$ (solid points) and $G''(\omega)$ (open points), of repulsive emulsions with $U = 0$, $a = 128\text{nm}$, and $\phi_{eff} \approx 0.70, 0.65$, and 0.60 (progressively lighter colors).

range of ϕ_{eff} [Figure 7.2]. To summarize this behavior, we plot the plateau modulus G'_p , measured at $\omega = 1 \text{ rad/s}$, as a function of ϕ_{eff} . Above ϕ_{RCP} , G'_p has the same magnitude for both attractive and repulsive emulsions as shown in Figure 7.3. This indicates that the elasticity in both cases is dominated by the repulsive forces deforming the droplets. However, G'' is an order of magnitude larger for attractive emulsions, as compared to the repulsive case [Figure 7.3]. For repulsive emulsions, G'_p drops precipitously as ϕ_{eff} is decreased below ϕ_{RCP} , indicating that the droplets are no longer compressed [219]; by contrast, the elasticity of attractive emulsions persists far below ϕ_{RCP} , as shown by the upper symbols in Figure 7.3.

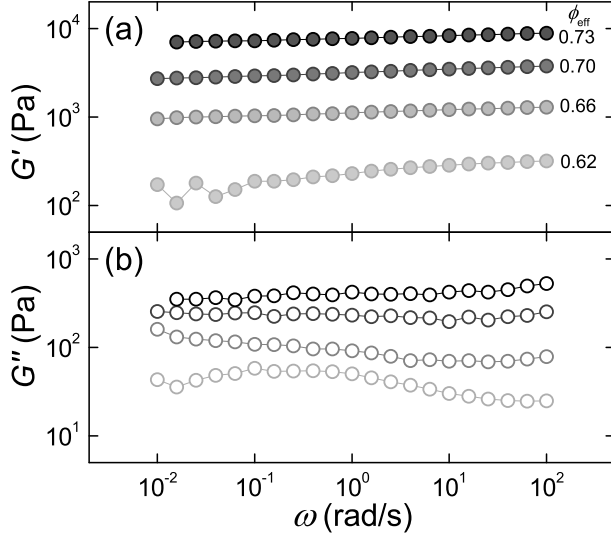


Figure 7.2: Attractive emulsions are elastic both above and below random close packing. Linear storage and loss moduli, (a) $G'(\omega)$ and (b) $G''(\omega)$, of attractive emulsions with $U \approx 9k_B T$, $a = 100\text{nm}$, and $\phi_{eff} \approx 0.73, 0.70, 0.66$, and 0.62 (progressively lighter colors). For clarity, G' and G'' data are multiplied by a factor of 0.5, 0.2, or 0.07 for $\phi_{eff} = 0.70, 0.66$, or 0.62 , respectively.

7.3 Strain-dependent mechanical response

To elucidate the microscopic mechanisms for emulsion flow, we investigate the yielding of emulsions with different ϕ_{eff} by measuring the γ -dependence of G' and G'' at $\omega = 1$ rad/s. Repulsive emulsions above ϕ_{RCP} begin to yield at $\gamma_r^* \sim 10\%$ and G'' exhibits a single, well-defined peak at this strain, as indicated by the arrow in Figure 7.4 [219, 220, 221]. Attractive emulsions above ϕ_{RCP} begin to yield at much smaller strain. Unexpectedly, G'' exhibits two well-defined peaks, a first at $\gamma_1^* \sim 1\% \ll \gamma_r^*$ and a second at $\gamma_2^* \approx \gamma_r^*$, before falling as $\gamma^{-\nu''}$, as indicated by the arrows in Figure 7.5(b). Correspondingly, G' decreases weakly for $\gamma > 0.5\%$ before falling as $\gamma^{-\nu'}$ for $\gamma > 10\%$, with $\nu'' \approx \nu'/2$ [Figure 7.5(a)]. By contrast, G'' of attractive emulsions below ϕ_{RCP} only exhibits a single peak at γ_1^* , as

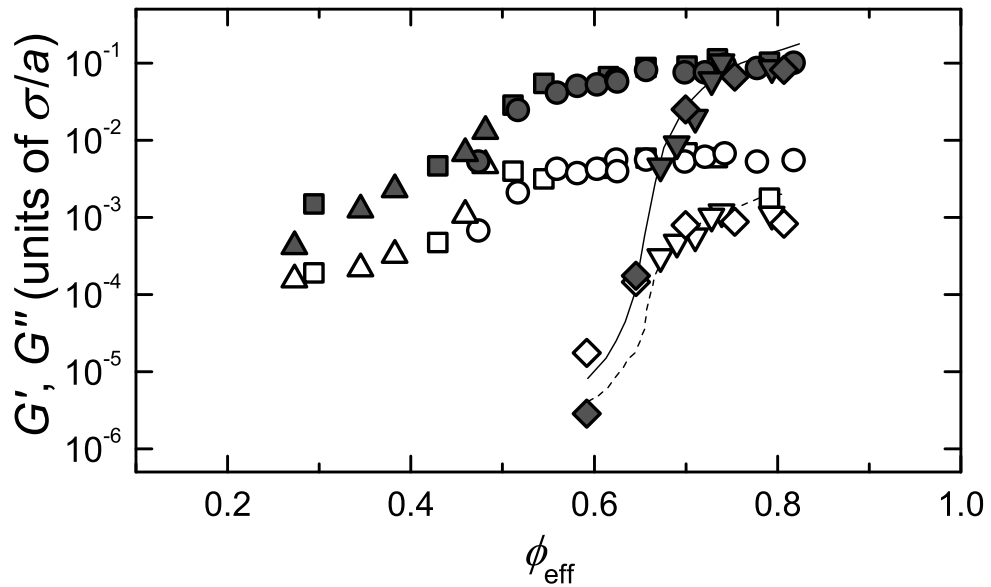


Figure 7.3: Elasticities of attractive and repulsive emulsions differ below random close packing but are similar above it. Linear storage and loss moduli, G'_p (solid points) and G'' (open points), measured at $\omega = 1$ rad/s, normalized by the Laplace pressure σ/a , for both attractive and repulsive emulsions of varying ϕ_{eff} . Attractive emulsions have $a = 128\text{nm}$, $U \approx 9k_B T$ (circles), $a = 106\text{nm}$, $U \approx 7k_B T$ (upward triangles), and $a = 100\text{nm}$, $U \approx 9k_B T$ (squares); repulsive emulsions have $a = 128\text{nm}$ (diamonds) and $a = 106\text{nm}$ (downward triangles). The interfacial tension $\sigma = 6 - 9\text{mN/m}$ for the range of surfactant concentrations used. Previous measurements of G'_p (solid line) and G'' (dashed line) for monodisperse repulsive emulsions [219], horizontally shifted to account for polydispersity, agree with our data. We find $\phi_{RCP} \approx 0.68 - 0.72$, characteristic of ϕ_{RCP} for spheres of comparable polydispersity [237].

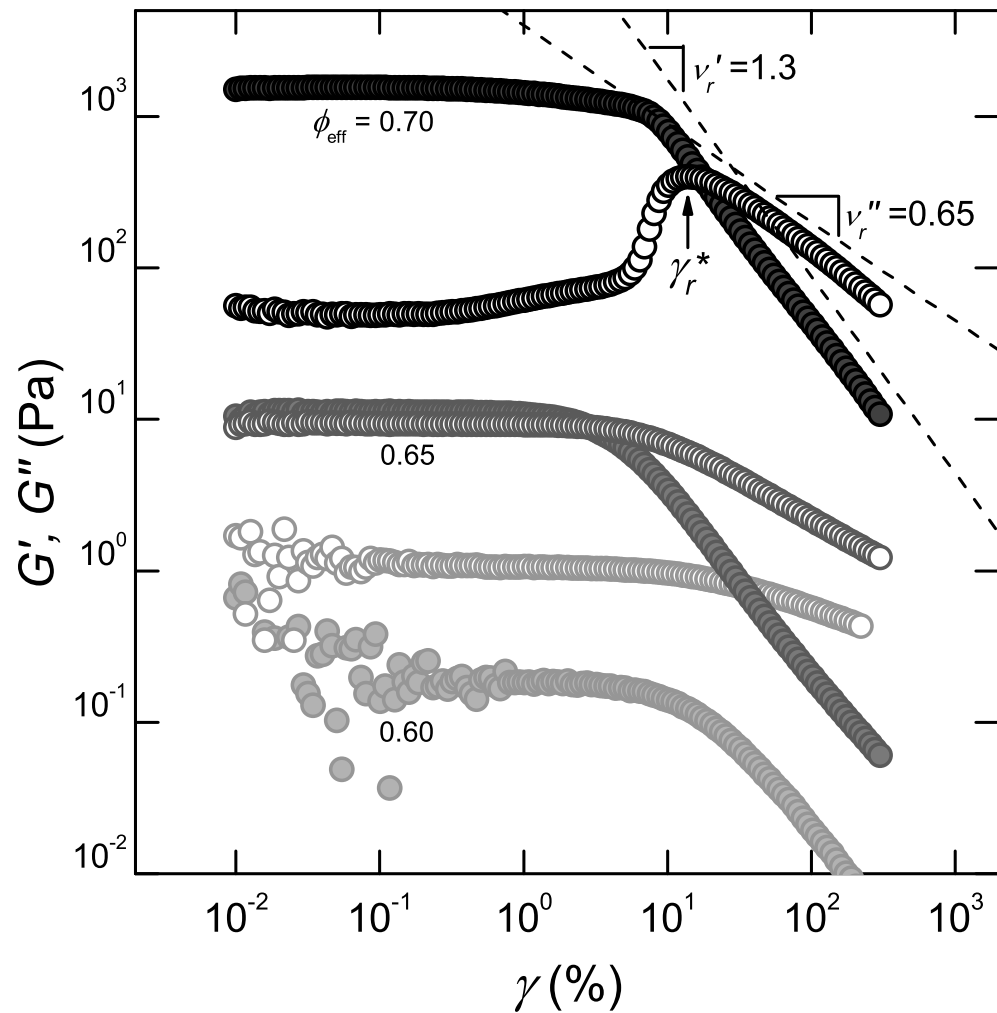


Figure 7.4: **Repulsive emulsions above random close packing exhibit one peak in $G''(\gamma)$ at γ_r^* while those below random close packing do not exhibit a peak in $G''(\gamma)$.** Viscoelastic moduli $G'(\gamma)$ and $G''(\gamma)$ measured at $\omega = 1$ rad/s of repulsive emulsions with $U = 0$, $a = 128$ nm, and $\phi_{eff} \approx 0.70, 0.65$, and 0.60 (progressively lighter colors).

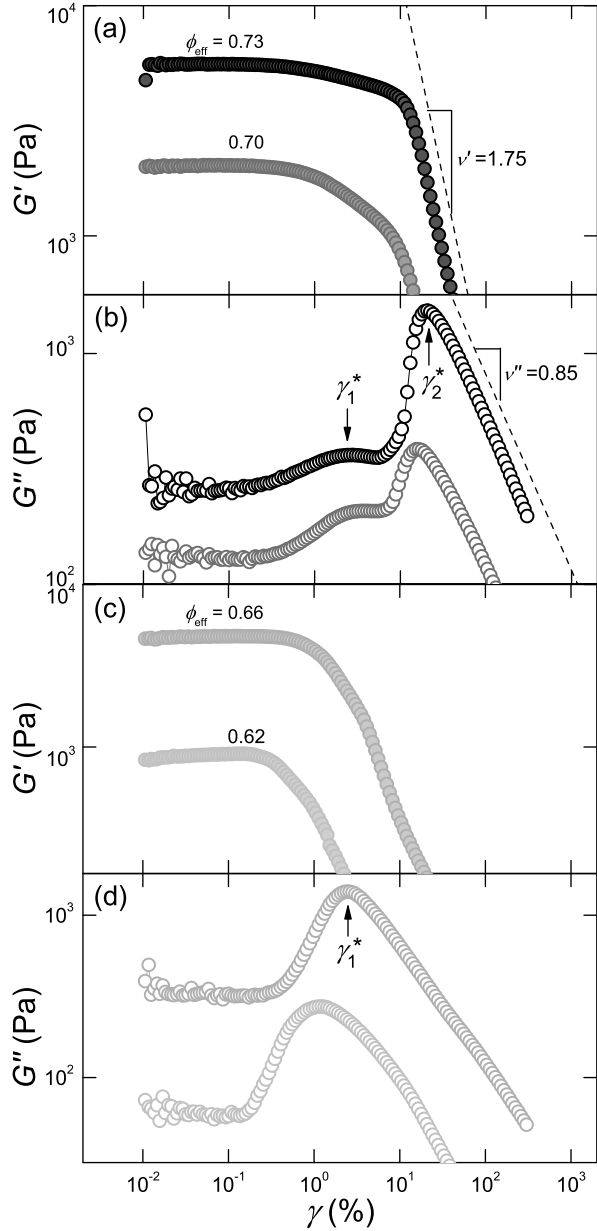


Figure 7.5: Attractive emulsions above random close packing exhibit two peaks in $G''(\gamma)$ at γ_1^* and γ_2^* while those below random close packing exhibit one peak at γ_1^* . Viscoelastic moduli $G'(\gamma)$ and $G''(\gamma)$ measured at $\omega = 1$ rad/s of attractive emulsions with $U \approx 9k_B T$ and $a = 100$ nm (a-b) above ϕ_{RCP} ($\phi_{eff} \approx 0.73$ and 0.70 , progressively lighter colors) and (c-d) below ϕ_{RCP} ($\phi_{eff} \approx 0.66$ and 0.62 , progressively lighter colors). For clarity, G' and G'' data are multiplied by a factor of $0.7, 0.3, 0.8$, or 0.2 for each ϕ_{eff} going from top to bottom. Straight lines indicate $G', G'' \sim \gamma^{-\nu', -\nu''}$ for large γ .

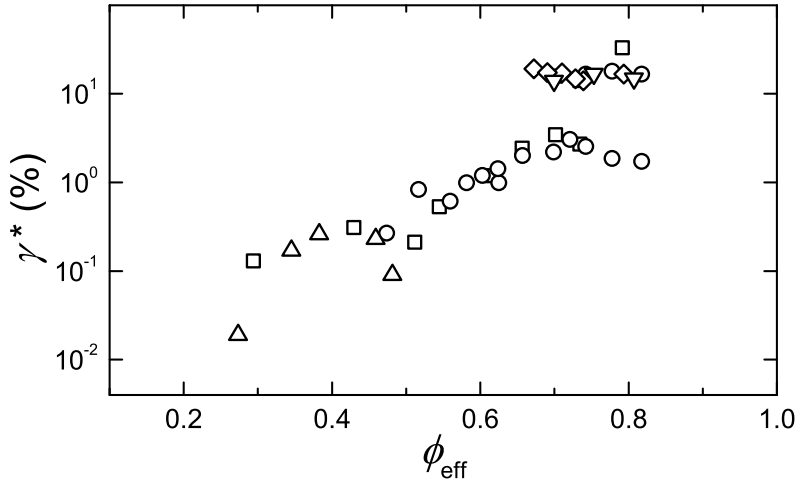


Figure 7.6: Position of peaks in $G''(\gamma)$ for varying ϕ_{eff} . Lower symbols represent γ_1^* , upper symbols represent either γ_2^* or γ_r^* . Attractive emulsions have $a = 128\text{nm}$, $U \approx 9k_B T$ (circles), $a = 106\text{nm}$, $U \approx 7k_B T$ (upward triangles), and $a = 100\text{nm}$, $U \approx 9k_B T$ (squares); repulsive emulsions have $a = 128\text{nm}$ (diamonds) and $a = 106\text{nm}$ (downward triangles).

shown in Figure 5(d), and G' decreases smoothly for $\gamma > 0.01 - 1\%$ [Figure 7.5(c)].

To understand these results, we examine the ϕ_{eff} -dependence of γ_1^* . Below ϕ_{RCP} , γ_1^* decreases with decreasing ϕ_{eff} , as shown by the lower symbols in Figure 7.6; interestingly, this is similar to behavior predicted for particulate colloidal gels connected by “weak links” [238]. The elasticity of these emulsions results from the attractive interdroplet bonds; these induce the formation of a stress-bearing connected network comprised of compact droplet aggregates [224, 225, 226]. We expect the elasticity to be dominated by the weakest bonds in the network, and hence yielding begins when these are broken. In this picture, a macroscopic deformation ΔL deforms such a bond by $\Delta L/(L/\zeta)$, where L is the system size and ζ is the characteristic distance between the weakest bonds. The force on such a bond is thus $k_a \Delta L/(L/\zeta) = k_a \zeta \gamma$, where k_a is the characteristic bond stiffness. Assuming that the bond breaks at a fixed critical force $F^* = k_a \zeta \gamma_1^*$, the critical strain amplitude $\gamma_1^* \propto \zeta^{-1}$. Our mea-

surements of γ_1^* thus imply that ξ increases with decreasing ϕ_{eff} , suggesting that yielding begins at fewer, sparser weak points as ϕ_{eff} is decreased. This may reflect the changing connectivity of the emulsion: the characteristic size ξ of the droplet aggregates comprising the emulsion also increases with decreasing ϕ_{eff} [224, 226]. If the bonds between droplet aggregates are the weakest in the emulsion [239, 240], we would expect $\zeta \approx \xi$ to increase with decreasing ϕ_{eff} , consistent with our results.

For increasing γ , attractive emulsions both below and above ϕ_{RCP} begin to yield and exhibit a peak in G'' at $\gamma \sim \gamma_1^*$; in contrast, those above ϕ_{RCP} exhibit an additional peak in G'' at $\gamma \sim \gamma_2^*$ [Figure 7.5]. This observation implies the existence of an additional process by which the structure of these emulsions must relax before they can flow. This is likely due to the compression of the droplets: above ϕ_{RCP} , attractive emulsions require larger strain to fully yield through the irreversible rearrangements of densely-packed droplets, just as in the repulsive case [220, 222]. This hypothesis is supported by our observation that $\gamma_2^* \approx \gamma_r^*$. The height of the first yielding peak in $G''(\gamma)$ decreases as ϕ_{eff} increases above ϕ_{RCP} , as shown in Figure 7.5(b), reflecting the increasing relative importance of these repulsive interactions as the droplets are increasingly compressed [241].

To test the generality of these results, we perform similar measurements on an oil-in-water emulsion stabilized by a different surfactant. The droplets are electrostatically stabilized by SDS, an ionic surfactant that also forms freely-dispersed globular micelles, and have low polydispersity ($\sim 10\%$) [219, 236]. Similar to the case of P105-stabilized emulsions, G'_p measured for the SDS-stabilized emulsions has the same magnitude for both attractive and repulsive emulsions packed above $\phi_{RCP} \approx 0.64$ [Figure 7.7(a)]; this indicates that the elasticity is dominated by the repulsive forces deforming the droplets.

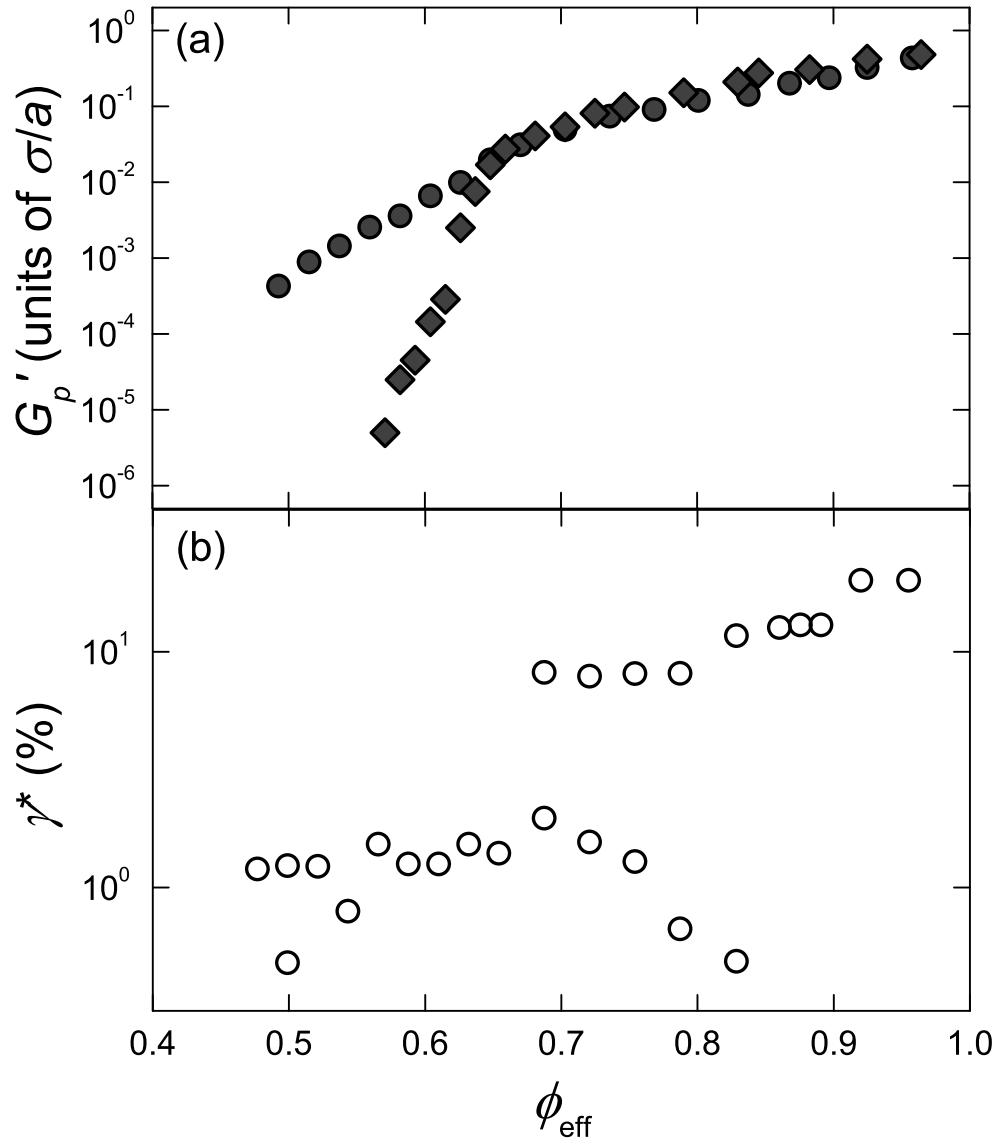


Figure 7.7: Volume fraction-dependent behavior is similar for oil-in-water emulsions stabilized by SDS. (a) Linear plateau storage modulus, G'_p [236], normalized by the Laplace pressure σ/a and (b) position of peaks in $G''(\gamma)$, for varying ϕ_{eff} . Emulsions have $a = 250\text{nm}$; attractive emulsions have $U \approx 21k_B T$ (circles) while repulsive emulsions have $U < 1k_B T$ (diamonds). The interfacial tension $\sigma = 9.8\text{mN/m}$ for the range of surfactant concentrations used. Upper symbols in (b) represent γ_2^* while lower symbols represent γ_1^* .

For the repulsive emulsions, G'_p drops precipitously as ϕ_{eff} is decreased below ϕ_{RCP} ; by contrast, the elasticity of the attractive emulsions persists far below ϕ_{RCP} [Figure 7.7(a)]. Moreover, $G''(\gamma)$ of SDS-stabilized attractive emulsions above ϕ_{RCP} exhibits two peaks at strains $\gamma_1^* \sim 1\% \ll \gamma_r^*$ and $\gamma_2^* \approx \gamma_r^*$, as indicated in Figure 7.8(b). Correspondingly, G' decreases weakly for $\gamma > 0.5\%$ before falling more quickly for $\gamma > 10\%$ [Figure 7.8(a)]. By contrast, $G''(\gamma)$ of the attractive emulsions below ϕ_{RCP} exhibits a single peak at a strain γ_1^* , and G' decreases smoothly for $\gamma > 1\%$ [Figure 7.8]. These data are similar to those obtained for P105-stabilized emulsions; this confirms that our results are more general.

7.4 Time scales of the structural relaxation

The frequency-dependent mechanical response of emulsions directly reflects the time scales of their structural relaxation. For repulsive emulsions above ϕ_{RCP} , $G''(\omega)$ exhibits a shallow minimum at $\omega \sim 0.1 - 10$ rad/s resulting from the combination of viscous loss at high ω and the configurational rearrangements of the individual droplets at low ω [Figure 7.1] [219, 221]. In contrast, for attractive emulsions, $G''(\omega)$ exhibits a minimum at $\omega_{min} \geq 10$ rad/s, as shown in Figure 7.2. This further suggests that attractive interactions alter the structural relaxation of emulsions.

The structural relaxation process through which attractive emulsions yield occurs at frequencies much lower than is accessible in a linear rheological measurement, typical of soft glassy materials [221]. We circumvent this problem by performing ω -dependent measurements holding the strain rate amplitude $\dot{\gamma} = \gamma\omega$ constant for different values of $\dot{\gamma}$. A relaxation process of time scale τ gives rise to a peak in $G''(\omega)$ at a frequency proportional to τ^{-1} [221]. We observe one peak in $G''(\omega)$ for attractive emulsions with $\phi_{eff} < \phi_{RCP}$.

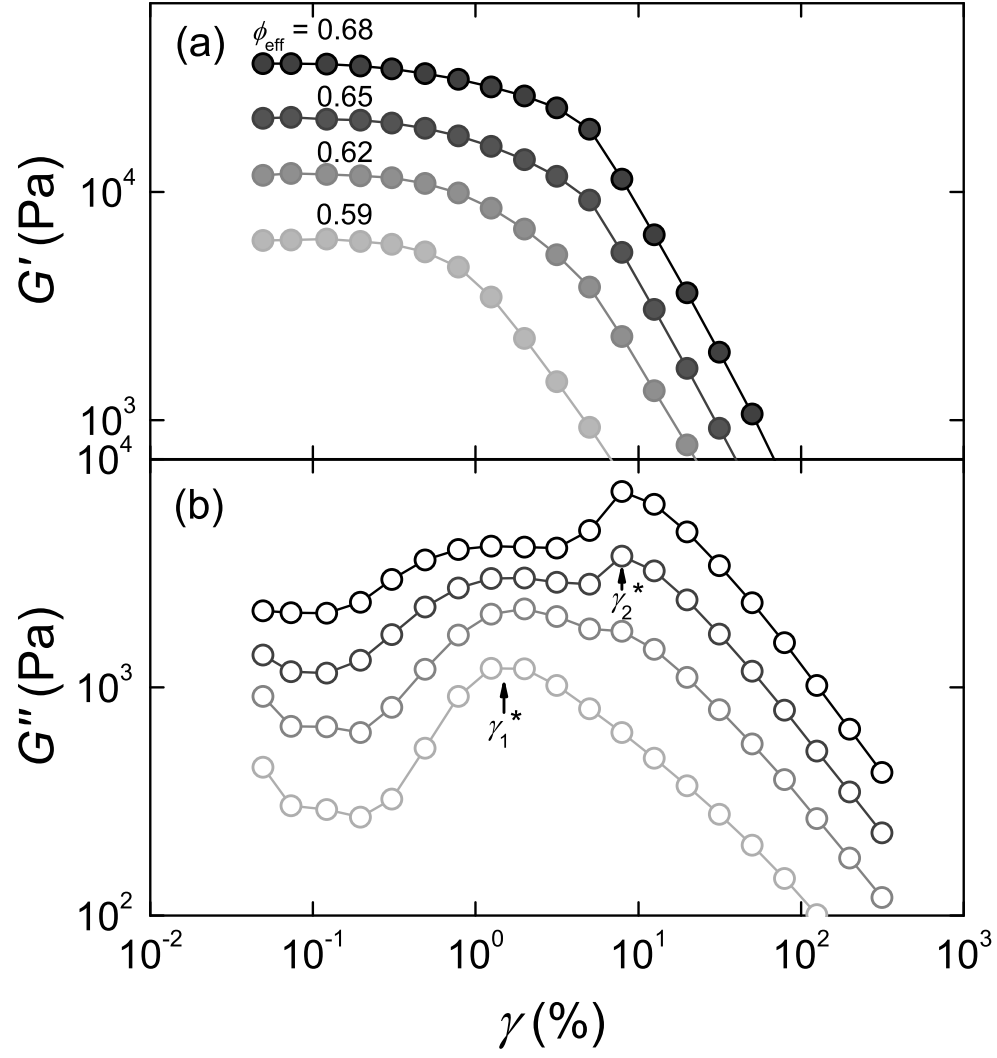


Figure 7.8: Strain-dependent behavior is similar for oil-in-water emulsions stabilized by SDS. Viscoelastic moduli (a) $G'(\gamma)$ and (b) $G''(\gamma)$ of attractive emulsions stabilized by SDS with $U \approx 21k_B T$ and $a = 250\text{nm}$ for $\phi_{eff} \approx 0.68, 0.65, 0.62$, and 0.59 (progressively lighter colors). Emulsions above ϕ_{RCP} (top two curves) show peaks in G'' at γ_1^* and γ_2^* while those below ϕ_{RCP} (lower two curves) show a single peak at γ_1^* . For clarity, G' and G'' data are multiplied by a factor of 0.7, 0.6, or 0.5 for $\phi_{eff} = 0.65, 0.62$, or 0.59 , respectively.

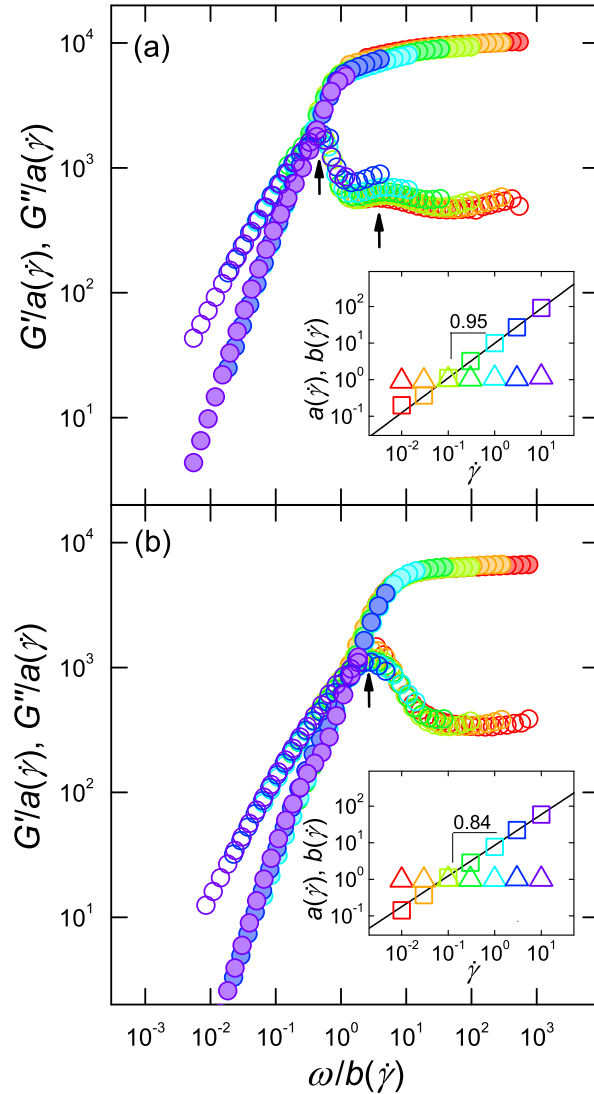


Figure 7.9: Yielding of attractive emulsions is a shear-driven process. Constant $\dot{\gamma}$ frequency sweep measurements of viscoelastic moduli $G'(\omega)$ (solid points) and $G''(\omega)$ (open points) for two samples with $a = 100\text{nm}$ and $U \approx 9k_B T$ above ϕ_{RCP} (a, $\phi_{eff} \approx 0.73$) and below ϕ_{RCP} (b, $\phi_{eff} \approx 0.66$), shifted onto a single master curve by normalizing by the shear-rate-dependent shift factors $a(\dot{\gamma})$ and $b(\dot{\gamma})$. Inset: corresponding amplitude and frequency shift factors $a(\dot{\gamma})$ (triangles) and $b(\dot{\gamma})$ (squares).

strikingly, we observe two peaks in $G''(\omega)$ for those with $\phi_{eff} > \phi_{RCP}$, as indicated in Figure 7.9, in stark contrast to the repulsive case [221]. This provides further confirmation that attractive emulsions above ϕ_{RCP} undergo an additional relaxation process during yielding.

The data measured at different $\dot{\gamma}$ can be scaled onto a master curve by rescaling the moduli and frequency, as shown in Figure 7.9. The frequency scaling factor $b(\dot{\gamma}) \sim \tau^{-1}$ [221]. We explore its dependence on $\dot{\gamma}$ to directly probe how the time scales of the structural relaxation processes of attractive emulsions depend on shear rate. We find $b(\dot{\gamma}) \sim \tau^{-1} \sim \dot{\gamma}^\nu$ with $\nu \approx 0.8 - 1$ for both relaxation processes in attractive emulsions having ϕ_{eff} both below and above ϕ_{RCP} ; two representative examples are shown in Figure 7.9 (inset). This shear-driven behavior is similar to the yielding of colloidal gels [242] and to the yielding of repulsive emulsions above ϕ_{RCP} [221].

Our data suggest a simple physical picture of emulsion flow. The rheology of emulsions with slippery bonds of magnitude $U < 1k_B T$ is similar to that of repulsive emulsions; in stark contrast, emulsions with $U > 7k_B T$ show a dramatically enhanced elasticity below ϕ_{RCP} . Moreover, their nonlinear rheology is markedly different from the repulsive case. These attractive emulsions begin to yield under sufficient shear through the breakage of interdroplet bonds at weak points in the emulsion [227]. Attractive emulsions above ϕ_{RCP} also undergo shear-induced configurational rearrangements of the densely-packed droplets, similar to the repulsive case, at larger strain. This is reminiscent of the two-step yielding of attractive colloidal glasses [243]. How this behavior changes with intermediate values of U remains to be explored.

Emulsions are often used to model many other diverse physical systems and are crucial in various technological processes. We find that their linear and nonlinear rheology depend

sensitively on the interactions between the droplets. Our results may thus be a useful input to such models and could help guide processes designed to control emulsion elasticity and flow behavior.

Chapter 8

Buckling and crumpling of nanoparticle-coated droplets

Suspensions of fluid droplets coated with solid colloidal particles are commonly known as “Pickering” emulsions. Particles with suitable surface chemistries can adsorb at the droplet surfaces strongly, with an energy of up to hundreds of $k_B T$. As a result, Pickering emulsion droplets can be exceptionally stable against coalescence and Ostwald ripening, making them useful for a wide variety of applications in which their interfacial properties play a key role. For example, Pickering emulsion droplets are promising candidates for encapsulating, delivering, or controllably releasing poorly soluble drugs [244]. They have also been used as templates for fabricating hierarchical porous materials for catalysts or filters [245].

The stability of Pickering emulsion droplets is due to the dense packing of a strongly bound layer of colloidal particles at the fluid-fluid interface [246, 247]; this layer is hypothesized to behave as a two-dimensional solid [248, 249, 250, 251, 252]. However,

experimental approaches to verifying this suggestion have been limited to *flat* fluid interfaces [249, 253, 254, 255, 256]. The solid-like nature of particle-coated surfaces is also often used to describe the curved interfaces of fluid droplets; for example, this assumption is essential to the interpretation of rheological measurements of densely packed Pickering emulsions [251]. Nevertheless, direct experimental evidence of the solid-like nature of the surface of particle-coated droplets remains lacking.

An unambiguous way to confirm the solid-like behavior of a thin shell is to observe buckling when it is strongly deformed. For example, as the volume of a thin elastic shell is reduced, compressive stresses build up on its surface, causing localized mechanical instabilities such as sharp points and bends to develop [257]. The proliferation of these localized instabilities results in a shell with a crumpled morphology. The crumpling of fluid-filled shells has been achieved experimentally either by uncontrollably dissolving or by evaporating the interior fluid for several porous capsules [258, 259, 260, 261], or by using an externally imposed osmotic pressure [262, 263]. Few such studies exist for Pickering emulsions [264]. A method to controllably induce compressive stresses at Pickering emulsion droplet surfaces is thus highly desirable to directly test their mechanical properties.

In this Chapter⁷, we study the structural transitions of large numbers of nanoparticle-coated droplets as fluid is controllably pumped out of the droplet interiors. We find that a significant fraction of droplets buckle or crumple upon volume reduction, confirming the hypothesis that their interfaces behave like solids. The number of non-spherical droplets as well as the resultant droplet morphology is highly dependent on the amount of volume reduction and the average size of the droplets. All of the morphologies we observe are sta-

⁷Based on “Controlled buckling and crumpling of nanoparticle-coated droplets”, **S. S. Datta**, H. C. Shum, and D. A. Weitz, *Langmuir*, 26, 18612 (2010).

ble over a period of at least several hours. Many of these are strikingly similar to structures observed or predicted for buckled thin continuum elastic shells. The technique presented here provides a new and straightforward way to study the deformation behavior of thin fluid-filled granular shells.

8.1 Formulation of Pickering emulsions

Ethylene glycol (anhydrous, 99.8%, Sigma-Aldrich), chlorobenzene (CHROMASOLV, for HPLC, 99.9%, Sigma-Aldrich), glycerol (ACS reagent, 99.5%, Sigma-Aldrich), and hydrophobic silica nanoparticles (diameter $\approx 15 \text{ nm} \pm 30\%$, Tol-ST, Nissan Chemical Inc.) were used as received. Some samples were made using ethylene glycol and chlorobenzene dried by tumbling with molecular sieves (3 Å, beads, 4-8 mesh, Sigma-Aldrich) and filtered with a 0.2 μm filter. The samples prepared with the dried reagents showed no noticeable difference in the final results, as compared to samples prepared with reagents used as received.

Emulsions were produced at a volume fraction of $\sim 61\%$ by mixing known masses of ethylene glycol containing 1% glycerol (to minimize Ostwald ripening) and chlorobenzene containing a suitable amount of nanoparticle suspension. These were mechanically agitated by intensive vortexing for 10-40 minutes. This procedure forms extremely stable “water-in-oil” emulsions with ethylene glycol/glycerol as the dispersed phase and chlorobenzene as the continuous phase. This suggests that the silica nanoparticles have a contact angle close to 90° , but are more preferentially wet by chlorobenzene [265]. Furthermore, these samples have surprisingly low polydispersities ($\sim 30\%$) given the inhomogeneous shear rates that arise during emulsification.

Ethylene glycol is partially soluble in chlorobenzene at a concentration of $\sim 1.5 \mu\text{L g}^{-1}$. This is determined in two ways. First, the conductivities of both unsaturated chlorobenzene (σ_{unsat}) and chlorobenzene that has been saturated with ethylene glycol (σ_{sat}) were measured, as well as the conductivity of ethylene glycol (σ_{EG}). The saturation concentration of ethylene glycol in chlorobenzene (c_{sat}) was then calculated by linearly interpolating between σ_{unsat} and σ_{EG} using the relation $\sigma_{sat} \approx \sigma_{unsat} + c_{sat} \sigma_{EG}$. Second, the saturation concentration was directly measured by mixing measured amounts of ethylene glycol with chlorobenzene until the resulting solution is no longer visibly homogenous. Values of saturation concentration of ethylene glycol in chlorobenzene from the two measurements are in good agreement.

To controllably pump a known volume of fluid from inside the droplets, a measured quantity of emulsion is added to a suitable amount of unsaturated chlorobenzene. This is then tumbled gently for several days.

Droplet morphologies were characterized using optical microscopy at a range of magnifications (10x-100x), using either a Leica SP5 confocal microscope operating in bright-field mode or a Nikon Eclipse TE2000-E. Samples were imaged in sealed glass capillaries or sealed imaging chambers made from polyether ether ketone (PEEK) spacers.

8.2 Volume-controlled morphological transitions

We use hydrophilic silica nanoparticles that are coated with a diffuse layer of alkane, rendering them partially hydrophobic and partially hydrophilic. Thus, they are wetted by both dispersed and continuous phases, and the three-phase contact angle characterizing the placement of the nanoparticles at the interface between the two phases is close to 90° . As a

result, once a nanoparticle is mechanically driven to this interface during the emulsification process, it is confined within a potential well of depth as large as hundreds of $k_B T$ [266]. This makes the emulsions used in this work highly stable for at least several weeks.

Due to the strong attachment of the nanoparticles to the droplet surfaces, the average droplet size is controlled by the concentration of nanoparticles used to prepare the samples [267]. The average droplet diameter d is related to the volume concentration c_p of nanoparticles with respect to the dispersed phase by $d = 8\phi_A n a_p / c_p$, where ϕ_A is the fraction of the droplet surfaces that is covered with nanoparticles, n is the average number of nanoparticle layers covering the droplets, and a_p is the nanoparticle radius. This equation fits our data very well over a wide range, as shown in Figure 8.1. Using this fit, we estimate that the droplet surfaces are coated with a monolayer of nanoparticles with surface coverage $\phi_A = 80 \pm 2\%$.

A closed solid shell with a fixed surface area must deform as its volume is reduced and compressive stresses develop in the shell wall. These stresses are typically relieved through buckling events, in which the shell is strongly deformed only at points and lines on its surface [257]. Motivated by this, we develop a technique to study the mechanical properties of our Pickering emulsion droplet surfaces by reducing their average volume in a controlled manner. To achieve volume reduction, we use a dispersed phase whose solubility in the continuous phase is measured to be ~ 0.17 vol%. Thus mixing a Pickering emulsion with unsaturated continuous phase causes a finite amount of the dispersed phase to be pumped out of the droplets until the solubility limit of the continuous phase is reached. We calculate the average decrease in droplet volume ΔV relative to the original droplet volume V_0 to be $\Delta V/V_0 \approx 0.0017V_{add}/\phi V_s$, where ϕ is the emulsion volume fraction, V_s is the

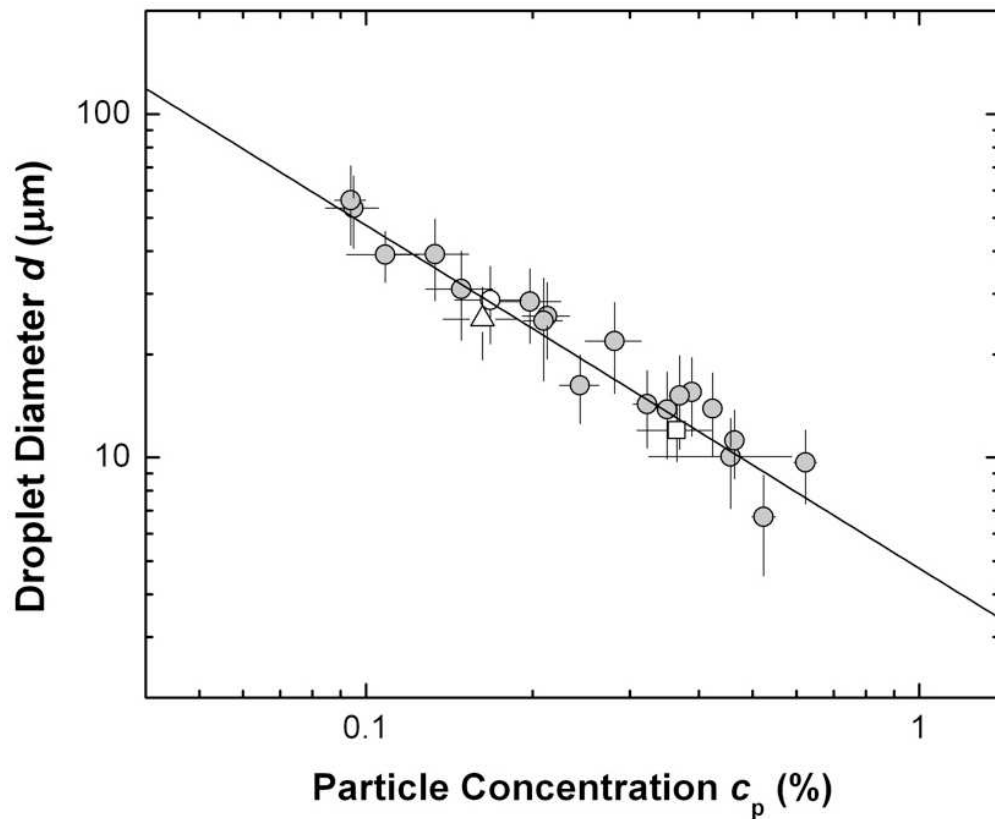


Figure 8.1: **Average droplet diameter d of Pickering emulsion prepared at different nanoparticle concentrations c_p .** White square represents a sample made by adding nanoparticles to the sample represented by the white circle; white triangle represents a sample made by adding more dispersed phase to the sample represented by the white square. Vertical error bars indicate standard deviation of area-weighted size distribution, while horizontal error bars indicate estimated uncertainty in c_p . Solid line indicates inverse dependence of d with c_p ($d = 8\phi_A n a_p / c_p$) as discussed in the text.

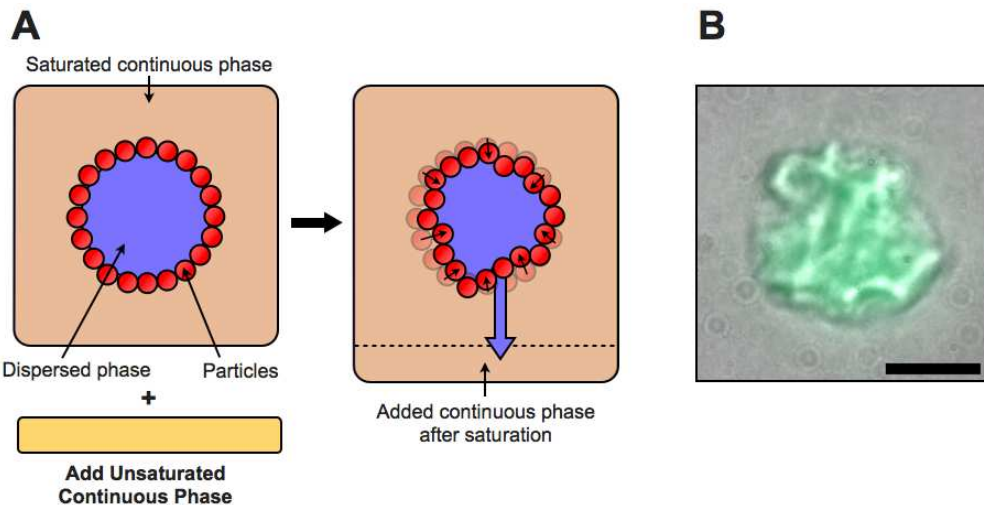


Figure 8.2: Forcing droplets to buckle by shrinking them. (A) Schematic illustrating the controlled reduction of droplet volume of Pickering emulsion droplets. (B) Optical micrograph of a crumpled droplet with fluorescently labeled dispersed phase (green overlaid); scale bar is $5\mu\text{m}$.

initial sample volume, and V_{add} is the volume of additional unsaturated continuous phase. For each value of V_{add} , we use optical microscopy to quantify the fraction of droplets that were clearly buckled or crumpled, analyzing a total of 3759 droplets. The pumping process presented here is analogous to applying a pressure difference across the particle-coated droplet surface. Similar to studies of osmotically-induced buckling of hollow capsules [262], our technique involves the addition of a chemical species that forces solvent to be expelled from the droplet interiors. A key advantage of this approach is that it enables the simultaneous investigation of the buckling of large numbers of Pickering emulsion droplets of varying sizes, yielding statistics of this process unlike approaches using pendant drop tensiometry [268] or a syringe [264] to shrink individual macroscopic droplets.

To study the mechanical nature of the particle-coated droplet surfaces, we observe their morphologies as their volume is reduced. Strikingly, a considerable fraction of the droplets

become non-spherical due to buckling or crumpling (Figure 8.2), unambiguously demonstrating that their surfaces are solid. As V_{add} and hence the degree of pumping is increased, more droplets are deformed. To further understand the properties of the droplet surfaces, we explicitly consider the microscopic interactions between the nanoparticles.

The van der Waals interaction can be estimated by $U_{vdW} = Aa_p/12l$, where A is the Hamaker constant, a_p is the nanoparticle radius, and l is the distance between the nanoparticle surfaces. Using typical values of $A \approx 10 - 20$ J and $l \approx 0.5$ nm, we estimate $U_{vdW} \approx 3k_B T$ and hence, the two-dimensional shear modulus $G'_{2D} \approx U_{vdW}/a_p^2 \approx 0.2$ mN m⁻¹.

In the bulk continuous phase, the nanoparticles possess very weak attractions, whereas in the bulk dispersed phase the nanoparticles are much more strongly attractive due to the interpenetration of the alkyl chains coating the colloidal particles. The maximum value of these attractive interactions can be estimated by $U_{attr} \approx \pi a_p L^2 |1/2 - \chi|/v_m$ where L is the thickness of the surface coating layer, χ is the Flory-Huggins interaction parameter appropriate for the dispersed phase, and v_m is the volume of a solvent molecule [269]. Using suitable values of $L \approx 0.5$ nm, $\chi \leq 10$, and $v_m \approx 3$ Å³, we estimate a maximum value of $U_{att} \approx 10^4 k_B T$; thus, $G'_{2D} \approx U_{att}/a_p^2 \approx 700$ mN m⁻¹.

By modeling a particle monolayer at a fluid interface interacting via capillary forces [270] as an isotropic solid, Vella *et al.* [249] and Arditty *et al.* [251] independently developed an estimate for its Youngs modulus: $E \sim 5\gamma/a_p$, where γ is the fluid-fluid interfacial tension and a_p is the particle radius. Using the interfacial tension for our system measured using pendant drop tensiometry ($\gamma \approx 7$ mN m⁻¹), we use the expression for E to estimate the energy of capillary interactions as $U_{cap} \approx E a_p^3 = 5\gamma a_p^2 \approx 500 k_B T$ and hence

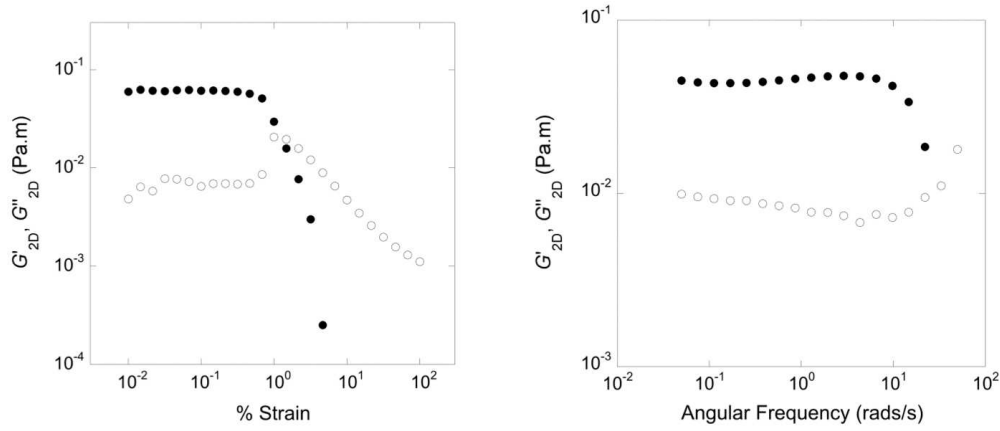


Figure 8.3: Rheology of the particle interface. Interfacial shear and loss moduli G'_2D (closed circles) and G''_2D (open circles) as a function of applied strain at a fixed angular frequency of 5 rads s^{-1} (left image) and as a function of angular frequency at a fixed strain of 0.1% (right image).

the two-dimensional shear modulus $G'_2D \approx U_{cap}/a_p^2 \approx 40 \text{ mN m}^{-1}$.

These simple estimates suggest that the surface shear modulus at the droplet interfaces is likely to be determined predominantly by interparticle attractions due to their surface functionalization and capillary interactions, and is in the range $G'_2D \approx 40 - 700 \text{ mN m}^{-1}$.

We also use interfacial rheology to directly measure G'_2D for the flat fluid-fluid interface saturated with an excess of nanoparticles. We place an excess amount of nanoparticles at a flat interface between ethylene glycol and chlorobenzene and use an Anton-Paar Physica MCR501 rheometer equipped with an Interfacial Rheology System. We use a bicone geometry to directly measure the interfacial elastic and loss moduli G'_2D and G''_2D as a function of applied strain and frequency. The results, shown in Figure 8.3, indicate that the layer of nanoparticles has mechanical properties similar to a soft glassy material [256] with $G'_2D \approx 0.05 \text{ Pa m} = 50 \text{ mN m}^{-1}$.

Furthermore, because our nanoparticles are highly polydisperse, their structure at a

droplet surface is likely to be amorphous, in contrast to systems with monodisperse particles in which crystalline defects play a significant role [271, 272]. Thus, the droplet surfaces can be thought of as thin, porous, solid granular shells. The approach presented here is a powerful means to study volume-controlled morphological transitions of fluid-filled granular shells in a well-defined manner, by subjecting large numbers of droplets to the same degree of pumping.

8.3 Size-dependent morphologies

Unlike the case of a sheet, deforming a thin elastic shell requires it to both bend and stretch [273]; thus, the buckling and crumpling behavior of such shells is typically understood by considering the energies associated with both of these deformation modes. Because stretching deformations require more energy than bending [274], they tend to be focused at points and lines, leading to localized mechanical instabilities that develop as the shell is increasingly deformed. While the mechanical properties of densely packed particles at fluid-fluid interfaces is typically interpreted within the framework of continuum elasticity [248, 249], it is still not clear that this approach is appropriate for particle-coated droplets [275, 276]. To explore the similarities between classical thin elastic shells and our particle-coated droplets, we study the size dependence of droplet buckling as well as the morphologies of buckled and crumpled droplets.

By considering the shell size dependence of the energy required to form a depression in an elastic spherical shell, an analysis based on classical elasticity theory predicts that larger droplets should buckle more easily than smaller droplets [258]. To test this, we prepare samples consisting of droplets of three different average sizes, and controllably reduce

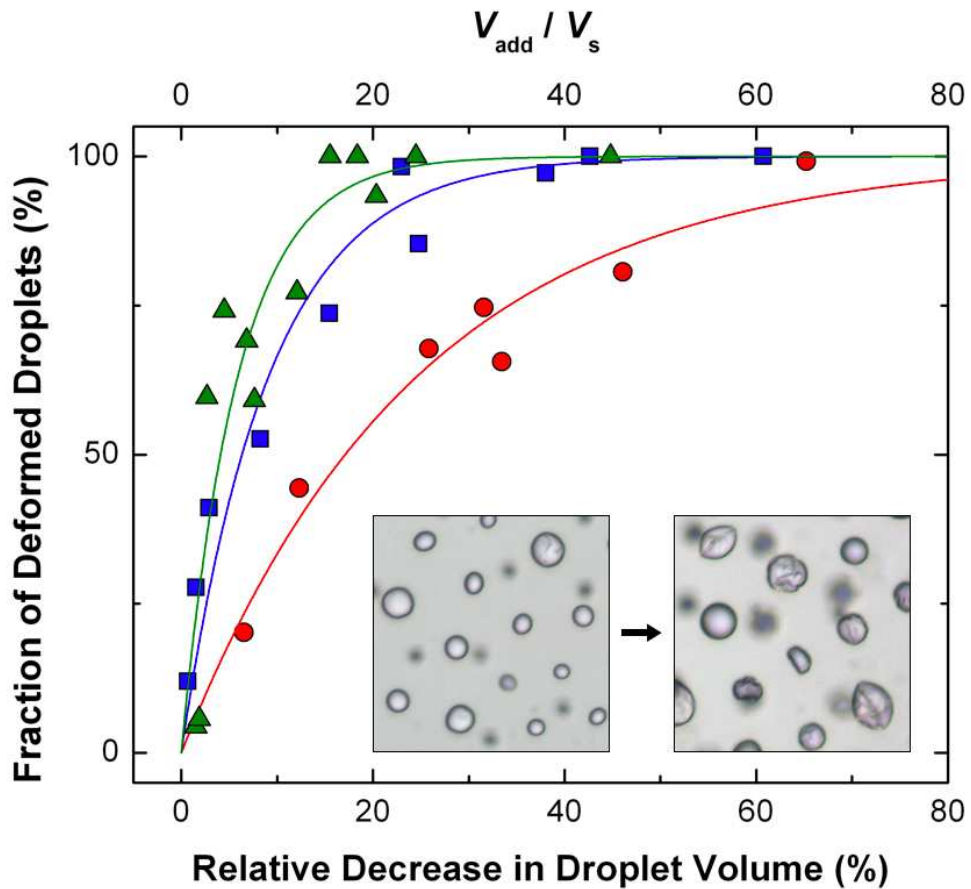


Figure 8.4: **Volume change controls amount of buckling.** A plot of the fraction of buckled/crumpled droplets as a function of calculated relative change in droplet volume for samples of average droplet diameters $d = 14.7\mu\text{m}$ (red circles), $34.7\mu\text{m}$ (blue squares), and $44.1\mu\text{m}$ (green triangles). Solid lines are guides to the eye. Inset shows optical micrographs of two different samples: left has undergone weak pumping, right has undergone stronger pumping.

their average volume. Crucially, our data clearly show that larger droplets require a smaller relative decrease in their volume than do smaller droplets to crumple by the same fraction, as shown in Figure 8.4. This suggests that larger droplets crumple more easily, which is in agreement with the idea of having a thin shell of densely-packed colloids covering the fluid droplets.

Our approach is a useful way to characterize the morphological transitions undergone by droplets at varying degrees of pumping. For weak pumping, the droplets are often non-spherical, forming polyhedra with multiple flat facets separated by straight edges (Figure 8.5A). Similar shapes have been achieved previously for particle-coated bubbles or droplets that have coalesced or that have forcibly undergone plastic deformation [277]. In our system, however, it is likely that such shapes arise from the presence of localized defects in the granular shell. These can mediate the structural transitions of the shell due to volume pumping in a manner similar to that in which fivefold disclinations can lead to faceting of crystalline granular shells [278]. For intermediate pumping, droplets develop dimples or corrugations of size $\sim 1 - 10\mu\text{m}$ on their surfaces (Figure 8.5B). These are reminiscent of post-buckling structures for thin shells under pressure [279] or core-shell structures whose shells have experienced significant compressive stresses [262, 259]. As pumping increases, droplets have more crumpled morphologies with increasing numbers of dimples developing; this is consistent with the notion that crumpling may be thought of as a sequential buckling process [257]. For stronger pumping, dimples grow into cusps and ridges spanning a wide range of size scales ($\sim 0.1 - 100\mu\text{m}$) joining points of maximal curvature (Figure 8.5C). Due to the fixed surface area of the shell, these cusps and ridges start to interact with each other as fluid is pumped out of the droplets, as demonstrated

by the increasing numbers of longer and sharper cusps and ridges shown in Figure 8.5C. This suggests that in-plane stretching of the nanoparticle network at the droplet surface is energetically more costly than bending, as in the case of thin continuum sheets, and stress is localized heterogeneously on the droplet surface.

These observations strongly support the hypothesis that a sufficiently densely packed layer of colloidal particles at a fluid-fluid interface acts like a solid. In particular, the nonuniform capillary stresses associated with the highly deformed morphologies adopted by our droplets must be supported by localized stresses in the solid granular shell; otherwise, these would be pulled back to a spherical shape by the fluid-fluid interfacial tension [277, 250, 280, 281]. Moreover, all observed morphologies are “frozen-in”; they are stable over an observation time of hours. Furthermore, when subjected to a shear flow, buckled droplets undergo rigid-body rotation as expected for a solid shell. This is clearly different from the tank treading motion expected for a droplet with a fluid surface [282], confirming that the particles form a solid layer at the droplet interfaces.

In addition to the typical morphologies shown in Figure 8.5A-C, droplets exhibit a number of other buckled structures. These include multifaceted polyhedral indentations consisting of up to eight vertices (Figures 8.5D and 8.6); sharply-defined creases and ridges that meet at individual points (Figure 8.5E); and elongated shapes strongly reminiscent of folded monosulcate lily pollen grains [285] (Figure 8.5F). The observation of such a variety of buckled structures suggests that the mechanical properties of the interfaces of the Pickering droplets are non-uniform. The morphologies observed are strikingly similar to those seen for thin continuum elastic shells possessing locally more compliant areas on their surface. For example, a spherical cap with a single point-like “weak spot” develops a faceted

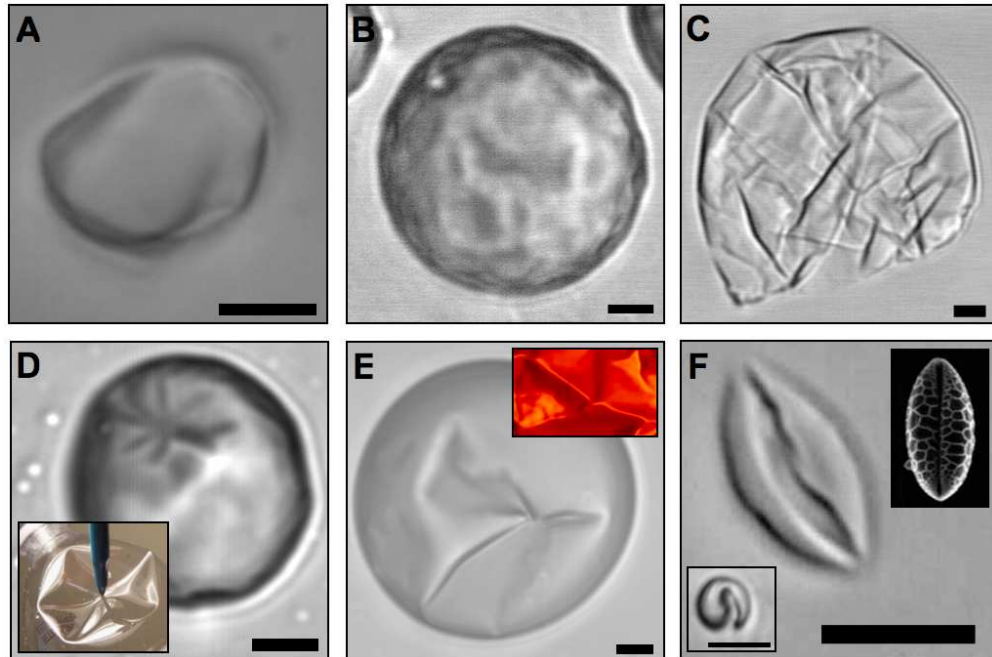


Figure 8.5: Optical micrographs of different buckled droplets. (A-C) show characteristic shapes at increasing levels of pumping, ranging from weak pumping (A), intermediate pumping (B), and strong pumping (C). Typical buckled structures also include multifaceted polyhedral indentations (D), stretching ridges, *d*-cones, and “swallowtail” folds (E), and elongated “football” structures (F). Bottom-left inset to (F) shows representative end-on view. All scale bars are $5\mu\text{m}$. Colored insets show macroscopic analogues of buckled structures: point indentation of a bottle using a pen [283] (D), creases and ridges in crumpled paper [284] (E), and elongated dessicated pollen granule [285] (F).

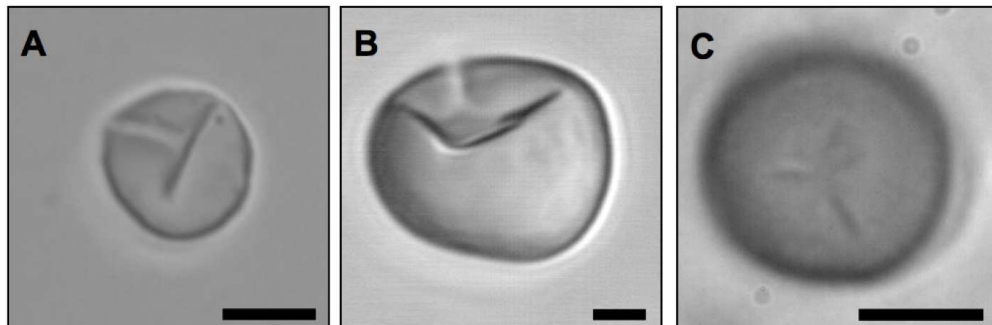


Figure 8.6: Optical micrographs of different buckled droplets. We observe multifaceted polyhedral indentations having three (A), four (B), and six (C) vertices. All scale bars are $5\mu\text{m}$.

polyhedral indentation within its surface upon volume reduction, similar to the structure shown in Figure 8.5D [283, 285]. In folded sheets and large crumpled shells, multiple point-like singularities connected by stretching ridges give rise to morphologies similar to that shown in Figure 8.5E [257, 286, 287, 284]. A “weak spot” extended along a line on the surface of a shell, such as at a grain boundary [271], gives rise to an elongated structure upon volume reduction as in the droplet shown in Figure 8.5F [285]. These comparisons suggest that the observed non-uniform crumpling morphologies can be attributed to heterogeneities in the colloidal shell of the Pickering droplets that inevitably arise during sample preparation. The compliant areas in the surfaces of Pickering emulsions likely guide the development of deformations during volume reduction, giving rise to the rich diversity of post-buckling morphologies. Thus, by tuning the arrangements of particles at the droplet interfaces, the crumpling morphologies can potentially be controlled.

In conclusion, we present a straightforward and general method for buckling and crumpling statistically significant numbers of nanoparticle-coated droplets by pumping fluid out of the droplet interiors. Increasing numbers of droplets buckle and crumple as their average volume is reduced. The extent to which droplets are buckled or crumpled depends on the average droplet size, with larger droplets crumpling more easily than smaller droplets in agreement with ideas based on continuum elasticity theory. As they undergo volume reduction, droplets become increasingly non-spherical and develop progressively more dimples, suggesting that crumpling may be thought of as a sequential buckling process. For stronger pumping, cusps and sharply curved ridges develop and grow. The structures of our buckled Pickering emulsions are strikingly similar to the buckled shapes of thin continuum elastic shells. Our approach is a new means to realize stable non-spherical fluid droplets, and our

observations show that the droplet surfaces are solid-like. The technique presented here offers a route to systematically study the morphological transitions of thin fluid-filled granular shells undergoing volume reduction and to explore the similarities between these and “classical” thin elastic shells.

Chapter 9

Buckling of inhomogeneous microcapsules

An important stimulus for microcapsule release is an externally imposed stress. This idea is central to one of the earliest and most ubiquitous applications of microcapsules: to encapsulate and release the colorless ink used in carbonless copy paper. The microcapsules coat each sheet of paper, only releasing the encapsulated ink when pressed on sufficiently hard by a pen; the released ink then reacts with a developer coating the underlying sheet, forming a mark that reproduces the pen's trace [81]. In this application, as in numerous others, the utility of the microcapsules depends sensitively on the mechanical properties of their shells.

One common way of characterizing this behavior is to monitor how a microcapsule responds to an externally-imposed pressure. For small pressures, a homogeneous, spherical shell, characterized by a uniform thickness, supports a compressive stress, and it shrinks isotropically. Above a threshold pressure, however, this shrinkage becomes energetically

prohibitive; instead, the shell buckles, reducing its volume by forming a localized indentation at a random position on its surface. For the case of a homogeneous shell, this threshold pressure can be calculated using a linearized analysis of shell theory [279, 288], while the exact morphology of the shell after it buckles requires a full nonlinear analysis [289, 290, 283]. However, many microcapsule shells are inhomogeneous, characterized by spatially-varying thicknesses and elastic constants. Such inhomogeneities can strongly influence how a shell buckles [285, 279, 291, 292, 293, 294, 295]. Unfortunately, despite its common occurrence in real microcapsules, exactly how inhomogeneity influences the onset of buckling, as well as the microcapsule morphology after buckling, remains to be elucidated. A deeper understanding requires careful investigations of the buckling of spherical microcapsules with shells having tunable, well-defined, inhomogeneities.

In this Chapter⁸, we use a combination of experiments, theory, and simulation to study the buckling of spherical microcapsules with inhomogeneous shells of non-uniform thicknesses. We show that the onset of buckling, above a threshold external osmotic pressure, is well described by shell theory; however, even above this threshold, the microcapsules do not buckle immediately. We find that the time delay before the onset of buckling decreases as the shells are made more inhomogeneous; these dynamics can be quantitatively understood by coupling shell theory with Darcy's law for flow through a porous microcapsule shell, even for highly inhomogeneous shells. Moreover, we find that the shell inhomogeneity guides the folding pathway taken by a microcapsule during and after buckling. We use

⁸Based on "Delayed buckling and guided folding of inhomogeneous capsules", S. S. Datta*, S-H Kim*, J. Paulose*, A. Abbaspourrad, D. R. Nelson, and D. A. Weitz, *Physical Review Letters* 109, 134302 (2012) and "Controlling release from double emulsion-templated microcapsules", S. S. Datta*, A. Abbaspourrad*, E. Amstad, J. Fan, S-H Kim, M. Romanowsky, H. C. Shum, B. J. Sun, A. S. Utada, M. Windbergs, S. Zhu, and D. A. Weitz, to be submitted (2013) *Equal contribution.

these insights to controllably create novel colloidal structures using buckling.

9.1 Microcapsule fabrication

Microcapsules can be fabricated using a variety of techniques, including spray drying [296, 297, 298], electrospraying [299, 300, 301], coextrusion [302, 303, 304], interfacial polymerization [305, 306, 307], polymer phase separation [308, 309], layer-by-layer deposition [74, 310, 311], or membrane emulsification [312, 313]. However, the highly variable shear typically used in these approaches yields microcapsules with polydisperse sizes and structures, and consequently, poorly controlled loading levels and release kinetics – even within the same batch. This can severely limit the use of microcapsules in many practical applications. Microfluidic technologies offer exquisite control over the flows of multiple fluids, and thus, a way to overcome these limitations. One particularly promising route is the use of microfluidics to produce double emulsions, drops of the core material within drops of another fluid, which are themselves suspended in a continuous fluid phase. The middle phase can then be solidified, yielding microcapsules. The interfacial tensions between the different fluids forces the drops to be spherical; moreover, the drop sizes are determined by the shear forces exerted on the flowing fluids, which can be carefully tuned in a microfluidic device. As a result, double emulsion drops generated in microfluidics, and the microcapsules made from them, can be highly monodisperse, with compositions and morphologies that can be manipulated with a remarkable degree of accuracy.

We fabricate monodisperse thin-shelled microcapsules using water-in-oil-in-water (W/O/W) droplets prepared with two different types of glass capillary microfluidic devices. To make microcapsules with $h_0/R_0 = 0.017$, we use a device composed of a hydrophobic

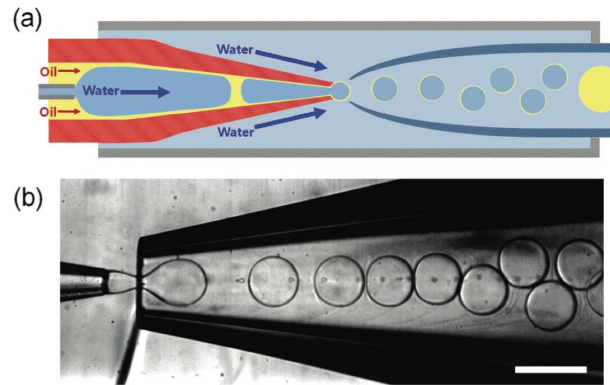


Figure 9.1: **Microfluidic production of double emulsion drops with $h_0/R_0 = 0.017$.**
Scale bar is $200\mu\text{m}$.

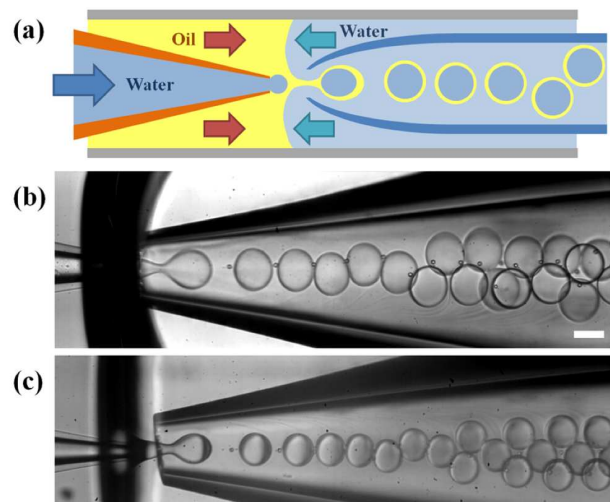


Figure 9.2: **Microfluidic production of double emulsion drops with (b) $h_0/R_0 = 0.019$ and (c) $h_0/R_0 = 0.1$.** Scale bars are $100\mu\text{m}$.

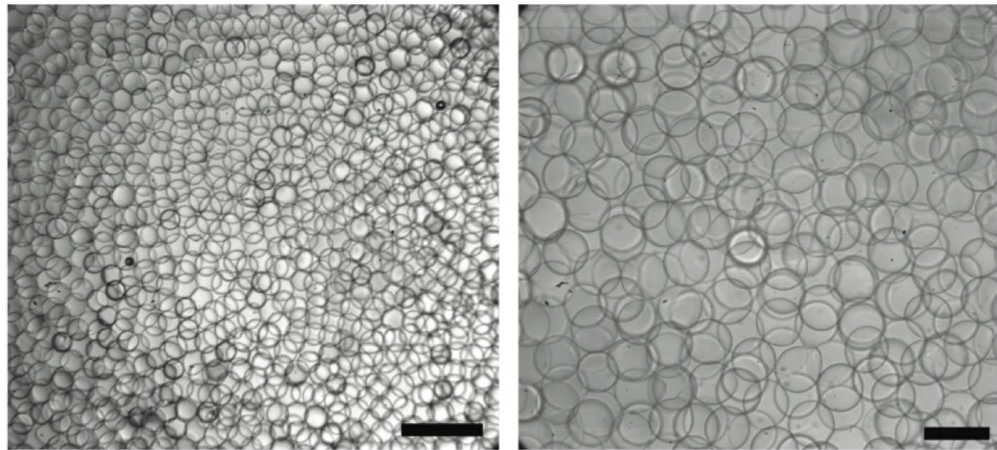


Figure 9.3: Monodisperse microcapsules. Scale bars in (a) and (b) are $500 \mu\text{m}$ and $200 \mu\text{m}$, respectively.

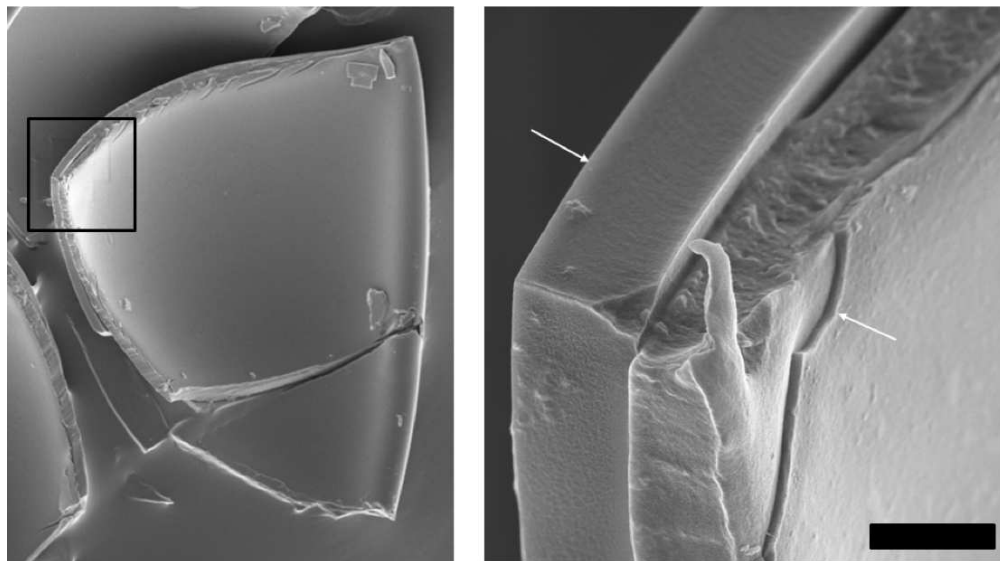


Figure 9.4: SEM showing inhomogeneous microcapsule shell. Shells buckle at the thinnest part; as a result, the thinnest part contacts the thickest part of the shell. Right panel: the left arrow shows the thinnest part of the shell, and the right arrow shows the thickest part of the shell; the solid in between the two parts of the shell is precipitated PVA. Scale bar is $2 \mu\text{m}$.

tapered injection capillary (World Precision Instruments, Inc., 1B100-6), pre-treated with n-octadecyltrimethoxyl silane (Aldrich), inserted in a second square capillary (AIT glass); the inner diameter of the square capillary and the outer diameter of the injection capillary are both 1 mm. Furthermore, a small tapered capillary is inserted into the injection capillary to simultaneously inject two immiscible fluids, as shown in Figure 9.1. To confine the flow near the injection tip and thereby increase the flow velocity, a hydrophilic circular capillary, pre-treated with 2-[methoxy(polyethyleneoxy)propyl] trimethoxyl silane (Gelest, Inc.), is inserted into the square capillary at its other end.

To make W/O/W double emulsion droplets, we simultaneously introduce two immiscible phases, 10 wt% aqueous solution of poly (vinylalcohol) (PVA, Mw 13000-23000) and ethoxylated trimethylolpropane triacrylate (ETPTA) containing 0.2 wt% photoinitiator (2-hydroxy-2-methylpropiophenone, Aldrich), through the injection capillary at flow rates of $300 \mu\text{L h}^{-1}$ and $150 \mu\text{L h}^{-1}$, respectively. The aqueous solution is saturated with ETPTA before injection to prevent diffusion of ETPTA molecules through water. We use the same aqueous solution of PVA as the continuous phase; this is injected through the square capillary at the flow rate of $3000 \mu\text{L h}^{-1}$. Because of the hydrophobic nature of the injection capillary, the ETPTA flows along the inner surface of the injection capillary; by contrast, the aqueous solution flows through the center of the injection capillary as plug-like droplets that do not contact the wall. These plug-like droplets are emulsified at the tip of the injection capillary, resulting in monodisperse double emulsion droplets with an ultra-thin middle layer as shown in Figure 9.1(b). The ETPTA formed between plug-like droplets produces large blobs at the tip of the injection capillary; we separate these from the double emulsion droplets by exploiting their density difference. We prepare thin-shelled microcapsules by

photo-polymerization of the droplet middle phase, ETPTA.

To make microcapsules with $h_0/R_0 = 0.019$ and 0.1 , we use a device composed of hydrophobic injection and collection capillaries as shown in Figure 9.2(a). The innermost aqueous phase is injected through the injection capillary and the middle ETPTA phase is injected through the interstices of the injection and the square capillaries. The continuous aqueous phase is injected through the interstices of the collection and the square capillaries as a counter flow to the innermost and the middle phases. These three streams flow coaxially through the orifice of the collection capillary, making double emulsion drops in a dripping mode. For $h_0/R_0 = 0.019$, flow rates of the innermost, the middle, and the continuous phases are kept at $400, 80, 2000 \mu\text{L h}^{-1}$, respectively, as shown in Figure 9.2(b). For $h_0/R_0 = 0.1$, flow rates of the innermost, the middle, and the continuous phases are kept at $200, 100, 2000 \mu\text{L h}^{-1}$, respectively, as shown in Figure 9.2(c). Optical microscope images of monodisperse microcapsules with $t_w = 1 \text{ min}$ are shown in Figure 9.3.

To make microcapsules with two or three spherical compartments, we employ two-step emulsification in a capillary microfluidic device. Inner water drops are produced at the tip of small tapered capillary in a dripping mode, which in turn are encapsulated into oil drops at the tip of injection capillary. Through precise control of flow rates of three streams, we can manipulate generation frequency of inner water drops and outer oil drops. Therefore, the number of inner drops confined in outer drop is controllable. To make the thin shell, the flow rate of middle oil stream is maintained to be small enough to encapsulate two or three inner drops with nonspherical envelope. The nonspherical double emulsion drops are polymerized by *in-situ* UV irradiation, resulting in microcapsules with multiple spherical compartments.

The PVA solution is less dense than the oil; as a result, after the droplets are produced and collected, the light inner water droplets gradually rise within them. This causes the oil to gradually thin on the top side of each droplet and thicken on the bottom [314]. We exploit this effect to prepare microcapsules, with outer radius R_0 , and spatially-varying shell thickness $h(\theta) \approx h_0 - \delta \cos\theta$; θ is measured from the top of the gravitationally-oriented shell, h_0 is the average shell thickness, and δ is the total distance moved by the inner droplet, as shown schematically in Figure 9.5(a). The shell inhomogeneity can thus be quantified by the ratio δ/h_0 . We use UV light to polymerize the oil either as the microcapsules are produced *in situ*, or after different average waiting times, t_w ; this enables us to prepare separate batches of microcapsules characterized by varying degrees of shell inhomogeneity. We use either scanning electron microscopy (SEM) or confocal microscopy to directly measure the microcapsule geometrical characteristics.

Microcapsules photopolymerized *in situ* are prepared in the following manner: As soon as the drops flow out from the nozzle of a microfluidic device to water bath containing 8 wt% aqueous solution of PVA which is saturated with ETPTA, they are polymerized by continuous UV irradiation (Omnicure S1000).

Microcapsules with $t_w = 5$ s or 1 min are prepared in the following manner: As they are continuously produced from the nozzle of the microfluidic device, the droplets are collected into a chamber containing 8 wt% aqueous solution of PVA saturated with ETPTA and are repetitively irradiated with UV irradiation (Omnicure S1000) of duration 1 second, fully polymerizing the ETPTA into a thin solid shell, every $2 \times t_w$. This forms a population of microcapsules that have remained quiescent in the collection chamber for an average waiting time of t_w before polymerization.

Microcapsules with $t_w = 1$ hr, 1 day, 2 days or 5 days are prepared in the following manner: As they are continuously produced from the nozzle of the microfluidic device, the droplets are collected for a total time of 10 min into a chamber containing 10 wt% aqueous solution of PVA saturated with ETPTA. They are then photopolymerized after a waiting time of $t_w - 5\text{min}$.

Some microcapsules are subsequently washed in de-ionized water after they are collected. The shell is a solid characterized by a Young's modulus $E \approx 600$ MPa [315]; importantly, while this shell is impermeable to Na^+ and Cl^- ions, it is permeable to water [316].

9.2 Onset of microcapsule buckling

To probe their mechanical response, we subject inhomogeneous microcapsules, characterized by $t_w = 1$ min, $\delta/h_0 \approx 0.2$ and $h_0/R_0 = 0.017$, to an external osmotic pressure by injecting and gently mixing $20\mu\text{L}$ of the microcapsule suspension into a fixed volume of NaCl solution, $V_{\text{NaCl}} \approx 130 - 400 \mu\text{L}$. We investigate the pressure dependence of buckling using NaCl concentrations in the range 0.063-2.165 M. Estimating the total volume of the injected microcapsules using optical microscopy allows us to calculate the final NaCl concentration of the outer phase, which then ranges from $c_{\text{NaCl}} = 0.055 - 2.068$ M. These correspond to osmotic pressure differences across the shell of $\Pi = (2c_{\text{NaCl}} + \Pi_{\text{out}} - \Pi_{\text{in}}) \times N_A k_B T = 0.025 - 10.09$ MPa, where N_A is Avogadro's constant, k_B is Boltzmann's constant, $T \approx 300$ K, and Π_{out} and Π_{in} are the measured osmolalities of the fluids outside and inside the microcapsules, respectively, in the absence of NaCl.

For each batch of microcapsules studied, we monitor an average of 75 microcapsules over time using optical microscopy.

The osmotic pressure difference across these inhomogeneous shells forces the microcapsules to buckle; we observe the abrupt formation of localized indentations in the shells, as shown in Figure 9.5(b). For each osmotic pressure investigated, the fraction of the microcapsules that buckle increases over time, eventually plateauing, as shown in Figure 9.5(c). We quantify this behavior by fitting this increase to an empirical exponential relationship, exemplified by the smooth lines in Figure 9.5(c). The plateau value of this function yields a measure of the total fraction of the microcapsules that ultimately buckle over sufficiently long times, while the time constant of this function yields a measure of the time delay before the onset of buckling, τ . For sufficiently large Π , the total fraction of the microcapsules that ultimately buckle increases dramatically with increasing Π , as shown by the grey circles in Figure 9.5(d); this indicates that the microcapsules buckle above a threshold pressure, Π^* . We empirically fit these data using the cumulative distribution function of a normal distribution, shown by the black line in Figure 9.5(d); the mean value and standard deviation of this fit yield a measure of Π^* and the spread in Π^* , respectively.

We study the geometry dependence of Π^* by performing additional measurements on inhomogeneous microcapsules, polymerized *in situ*, with different shell thicknesses and radii; these are characterized by $\delta/h_0 \approx 0.2$, and $h_0/R_0 = 0.019$ or $h_0/R_0 = 0.1$. Similar to the $h_0/R_0 = 0.017$ case, for sufficiently large Π , the total fraction of the microcapsules that ultimately buckle increases dramatically with increasing Π , as shown by the red triangles and blue squares in Figure 9.5(d). Interestingly, we find that the threshold buckling pressure $\Pi^* \sim (h_0/R_0)^2$ [Figure 9.5(d), inset]; this observation is reminiscent of the pre-

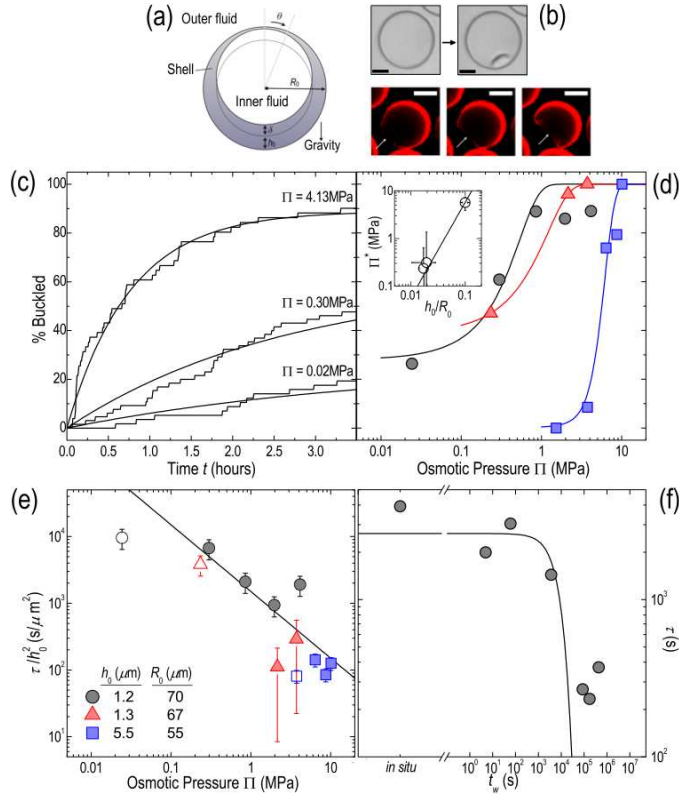


Figure 9.5: Buckling of inhomogeneous microcapsules. (a) Schematic showing the microcapsule geometry investigated. (b) Upper: buckling of a microcapsule; scale bar is $20\mu\text{m}$. Lower: buckling begins at the thinnest part of the shell for microcapsules with thickness inhomogeneity $\delta/h_0 \approx 0.84$; scale bars are $50\mu\text{m}$. (c) Fraction of microcapsules buckled over time, for three different osmotic pressures Π . Capsules have mean shell thickness $h_0 = 1.2\mu\text{m}$, outer radius $R_0 = 70\mu\text{m}$, and $\delta/h_0 = 0.20$. Smooth lines show exponential fits. (d) Total fraction of microcapsules that ultimately buckle over time for varying Π , for capsules with h_0, R_0 , and $\delta/h_0 = 1.2\mu\text{m}, 70\mu\text{m}$, and 0.20 (grey circles), $1.3\mu\text{m}, 67\mu\text{m}$, and 0.23 (red triangles), and $5.5\mu\text{m}, 55\mu\text{m}$, and 0.19 (blue squares). Smooth curves are fits to the data using the cumulative distribution function of the normal distribution. Inset shows mean osmotic pressure of each fit versus h_0/R_0 ; vertical and horizontal error bars show standard deviation of each fit and estimated variation in h_0/R_0 , respectively. Straight line shows $(h_0/R_0)^2$ scaling. (e) Time delay before the onset of buckling, τ , normalized by h_0^2 , for varying Π , for the same microcapsules as in (d). Filled points show $\Pi > \Pi^*$ while open points show $\Pi < \Pi^*$. Vertical error bars show uncertainty arising from estimated variation in h_0 . Black line shows Π^{-1} scaling. (f) Time delay τ decreases with the wait time before a shell is polymerized, t_w ; microcapsules have $h_0 = 1.2\mu\text{m}$ and $R_0 = 70\mu\text{m}$, and are buckled at $\Pi \approx 0.86 \text{ MPa} > \Pi^*$. Black line shows theoretical prediction coupling shell theory and Darcy's law, as described in the text, with $k \approx 3.5 \times 10^{-24} \text{ m}^2$.

dition of shell theory for the buckling of a *uniform* shell [288], despite the fact that our microcapsules are inhomogeneous. To understand this behavior, we consider the local deformability of an inhomogeneous shell at various points on its surface. Because the 2D stretching and bending stiffnesses scale as $\sim h$ and $\sim h^3$ [317], respectively, the thinnest part of the shell, where $h \approx h_0 - \delta$, should be the easiest to deform. We directly visualize that buckling begins at this “weak spot” using confocal microscopy of inhomogeneous microcapsules with fluorescent shells characterized by $\delta/h_0 \approx 0.84$ [Figure 9.5(b), lower panel]. Consequently, we expect the onset of buckling to be governed by deformations in this part of the shell. To quantify this expectation, we apply shell theory to an inhomogeneous shell characterized by the same geometry as the experimental microcapsules [5]; this analysis yields $\Pi^* = \frac{2E}{\sqrt{3(1-\nu^2)}} \left(\frac{h_0-\delta}{R_0}\right)^2 \approx 470(h_0/R_0)^2$ MPa, assuming a Poisson ratio $\nu \approx 1/3$. The dependence of Π^* on $h_0 - \delta$ confirms our expectation that the threshold buckling pressure is set by the thinnest part of the inhomogeneous shell. Moreover, we find $\Pi^*(R_0/h_0)^2 \approx 600 \pm 200$ MPa for the experimental microcapsules [solid line, Figure 9.5(d) inset], in good agreement with our theoretical prediction. This indicates that the onset of microcapsule buckling is well described by shell theory.

9.3 Dynamics of microcapsule buckling

Within this framework, for $\Pi > \Pi^*$, a microcapsule remains spherical before it buckles; it initially responds to the applied pressure by contracting uniformly, reducing its volume from its initial value, V_0 , by a threshold amount ΔV^* , before buckling. We find that the time delay before the onset of buckling, τ , strongly decreases with increasing osmotic pressure $\Pi > \Pi^*$, as shown by the filled points in Figure 9.5(e). We hypothesize that this

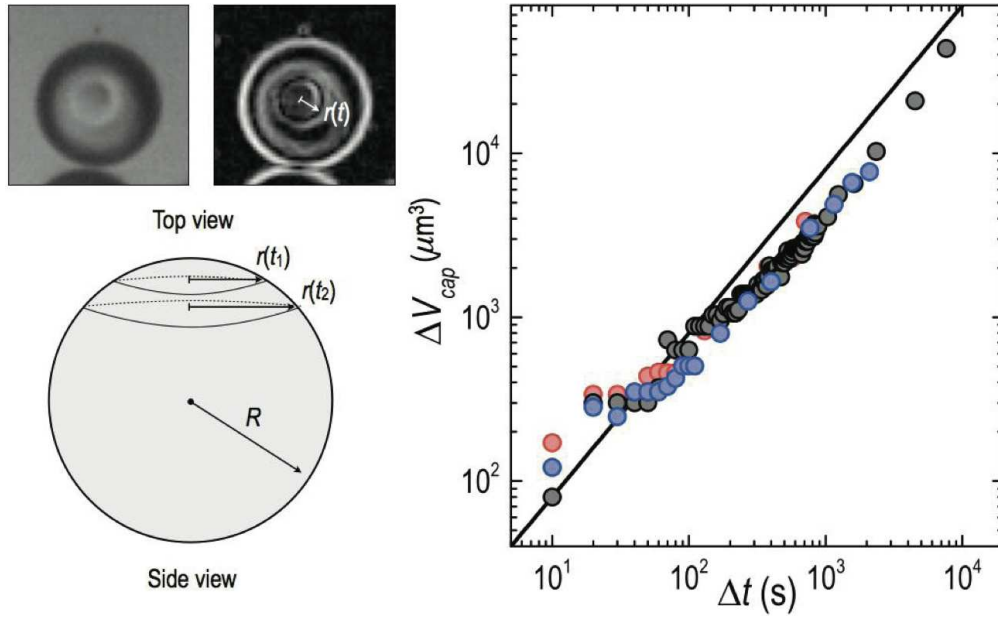


Figure 9.6: Measuring microcapsule permeability. Change in the volume of a circular indentation formed in a microcapsule, ΔV_{cap} , over time Δt . The indentation forms at $\Delta t = 0$. Top left panel shows the top view of the indentation formation, measured using optical microscopy; we use image processing to detect the edge of the indentation, shown in the panel to the right, and track the radius of the indentation over time, $r(t)$. We assume a spherical cap geometry, schematically shown in the side view, to calculate ΔV_{cap} ; the data are shown for three different capsules (different colors). We fit the small-time dynamics ($\Delta t < 10^2$ s) to measure the permeability. The microcapsules have $h_0/R_0 = 0.1$ and $\delta/h_0 \approx 0.2$, and are buckled at $\Pi = 10$ MPa.

behavior reflects the dynamics of the fluid flow through the microcapsule shell; for the microcapsule to buckle, a volume ΔV^* of fluid must be ejected from its interior. The time delay can then be estimated as $\tau = \Delta V^*/Q$, where both ΔV^* and Q , the volumetric rate of fluid ejection from the microcapsule interior, are functions of δ/h_0 . We calculate ΔV^* for inhomogeneous shells using shell theory and validate the calculations with numerical simulations [5]; the fluid ejection rate Q follows from integrating Darcy's law over the surface of the microcapsule geometry shown in Figure 9.5(a).

The buckling of a microcapsule is driven by the fluid ejection from the microcapsule

interior, due to the imposed osmotic pressure difference across the microcapsule shell, Π . This is resisted by the mechanical pressure required to compress the shell, Π_m , at most $\Pi_m \approx 2E(1-\nu)^{-1}h_0(1/R^* - 1/R_0) \approx 3E(h_0/R_0)[(1 - \Delta V^*/V_0)^{-1/3} - 1]$, where R^* is the radius of the shell at buckling. For the shells studied in this work, $\Pi_m < \Pi^*$; we thus expect the buckling dynamics to be dominated by the imposed osmotic pressure for $\Pi \gg \Pi^*$, and we neglect Π_m in the simple model presented here.

We now estimate the flow rate out of an inhomogeneous microcapsule due to Π ; the microcapsule has shell thickness $h(\theta) = h_0 - \delta \cos\theta$. We use spherical coordinates (r, θ, ϕ) centered on the microcapsule center. For an arbitrary area element dA on the shell surface at (R_0, θ, ϕ) , the local volumetric ejection rate is given by Darcy's law, $dA \cdot \Pi k / \mu h(\theta)$, where k is the shell permeability and μ is the fluid viscosity. Integrating this over the entire shell surface yields the total ejection rate through the shell:

$$Q = R_0^2 \int_0^{2\pi} d\phi \int_0^\pi \sin\theta \frac{\Pi k}{\mu(h_0 - \delta \cos\theta)} d\theta = \frac{4\pi R_0^2 \Pi k}{\mu h_0} \cdot \frac{1}{2\delta/h_0} \ln \left(\frac{1 + \delta/h_0}{1 - \delta/h_0} \right) \quad (9.1)$$

The time delay before the onset of buckling, τ , is the time taken for the volume of fluid ejected from the shell to equate to the threshold buckling volume, $\tau = \Delta V^*/Q$. Combining the calculated ΔV^* [5] with the expression for Q yields

$$\tau \approx \frac{V_0}{Q_0} \sqrt{\frac{3(1-\nu)}{1+\nu}} \frac{h_0}{R_0} \left(1 - \frac{\delta}{h_0} \right)^2 \quad (9.2)$$

where $Q_0 \equiv 4\pi R_0^2 \Pi k / \mu h_0$ and k is the shell permeability. For the inhomogeneous microcapsules, characterized by $\delta/h_0 \approx 0.2$, we thus expect $\tau/h_0^2 \approx 0.8\mu/k\Pi$; our experimental measurements of τ allow a direct test of this prediction. Above Π^* , the data collapse when τ is rescaled by h_0^2 , as shown by the filled points in Figure 9.5(e), consistent with our expec-

tation; moreover, by fitting these data [black line in Figure 9.5(e)], we obtain an estimate for the shell permeability, $k \approx 7 \times 10^{-24} \text{ m}^2$.

We use optical microscopy to directly measure the rate at which the microcapsule volume decreases immediately after the onset of buckling; this gives an independent measure of the shell permeability. We estimate the microcapsule permeability k by measuring the change in the radius of a circular indentation r over time, immediately after it is formed in the shell, as shown in Figure 9.6. We assume the volume of the indentation ΔV_{cap} is given by that of a spherical cap having radius $r(t)$. The permeability is then given by $k \approx \frac{\mu h_0 d(\Delta V_{cap})/d(\Delta t)}{\Pi \cdot 4\pi R_0^2}$. In reality, the edges of the indentation are rounded, with radius of curvature $\sim \sqrt{h_0 R_0} \sim 15 \mu\text{m}$ [317]; we thus expect our estimated ΔV_{cap} to overpredict the actual ΔV , and consequently, we expect to underpredict the shell permeability by a factor ~ 2 . We find $k \approx 2 \times 10^{-24} \text{ m}^2$ [Figure 9.6], in good agreement with the fit shown in Figure 9.5(e); this further confirms the validity of Equation 9.2.

To test the applicability of this picture to even more inhomogeneous microcapsules, we measure τ for microcapsules polymerized at different t_w ; these have shells with $h_0/R_0 = 0.017$ and δ/h_0 ranging from 0.2 up to 0.84. We impose a fixed osmotic pressure $\Pi \approx 0.86 \text{ MPa} > \Pi^*$. We observe that τ decreases only slightly with increasing $t_w < 10^3 \text{ s}$; however, as t_w is increased above this value, τ drops precipitously over one order of magnitude, as shown by the points in Figure 9.5(f). To quantitatively compare these data to Equation 9.2, we estimate the dependence of δ/h_0 on t_w using lubrication theory, applied to the double emulsion geometry shown in Figure 9.5(a) [318].

Before UV polymerization at time t_w , the inner droplet containing 10 wt% PVA has radius $R_0 - h_0$ and the outer droplet containing ETPTA monomer has radius R_0 ; the shell

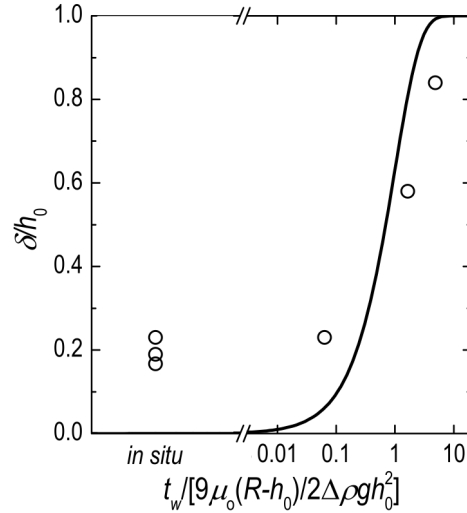


Figure 9.7: **Total fraction of microcapsules that ultimately buckle increases with wait time before polymerization t_w , and hence the shell inhomogeneity.** Microcapsules have $h_0 = 1.2 \mu\text{m}$ and $R_0 = 70 \mu\text{m}$, and are buckled at $\Pi \approx 0.86 \text{ MPa} > \Pi^*$.

thickness is then $h(t_w) = h_0 - \delta(t_w)\cos\theta$. The droplets are collected in 8 wt% or 10 wt% PVA solution. We note that, for our shells, $h_0/R_0 \leq 0.1$. Moreover, using our experimental measurements of $\delta(t_w)$, we estimate the characteristic translation speed of the inner droplet as $\sim 1 \mu\text{m day}^{-1}$; using a characteristic droplet length scale $< 100 \mu\text{m}$, shell viscosity $\mu_0 = 65 \text{ mPa s}$, fluid-fluid surface tension $\sim 2.5 \text{ mN m}^{-1}$, this corresponds to a Reynolds number $Re < 10^{-10}$ and a capillary number $Ca < 10^{-10}$. The fluid-fluid interface can thus be approximated as spherical, and the flow in the shell between the inner and outer droplets is well described using lubrication theory. We denote $x = r\theta$ as the direction along the shell, where r is the spherical radial distance measured from the center of the inner sphere, and z is across the shell.

Because both inner and outer droplets are stabilized by 8-10 wt% PVA, Marangoni stresses resist shear stresses at the fluid interfaces; thus, we assume no-slip boundary con-

ditions on the fluid-fluid interfaces at $z = 0$ and $z = h(\theta, t_w)$. The Stokes equation then yields the velocity distribution:

$$u_x(\theta, z, t_w) = \frac{1}{2\mu(R_0 - h_0)} \frac{\partial p}{\partial \theta} z(z - h(\theta, t_w)) \quad (9.3)$$

Integrating the continuity equation twice across the gap, with $u_r = 0$ at the outer boundary, $u_r = U \cos \theta$ at the inner translating boundary, and $u_\theta = u_z = 0$ at both boundaries, we find the pressure distribution

$$p(\theta, t_w) = p_0(t_w) - \frac{3\mu_o(R_0 - h_0)^2 U}{\delta h^2} \quad (9.4)$$

Balancing forces in the z direction, $2\pi \int_{\theta=0}^{\pi} p \mathbf{n} \cdot \mathbf{e}_z \sin \theta d\theta = F^b$, where $F^b \equiv (4/3)\pi(R_0 - h_0)^3 \Delta \rho g$ is the buoyant force on the inner sphere and $\Delta \rho$ is the difference in density between the inner and outer spheres (0.08 g/cm^3). We complete the integral and substitute $U = \partial \delta / \partial t_w$, and take the limit $\delta/h_0 \rightarrow 1$ [318]; we obtain

$$\frac{1}{h_0 - \delta} \frac{\partial \delta}{\partial t_w} = \frac{F^b h_0^2}{6\pi\mu_o(R_0 - h_0)^4} \implies \frac{\delta(t_w)}{h_0} = 1 - e^{-\frac{2\Delta\rho g h_0^2 t_w}{9\mu_o(R_0 - h_0)}} \quad (9.5)$$

To test this prediction, we use SEM or confocal microscopy measurements of microcapsules with fluorescently-labeled shells to directly measure δ/h_0 for microcapsules of varying t_w . We find good agreement between the two, particularly for large t_w , when δ/h_0 precipitously rises to 1, as shown in Figure 9.7. We find $\delta/h_0 \rightarrow 0.2$ as $t_w \rightarrow 0$, in contrast to the theory; this is to be expected, due to the slight bias in the inner droplet position as the double emulsions are formed in the microfluidics device.

We use Equation 9.5 to relate our measurements of τ to δ/h_0 . Remarkably, we find good agreement between our data and Equation 9.2, with $k \approx 3.5 \times 10^{-24} \text{ m}^2$, as shown by the black line in Figure 9.5(f); in particular, this simple picture captures the strong decrease

in τ at $t_w \sim 10^3$ s, with a shell permeability consistent with our independent measurements [Figure 9.6]. While these results do not rule out other possible functional forms of τ , they further suggest that the time delay before the onset of buckling can be understood by combining shell theory with Darcy's law for flow through the microcapsule shell, even for very inhomogeneous shells.

9.4 Shell inhomogeneities guide microcapsule deformations

The shell thickness inhomogeneity may continue to guide the development of deformations in a microcapsule after it buckles. To explore this possibility, we use optical microscopy to monitor the evolution of the microcapsule morphologies after the onset of buckling. Slightly inhomogeneous microcapsules typically buckle through the sudden formation of a single circular indentation. As this indentation grows over time, its perimeter eventually sharpens into straight ridges connected by 2-3 vertices [283, 291, 319]; this folding pathway is exemplified by microcapsules polymerized *in situ*, characterized by $\delta/h_0 \approx 0.2$, as shown in Figure 9.8(a). This sharpening reflects the unique physics of thin shells: because it is more difficult to compress the microcapsule shell than it is to bend it, localizing compressive deformations only along sharp lines and points on the microcapsule surface requires less energy than uniformly compressing the shell [257]. Interesting differences arise for very inhomogeneous microcapsules polymerized after $t_w = 1$ day, characterized by $\delta/h_0 \approx 0.84$. The initial folding pathway is similar; however, the perimeters of the indentations formed in these microcapsules sharpen into straight ridges connected by 4-5 vertices, more than in the slightly inhomogeneous case, as shown in Figure 9.8(b). Moreover, surprisingly, roughly 30% of the very inhomogeneous microcapsules begin to

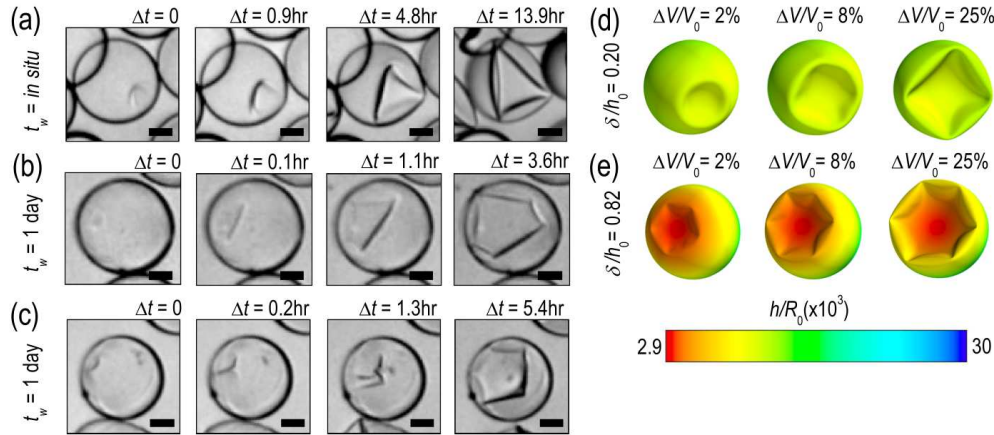


Figure 9.8: Folding pathways for different shell inhomogeneities. (a-c) Optical microscope images exemplifying buckling at $\Pi \approx 0.86$ MPa of (a) slightly inhomogeneous microcapsules polymerized *in situ* ($t_w \approx 0$), with $\delta/h_0 \approx 0.2$, (b-c) very inhomogeneous microcapsules polymerized after a wait time $t_w = 1$ day, with $\delta/h_0 \approx 0.84$. Very inhomogeneous microcapsules buckle through the formation of either (b) one single indentation or (c) two indentations. Δt is time elapsed after buckling. Scale bars are $35\mu\text{m}$. (d-e) Examples of simulated shells with similar geometries as the microcapsules shown in (a-c), for varying fractional volume reduction $\Delta V/V_0$. Color scale indicates the spatially-varying shell thickness.

buckle through the formation of one, then two, adjacent indentations, as exemplified in Figure 9.8(c). The perimeters of these indentations grow over time, eventually meeting, coalescing, and sharpening into straight ridges connected by 4-5 vertices [Figure 9.8(c)]. These observations directly demonstrate that the deformations of a microcapsule after it buckles are sensitive to the shell inhomogeneity.

To gain insight into this behavior, we perform numerical simulations of two different shells, a slightly inhomogeneous shell with $\delta/h_0 = 0.20$, and a very inhomogeneous shell with $\delta/h_0 = 0.82$, similar to the experimental microcapsules. As the shell volume is reduced below $V_0 - \Delta V^*$, both shells buckle through the formation of a single indentation centered at the thinnest part of the shell, as shown in the leftmost panels of Figure

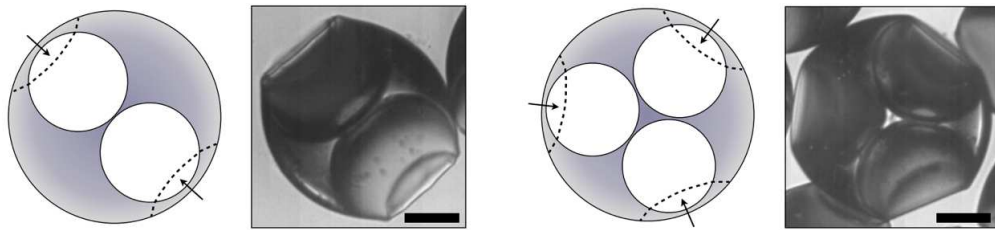


Figure 9.9: Designing lock-and-key colloids. Microcapsules with two or three spherical interior compartments, schematized in left panels, buckle at “weak spots” (arrows). This forms shapes with two or three equally-spaced circular indentations after buckling (right panels). Scale bars are $100\mu\text{m}$.

9.8(d-e). As ΔV increases, this indentation grows and its edges sharpen. We find that the indentations formed in the very inhomogeneous shells begin to sharpen at smaller $\Delta V/V_0$, and ultimately develop more vertices than those formed in more homogeneous shells [Figure 9.8(d-e)]. These results qualitatively agree with our experimental observations [Figure 9.8(a-c)], further confirming that after the onset of buckling, the folding pathway of a shell depends on the inhomogeneity. However, in contrast to the experimental microcapsules [Figure 9.8(c)], we do not systematically observe the formation of adjacent indentations in the simulations on very inhomogeneous shells. This presents a puzzle requiring further inquiry.

Our microcapsules may be used to guide colloidal self-assembly; for example, a colloidal particle can spontaneously bind to the indentation formed during buckling through a lock-and-key mechanism [320]. This mechanism is typically applied to a homogeneous colloidal particle, which buckles through the formation of a single indentation at a random position on its surface. We apply our findings to create multiply-indented microcapsules having two-fold or three-fold symmetry. To do this, we form double emulsions with two or three inner droplets of radii larger than half the radius of the outer droplet. Consequently,

the inner droplets pack closely to form dimers or trimers [321], as shown schematically in Figure 9.9. The double emulsions are then polymerized, forming solid microcapsules with two or three spherical compartments in their interiors, and two or three equally-spaced “weak spots” in the microcapsule shell [arrows in Figure 9.9]. When exposed to a sufficiently large osmotic pressure, these microcapsules buckle through the formation of multiple, equally-spaced indentations at the weak spots, as shown in Figure 9.9. This approach is thus a versatile way to create microcapsules of desired symmetries, and extends the range of structures that can be used for lock-and-key colloidal assembly.

Our results may be applicable to other thin, spherical shells, such as biological cells [322, 323], pollen grains [285], submersibles [324], chemical storage tanks [325], nuclear containment shells [325], and even the earth’s crust [326]. Indeed, many of these shells are inhomogeneous, similar to the microcapsules described here [285, 327, 328, 329, 330].

Chapter 10

Expansion and rupture of pH-responsive microcapsules

One common way of characterizing the mechanical properties of a microcapsule is to monitor how it responds to forces exerted on its shell. These can be mechanical forces, externally imposed by poking, squeezing, or uniformly pressurizing the microcapsule, as described in the previous Chapter [331, 332, 333, 5]. Alternatively, these forces can arise through physico-chemical modifications to the shell itself, such as charging it; under certain conditions, the repulsion between the charges on the shell can cause it to deform. Electrostatic forces arise in many applications of soft matter, and consequently, this approach is frequently used to induce deformations in a variety of bulk materials [334, 335]. Nevertheless, systematic investigations of how electrostatic forces deform microcapsules are scarce [336, 337, 338]. Thus, despite the prevalence of these forces in many real-world situations, a full understanding of how they affect microcapsules is lacking.

In this Chapter⁹, we study the deformations of spherical microcapsules exposed to a pH stimulus. We choose NaOH as the stimulus; when exposed to this base, the microcapsule shells become highly charged. For large NaOH concentrations, the microcapsules expand isotropically. We find that the extent of the microcapsule expansion can be understood by coupling electrostatics with shell theory; moreover, the dynamics of this expansion is well described by Darcy's law for flow through the porous microcapsule shell. Surprisingly, below a threshold NaOH concentration, the microcapsules begin to disintegrate, and eventually rupture; they then expand non-uniformly, ultimately forming large, jellyfish-like structures. Our results thus highlight the rich behavior exhibited by microcapsules under the influence of electrostatic forces.

We first describe the production of microcapsules composed solely of a pH-responsive polymer; when exposed to a trigger pH, this shell dissolves at a constant rate, ultimately releasing the microcapsule contents. In the next section, we describe the production of hybrid microcapsules with shells composed of a mixture of a pH-responsive and a pH-unresponsive polymer. These microcapsules do not dissolve when exposed to a trigger pH, but instead, become highly charged. We then use these hybrid microcapsules to study how electrostatic forces can be used to deform spherical microcapsules.

⁹Based on "Expansion and rupture of pH-responsive microcapsules", **S. S. Datta***, A. Abbaspourrad*, and D. A. Weitz, submitted, *Materials Horizons* (2013) and "Controlling release from pH-responsive microcapsules", A. Abbaspourrad*, **S. S. Datta***, and D. A. Weitz, submitted, *Langmuir* (2013) *Equal contribution.

10.1 Microcapsules composed solely of a pH-responsive polymer

We use a glass capillary microfluidic device to prepare monodisperse W/O/W double emulsion drops as templates to form microcapsules [339]. The device consists of two tapered cylindrical capillaries inserted into the opposite ends of a square capillary, whose inner dimension is slightly larger than the outer diameter of the cylindrical capillaries, as illustrated by the optical micrograph in Figure 10.1(a). This configuration enables us to accurately align both cylindrical capillaries. We use the left cylindrical capillary to inject the innermost aqueous phase, a 5 wt% aqueous solution of polyvinyl alcohol (PVA) of molecular weight 13,000-23,000, seeded with a small amount of 6 nm-diameter quantum dots for flow visualization. We treat this capillary with n-octadecyl trimethoxy silane; this renders its surface hydrophobic, preventing wetting of the aqueous phase on the capillary wall. To fabricate solid microcapsules, we use a middle oil phase comprised of a 5-15 wt% solution of an anionic diblock copolymer of methacrylic acid and methyl methacrylate (PAA-b-PMMA) in a mixture of 70 vol% chloroform and 30 vol% tetrahydrofuran (THF)[340]. We inject this oil from the left, forcing it to flow in the same direction as the inner aqueous phase, through the interstices between the left cylindrical capillary and the square capillary. The outermost aqueous phase is a 10 wt% aqueous solution of PVA containing 15 wt% THF; we inject it from the right, forcing it to flow in the opposite direction, through the interstices between the right cylindrical capillary and the square capillary. We operate this hydrodynamic focusing geometry in the dripping regime, causing the inner and middle phases to break up at the orifice of the right cylindrical capillary; this forms monodisperse

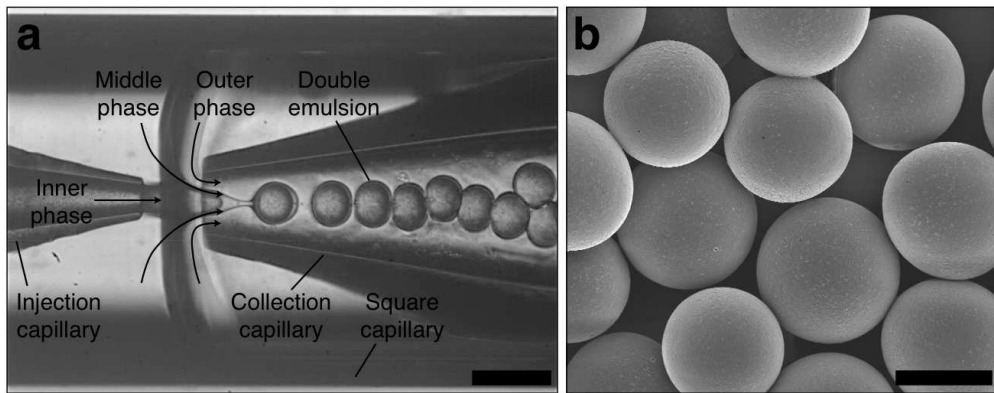


Figure 10.1: Microcapsules produced using microfluidics. (a) Optical micrograph of a glass capillary microfluidic device as it produces monodisperse double emulsions. Scale bar is 250 μm . (b) Scanning electron microscope micrograph of monodisperse, uniform, solid microcapsules formed after evaporation of the solvent from the middle phase of the double emulsion drops. Scale bar is 100 μm .

W/O/W double emulsions, as shown in Figure 10.1(a).

We use the right cylindrical capillary to collect these double emulsion drops; this capillary is treated with 2-(methoxy(polyethyleneoxy)propyl) trimethoxy silane, rendering its surface hydrophilic and preventing wetting of the middle oil phase on the capillary wall. After the double emulsion drops are collected, the solvent in the middle oil phase slowly diffuses into the outer continuous phase; this forces the PAA-b-PMMA to precipitate. Within one hour, this forms a uniform solid shell of radius $\approx 69 \mu\text{m}$, as exemplified in Figure 10.1(b). We wash the monodisperse microcapsules thus formed with water, adjusted to have $\text{pH} = 6$, three times to remove any surfactant from the continuous phase.

The resulting microcapsules stably encapsulate their contents over at least 30 days; however, when exposed to a basic $\text{pH} > 7$, the polymer chains making up the shells become highly charged and repel each other [340]. This causes the microcapsule shells to dissolve at a constant rate, starting at their exteriors; after a time delay of several minutes,



Figure 10.2: pH-triggered release from microcapsules. Optical micrographs showing the degradation of the 500 nm-thick shell of a microcapsule, leading to the release of an encapsulated dye starting at 12 min (green; fluorescence micrograph superimposed). The microcapsules also encapsulate, and subsequently release, polystyrene particles used for enhanced visualization (grey). Scale bar is 100 μ m. Time stamp shows time elapsed after pH is raised to 9.

the shells become fully dissolved, and the microcapsules release their contents, as shown in Figure 10.2. We expect microcapsules with thicker shells to take longer to fully dissolve and ultimately release their contents; thus, to control the time of release, we exploit the precise flow control afforded by microfluidics to prepare microcapsules of the same outer radius, but with different shell thicknesses. We do this by varying the flow rates of the inner and middle phases, Q_i and Q_m , respectively, while maintaining their sum, and the flow rate of the outer phase, Q_o , at constant values of 1.2 mL/hr and 6.0 mL/hr, respectively. Crucially, the thickness of the middle phase of each double emulsion drop, and consequently, the thickness of the solid shell formed from it, increases with increasing Q_m/Q_i , as shown in Figure 10.3(a). To quantify the release kinetics for microcapsules of different shell thicknesses, we monitor individual microcapsules using fluorescence microscopy, measuring the time between initiation of a trigger through exposure to a pH = 9 and the beginning of the release from their interiors [341]. The time delay increases linearly with increasing shell thickness, varying from just a minute up to tens of minutes, as shown in Figure 10.3(b); this is consistent with our expectation.

By fabricating and mixing varying amounts of different populations of capsules, each characterized by a different shell thickness, we can precisely control the distribution of release times over a range spanning one minute to nearly one hour. This enables us to program sequential release from different microcapsules; to illustrate this, we fabricate and mix two different populations of microcapsules, having either thin 500 nm shells or thick 4 μ m shells. We distinguish the two populations by encapsulating a green and a red dye within the microcapsules having thin and thick shells, respectively [first frame, Figure 10.4]. We increase the pH of the continuous phase to 9, forcing the shells to dissolve. After two minutes, the microcapsules with thin shells release their contents; in contrast, the microcapsules with thicker shells continue to stably encapsulate their contents, as shown in the second and third frames of Figure 10.4. These subsequently release their contents after thirteen more minutes have passed, as shown in the last two frames of Figure 10.4. These results demonstrate that varying the microcapsule shell thickness provides a straightforward means of programming sequential release at different times.

This experimental approach can be used to trigger release at a range of different pH conditions. To illustrate its generality, we apply the same microfluidic device, but use a different middle oil phase; this enables us to prepare microcapsules that release their contents under acidic conditions. The oil phase is an 8 wt% solution of a cationic triblock copolymer of poly-(n-butyl methacrylate-(2-dimethylaminoethyl)-methacrylate-methyl methacrylate) (DMAEMA-BMA-MMA) in a mixture of 70 vol% chloroform and 30 vol% THF [342]. Similar to the previous case, after the double emulsion drops are formed and collected, the solvent in the middle oil phase slowly diffuses into the continuous phase; this forces the polymer to precipitate, forming a uniform solid shell. In contrast to the PAA-b-PMMA

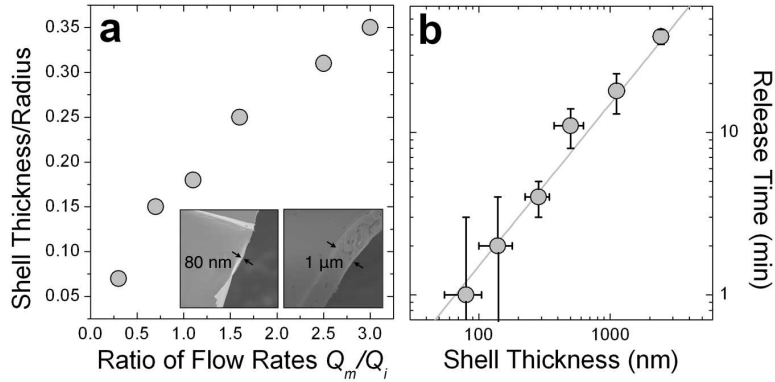


Figure 10.3: Controlling shell geometry using microfluidics. (a) Ratio of microcapsule shell thickness to shell radius, measured using scanning electron microscopy, increases with increasing ratio of middle phase flow rate Q_m to inner phase flow rate Q_i . Example scanning electron micrographs for thin and thick shells are shown in the inset. (b) Time delay before release begins, quantified using fluorescence microscopy of microcapsules encapsulating a fluorescent dye, increases with increasing shell thickness, for shells triggered at pH = 9; grey line shows linear relationship. Vertical error bars show standard deviation in measured release time, while horizontal error bars show standard deviation in shell thickness of each batch.

case, however, the DMAEMA-BMA-MMA polymer chains become highly charged only under acidic conditions; consequently, the microcapsule shells thus formed dissolve and release their contents only for pH < 6 [343, 344]. We are therefore able to prepare microcapsules that very stably encapsulate their contents, and only release them when exposed to either acidic or basic conditions.

This experimental approach enables us to program the sequential release of different actives upon exposure to different pH conditions; to illustrate this, we fabricate and mix two different populations of acid-responsive and base-responsive microcapsules. We distinguish the two populations by encapsulating a green dye within the base-responsive PAA-b-PMMA microcapsules, and a yellow dye, along with 1 μm polystyrene particles, within the acid-responsive DMAEMA-BMA-MMA microcapsules [first frame, Figure 10.5]. Both

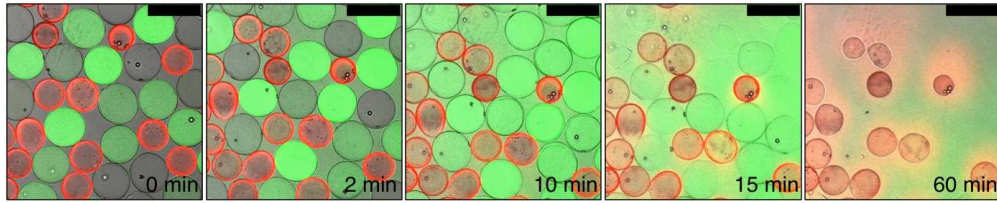


Figure 10.4: Controlling time of release. Optical micrographs showing the release, starting at 2 min, of an encapsulated dye from microcapsules with 500 nm-thick shells (green; fluorescence micrograph superimposed). A second encapsulated dye is then released, starting at 15 min, from microcapsules with 4 μm -thick shells (red; fluorescence micrograph superimposed). Scale bar is 250 μm . Time stamp shows time elapsed after pH is raised to 9.

populations of microcapsules are stable in water adjusted to have $\text{pH} = 6.5$. We then decrease the pH of the continuous phase to 5; while the base-responsive microcapsules remain stable, the acid-responsive microcapsules quickly release their contents, as shown in the second and third frames of Figure 10.5. We subsequently increase the pH of the continuous phase to 9; this forces the base-responsive microcapsules to also release their contents, as shown in the last two frames of Figure 10.5. These observations demonstrate that varying the microcapsule shell composition provides a straightforward means of programming sequential release at different pH.

10.2 Hybrid microcapsules

We fabricate monodisperse thin-shelled microcapsules using water-in-oil-in-water (W/O/W) double emulsion templates prepared by microfluidics [339]. The inner and outer phases are 6 wt % and 10 wt % solutions of polyvinyl alcohol (PVA), respectively, while the middle oil phase is a mixture of a pH-responsive polymer, suspended in tetrahydrofuran (THF), and another photo-polymerizable pH-unresponsive monomer. We use UV light to polymerize

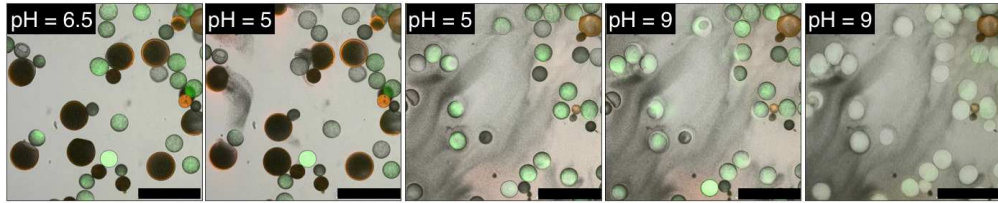


Figure 10.5: Programmed release at different pH values. Optical micrographs showing the release of an encapsulated dye only from acid-responsive DMAEMA-BMA-MMA microcapsules (yellow; fluorescence micrograph superimposed) when the pH is reduced to 5 [second and third frames]. A second encapsulated dye (green; fluorescence micrograph superimposed) and $1\mu\text{m}$ polystyrene particles (grey) are then released from base-responsive PAA-b-PMMA microcapsules when the pH is increased to 9 [fourth and fifth frames]. Scale bar is $500\mu\text{m}$. The shells of both types of capsules are 500 nm thick.

the pH-unresponsive monomer as the double emulsions are generated *in situ*, forming a highly cross-linked network around the inner core. This network is a solid characterized by a Young's modulus $E \approx 600 \text{ MPa}$ [315]; it is impermeable to hydrated Na^+ and OH^- ions, but is permeable to water [316, 5]. We then collect the microcapsules in water adjusted to have $\text{pH} = 6$, and let the THF evaporate; this forces the pH-responsive polymer to precipitate, completing the formation of a solid, hybrid shell [345], schematized in Figure 10.6(a). We then remove the supernatant, and repeatedly wash the microcapsules with pure water, to remove any surfactant from the continuous phase.

When exposed to NaOH , the pH-responsive polymer chains at the microcapsule exteriors become highly charged and repel each other; this repulsion is screened by any residual Na^+ or OH^- ions. To probe the microcapsule deformations under these conditions, we immerse them in an aqueous solution with $c_{\text{NaOH}} = 500 \text{ mM}$, and monitor them using optical microscopy. Strikingly, the hybrid microcapsules quickly become opaque, reflecting the development of heterogeneities in the shell, and abruptly expand in irregular shapes; representative optical micrographs of this process are shown in Figure 10.6(b). The micro-

capsules ultimately expand into spheres, as shown by the last frame of Figure 10.6(b); this entire process occurs over a timescale of ~ 10 s.

We quantify this behavior by measuring the maximal expansion, $\gamma \equiv (R_f - R_0)/R_0$, where R_0 and R_f are the average initial and final microcapsule radii, respectively. We also measure the average time taken for the microcapsules to expand into their final spherical shapes, τ . To elucidate the expansion behavior, we explore even lower values of c_{NaOH} . Intriguingly, γ increases strongly with decreasing c_{NaOH} , as shown in the upper panel of Figure 10.7, reaching a value exceeding 1 at $c_{NaOH} = 25$ mM; the expansion time τ concomitantly increases, but only weakly, as shown by the grey squares in the lower panel of Figure 10.7. Unexpectedly, at $c_{NaOH} = 25$ mM, the microcapsules also begin to disintegrate, forming fragments of size ~ 1 μm , as indicated by the arrows in Figure 10.6(c). At even smaller c_{NaOH} , the microcapsules first disintegrate, as shown by the first frame of Figure 10.6(d); this ultimately results in the formation of a hole in each shell after a time delay $\tau_1 \sim 10 - 100$ s. The microcapsules then begin to intermittently expand outward, starting at the hole perimeters, as exemplified by the last three frames of Figure 10.6(d); the region of the shell that expands is indicated by the arrow in each frame. This process occurs over a time period $\tau_2 \sim 10 - 100$ s; the expansion then stops, leaving wrinkled jellyfish-like structures, approximately 300 μm in size.

The isotropic expansion at high $c_{NaOH} \geq 25$ mM is due to the charging of the microcapsule shells; when exposed to NaOH, the pH-responsive polymers at the microcapsule exteriors become highly charged, leading to a surface charge density σ . We thus expect that the repulsion between the charges on each spherically-symmetric shell leads to a force, directed radially outward, on the shell. We estimate [346] the magnitude of the resultant

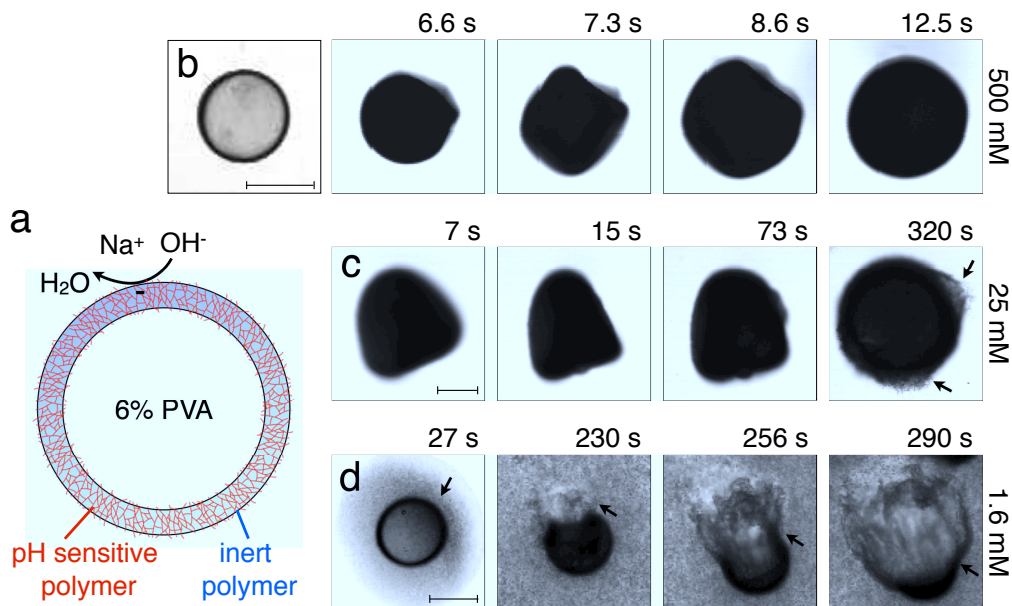


Figure 10.6: Expansion and rupture of microcapsules. (a) Schematic of a hybrid microcapsule, showing the thin, solid, spherical shell composed of a pH-unresponsive polymer and a pH-responsive polymer. The core is a 6 wt% aqueous solution of polyvinyl alcohol (PVA). The pH-responsive polymer at the surface of the shell becomes charged when exposed to NaOH in the continuous phase. First frame of (b) shows an optical micrograph of a hybrid microcapsule after it is collected. Subsequent frames in (b), (c), and (d) show the expansion of the microcapsule when exposed to different NaOH concentrations. (c) At $c_{NaOH} = 25 \text{ mM}$, the shell begins to disintegrate, as indicated by the arrows in the last frame. (d) For lower $c_{NaOH} < 25 \text{ mM}$, the shell first disintegrates, as indicated by the arrow in the first frame, then ruptures through the formation of a hole, shown in the second frame, then expands into a wrinkled jellyfish-like structure, shown in the last two frames. Scale bars indicate $100 \mu\text{m}$.

electrostatic pressure as $p_e \approx \sigma^2 \kappa^{-1} / \epsilon \epsilon_0 R$, where $\epsilon \approx 80$ is the dielectric constant of water, ϵ_0 is the permittivity of free space, R is the time-dependent radius of the spherical microcapsule, κ^{-1} is the length over which the repulsive interactions are screened. The quantity of NaOH required to fully charge the shell is small; consequently, the excess Na^+ and OH^- ions, which screen the surface charges on the shell, have a concentration $\approx c_{\text{NaOH}}$, and thus $\kappa^{-1} = A / \sqrt{c_{\text{NaOH}}}$, with $A \equiv 0.304 \text{ nm} \cdot \text{M}^{1/2}$ [347]. As the microcapsule expands isotropically, a tensile stress builds up within its shell; this resists the expansion. We use shell theory to estimate this stress, $p_m = Eh(1/R_0 - 1/R)$, where $h \approx 3 \mu\text{m}$ is the average shell thickness, measured using scanning electron microscopy [317]. We thus expect that the microcapsules expand until the electrostatic pressure and tensile stress balance each other; this yields a maximal expansion strain $\gamma = \sigma^2 A / E \epsilon \epsilon_0 h \sqrt{c_{\text{NaOH}}}$. We test this prediction using our measurements of γ . We find $\gamma \sim c_{\text{NaOH}}^{-1/2}$, as shown by the line in the top panel of Figure 10.7, consistent with the theoretical prediction; fitting the experimental data yields an estimate of $\sigma \approx 300 \text{ e/nm}^2$, where e is the charge of an electron. These results suggest that the microcapsule expansion can be understood by coupling electrostatics with shell theory.

Within this picture, the Na^+ and OH^- ions screen the repulsion between the charges on the microcapsule shells. As an additional test of this idea, we expose the microcapsules to a 25 mM NaOH solution, also containing 500 mM NaCl; we expect the Na^+ and Cl^- ions to similarly screen the repulsion between the charges on the microcapsule shells. Consistent with our expectation, the microcapsules do not disintegrate, unlike microcapsules exposed to only 25 mM NaOH. Instead, they expand slightly, reaching a maximal expansion strain $\gamma \approx 0.4$, much smaller than that expected for c_{NaOH} . This value of the strain is instead

comparable to that expected for $c_{NaOH} = 525$ mM, as shown by the line in the top panel of Figure 10.7, thus confirming the validity of our picture.

The microcapsules expand to their maximal size over a time period τ . We hypothesize that this behavior reflects the dynamics of the fluid flow into the microcapsule cores, through their porous shells, as they expand [5]. We estimate this inflow rate using Darcy's law, $p_e - p_m = \mu h \dot{R} / 3k$, where $\mu \approx 1$ mPa · s is the viscosity of water and k is the shell permeability; this yields a characteristic expansion time $\tau = \mu R_0^2 (1 + \gamma) / 3Ek$. We use our measurements of τ , as well as the fit to the measurements of γ shown in the top panel of Figure 10.7, to directly test this prediction. We find excellent agreement between the data and the theoretical prediction, as shown by the solid line in the bottom panel of Figure 10.7; fitting the experimental data yields a shell permeability $k \approx 10^{-21}$ m². The agreement between the data and the theoretical prediction thus suggests that the dynamics of the microcapsule expansion can be understood using Darcy's law.

As c_{NaOH} decreases, the screening length κ^{-1} increases; consequently, the stress in the microcapsule shell increases, ultimately reaching $p_m = p_e \approx 10$ MPa at $c_{NaOH} = 25$ mM. For even smaller c_{NaOH} , the microcapsules begin to disintegrate into ~ 1 μm fragments, and eventually rupture. We hypothesize that, under these conditions, the stress that builds up in the shell exceeds the stress required to fracture it. To test this hypothesis, we estimate the fracture stress [348] using the Griffith criterion, $\sqrt{2EG_c/\pi a} \approx 6 - 20$ MPa, where $G_c \sim 0.1 - 1$ J/m² is the surface energy per unit area of the shell material and $a \approx 1$ μm is the characteristic size of a shell fragment, measured using optical microscopy. Interestingly, this value is in good agreement with our estimate of the maximal stress that develops in the shell, $p_m \approx 10$ MPa, suggesting that the observed disintegration at $c_{NaOH} \leq 25$ mM reflects

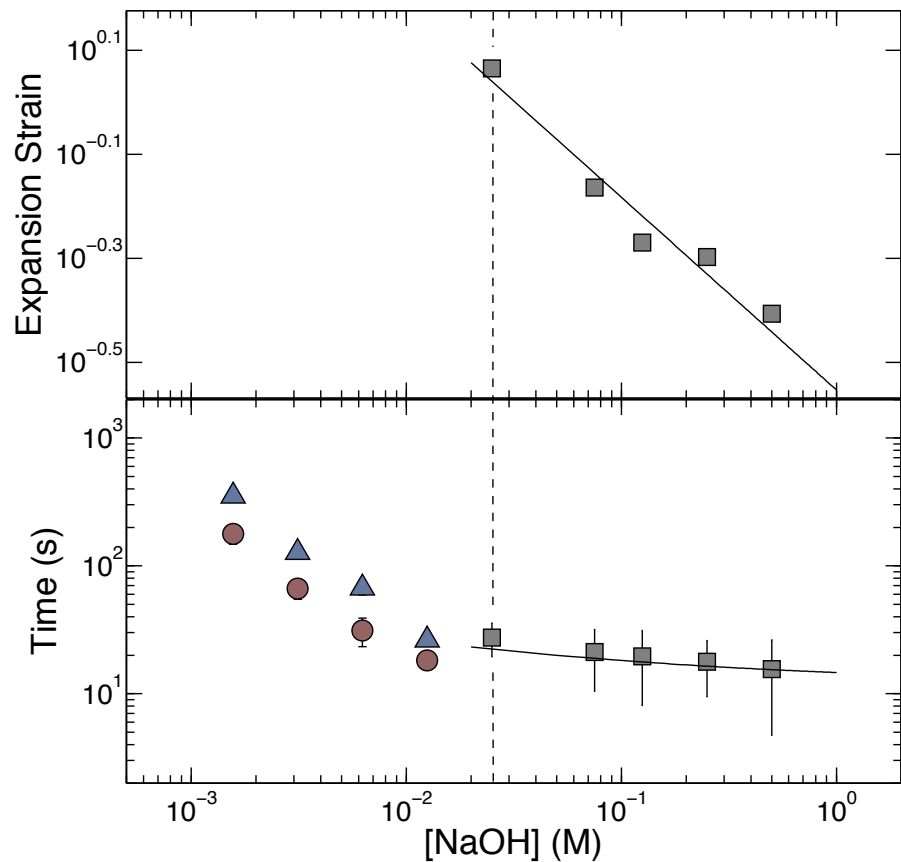


Figure 10.7: Geometry and dynamics of microcapsule expansion. (Top Panel) Maximal expansion strain of spherical microcapsules exposed to different NaOH concentrations; line shows theoretical prediction described in the text, with $\sigma \approx 300 \text{ e/nm}^2$, where e is the elementary charge. (Bottom Panel) Grey squares show time taken for spherical microcapsules to fully expand; line shows theoretical fit described in the text. Blue triangles and red circles the time period over which the shell disintegrates before a hole forms in it, τ_1 , and the time period over which the shell subsequently expands into a jellyfish-like structure, τ_2 , respectively, for $c_{NaOH} < 25 \text{ mM}$.

the fracturing of the microcapsule shell.

Finally, we monitor the dynamics of the disintegration, rupture, and subsequent expansion of the microcapsule shell that occurs at $c_{NaOH} < 25$ mM. Intriguingly, both the time period over which the shell fractures before a hole forms in it, τ_1 , and the time period over which the shell subsequently expands into a jellyfish-like structure, τ_2 , both increase with decreasing c_{NaOH} , as shown by the blue triangles and red circles in Figure 10.7, respectively. A complete understanding of these dynamics remains a puzzle requiring further inquiry.

Our work highlights the fascinating range of structures exhibited by pH-responsive microcapsules, driven by the interplay between electrostatic and mechanical forces. Intriguingly, many of these structures are reminiscent of structures, also induced by electrostatic effects, that are often observed in other soft matter systems, such as viruses [346, 349, 350] and red blood cells [351].

Bibliography

- [1] J. Bear. *Dynamics of Fluids in Porous Media*. Dover, 1988.
- [2] W. C. Yang. *Handbook of Fluidization and Fluid-Particle Systems*. CRC Press, 2003.
- [3] J. C. Giddings. *Dynamics of Chromatography*. CRC Press, 2002.
- [4] M. M. Mench. *Fuel Cell Engines*. Wiley, 2008.
- [5] S. S. Datta, S. H. Kim, J. Paulose, A. Abbaspourrad, D. R. Nelson, and D. A. Weitz. Delayed buckling and guided folding of inhomogeneous capsules. *Phys. Rev. Lett.*, 109:134302, 2012.
- [6] A. R. A. Khaled and K. Vafai. The role of porous media in modeling flow and heat transfer in biological tissues. *Int. J. Heat and Mass Transfer*, 46:4989–5003, 2003.
- [7] J. Ranft, J. Prost, F. Julicher, and J. F. Joanny. Tissue dynamics with permeation. *Eur. Phys. J. E*, 35:46, 2012.
- [8] S. Veran-Tissoires, M. Marcoux, and M. Prat. Discrete salt crystallization at the surface of a porous medium. *Phys. Rev. Lett.*, 108:054502–054505, 2012.
- [9] J. M. Rutkowski and M. A. Swartz. A driving force for change: interstitial flow as a morphoregulator. *Trends in Cell Biol.*, 17:44–50, 2006.
- [10] W. Rose and P. A. Witherspoon. Studies of waterflood performance II: trapping oil in a pore doublet. *Ill. State Geological Survey*, 224:3, 1956.
- [11] E. F. Herbeck, R. C. Hemtz, and J. R. Hastings. Fundamentals of tertiary oil recovery. *Pet. Engineer*, 48:33, 1976.
- [12] A. C. Payatakes. Dynamics of oil ganglia during immiscible displacement in water-wet porous media. *Annu. Rev. Fluid Mech.*, 14:365, 1982.
- [13] I. Chatzis and F. A. L. Dullien. Application of the theory of percolation for a model of drainage in porous media and relative permeability of injected non-wetting fluids. *Oil Gas Sci. Technol. Rev. IFP*, 37:183, 1982.

Bibliography

- [14] R. Lenormand, C. Zarcone, and A. Sarr. Mechanisms of the displacement of one fluid by another in a network of capillary ducts. *J. Fluid Mech.*, 135:337, 1983.
- [15] R. Lenormand and C. Zarcone. Role of roughness and edges during imbibition in square capillaries. *SPE Annual Technical Conference and Exhibition*, pages SPE–13264, 1984.
- [16] G. R. Jerauld and S. J. Salter. The effect of pore-structure on hysteresis in relative permeability and capillary pressure: pore-level modeling. *Transp. Porous Media*, 5:103, 1990.
- [17] M. J. Blunt and H. Scher. Pore-level modeling of wetting. *Phys. Rev. E*, 52:6387, 1995.
- [18] M. J. Blunt, M. D. Jackson, M. Piri, and P. H. Valvatne. Detailed physics, predictive capabilities and macroscopic consequences for pore-network models of multiphase flow. *Adv. Water Resour.*, 25:1069, 2002.
- [19] I. Chatzis, N. R. Morrow, and H. T. Lim. Magnitude and detailed structure of residual oil saturation. *Soc. Pet. Eng. J.*, 23:311, 1983.
- [20] M. Sahimi. *Flow and Transport in Porous Media and Fractured Rock*. Wiley, 2012.
- [21] D. Wilkinson. Percolation effects in immiscible displacement. *Phys. Rev. A*, 34:1380, 1986.
- [22] S. Sheppard, M. D. Mantle, A. J. Sederman, M. L. Johns, and L. F. Gladden. Magnetic resonance imaging study of complex fluid flow in porous media: flow patterns and quantitative saturation profiling of amphiphilic fracturing fluid displacement in sandstone cores. *Magn. Reson. Imag.*, 21:364, 2003.
- [23] M. H. Sankey, D. J. Holland, A. J. Sederman, and L. F. Gladden. Magnetic resonance velocity imaging of liquid and gas two-phase flow in packed beds. *J. Magn. Reson.*, 196:142, 2008.
- [24] M. L. Porter, D. Wildenschild, G. Grant, and J. I. Gerhard. Measurement and prediction of the relationship between capillary pressure, saturation, and interfacial area in a NAPL-water-glass bead system. *Water Resour. Res.*, 46:W08512, 2010.
- [25] D. Wildenschild, R. T. Armstrong, A. L. Herring, I. M. Young, and J. W. Carey. Exploring capillary trapping efficiency as a function of interfacial tension, viscosity, and flow rate. *Energy Procedia*, 4:4945, 2011.
- [26] S. Iglauer, S. Favretto, G. Spinelli, G. Schena, and M. J. Blunt. X-ray tomography measurements of power-law cluster size distributions for the non-wetting phase in sandstones. *Phys. Rev. E*, 82:056315, 2010.

Bibliography

- [27] M. Kumar, T. J. Senden, A. P. Sheppard, J. P. Middleton, and M. A. Knackstedt. Visualizing and quantifying the residual phase distribution in core material. *Petro-physics*, 51:v51n5a4, 2010.
- [28] L. Lebon, L. Oger, J. Leblond, J. P. Hulin, N. S. Martys, and L. M. Schwartz. Pulsed gradient NMR measurements and numerical simulation of flow velocity distribution in sphere packings. *Phys. Fluids*, 8:293–301, 1996.
- [29] L. Lebon, J. Leblond, and J. P. Hulin. Experimental measurement of dispersion processes at short times using a pulsed field gradient NMR technique. *Phys. Fluids*, 9:481–490, 1997.
- [30] D. R. Noble. *Lattice Boltzmann study of the interstitial hydrodynamics and dispersion in steady inertial flows in large randomly packed beds*. PhD thesis, University of Illinois and Urbana-Champaign, 1997.
- [31] Olav van Genabeek. *Velocity fluctuations in slow flow through porous media*. PhD thesis, Massachusetts Institute of Technology, 1998.
- [32] R. S. Maier, D. M. Kroll, Y. E. Kutsovsky, H. T. Davis, and R. S. Bernard. Simulation of flow through bead packs using the lattice Boltzmann method. *Phys. Fluids*, 10:60–74, 1998.
- [33] R. S. Maier, D. M. Kroll, H. T. Davis, and R. S. Bernard. Simulation of flow in bidisperse sphere packings. *J. Coll. Int. Sci.*, 217:341–347, 1999.
- [34] L. Talon, J. Martin, N. Rakotomalala, D. Salin, and Y. C. Yortsos. Lattice BGK simulations of macrodispersion in heterogeneous porous media. *Water Resour. Res.*, 39:1135–1141, 2003.
- [35] E. Zaman and P. Jalali. On hydraulic permeability of random packs of monodisperse spheres: Direct flow simulations versus correlations. *Physica A*, 389:205–214, 2010.
- [36] N. S. Martys, S. Torquato, and D. P. Bentz. Universal scaling of fluid permeability for sphere packings. *Phys. Rev. E*, 50:403–408, 1994.
- [37] F. M. Auzerais, J. Dunsmuir, B. B. Ferreol, N. Martys, J. Olson, T. S. Ramakrishnan, D. H. Rothman, and L. M. Schwartz. Transport in sandstone: A study based on three dimensional microtomography. *Geophys. Res. Lett.*, 23:705–708, 1996.
- [38] A. E. Scheidegger. *The physics of flow through porous media*. University of Toronto press, 1974.
- [39] G. De Josselin de Jong. Longitudinal and transverse diffusion in granular deposits. *Trans. Amer. Geophys. Union*, 39:67–74, 1958.

Bibliography

- [40] P. G. Saffman. A theory of dispersion in a porous medium. *J. Fluid Mech.*, 6:321–349, 1959.
- [41] J. Sheng. *Modern Chemical Enhanced Oil Recovery: Theory and Practice*. Gulf Professional Publishing, 2010.
- [42] S. P. Friedman and Y. Mualem. Diffusion of fertilizers from controlled release sources, uniformly distributed in soil. *Fert. Res.*, 39:19, 1994.
- [43] K. Tsuji. Microencapsulation of pesticides and their improved handling safety. *J. Microencapsul.*, 18:137, 2001.
- [44] K. Hirech, S. Payan, G. Carnelle, L. Brujes, and J. Legrand. Microencapsulation of an insecticide by interfacial polymerisation. *Powder Technol.*, 130:324, 2003.
- [45] C. C. Dowler, O. D. Dailey, and B. G. Mullinix. Polymeric microcapsules of alachlor and metolachlor: preparation and evaluation of controlled-release properties. *J. Agric. Food Chem.*, 47:2908, 1999.
- [46] T. Takei, M. Yoshida, K. Yanagi, Y. Hatake, K. Shiromori, and S. Kiyoyama. Preparation of acetamiprid-loaded polymeric microcapsules: Influence of preparation parameter in emulsion system on microcapsule characteristics. *Polymer Bulletin*, 61:119, 2008.
- [47] S. Riyajan and J. T. Sakdapipanich. Development of a controlled release neem capsule with a sodium alginate matrix, crosslinked by glutaraldehyde and coated with natural rubber. *Polymer Bulletin*, 63:609, 2009.
- [48] M. A. Augustin and Y. Hemar. Nano- and micro-structured assemblies for encapsulation of food ingredients. *Chem. Soc. Rev.*, 38:902, 2009.
- [49] A. Madene, M. Jacquot, J. Scher, and S. Desobry. Flavour encapsulation and controlled release – a review. *Int. J. Food Sci. Technol.*, 41:1, 2006.
- [50] D. J. McClements, Decker E. A, and J. Weiss. Emulsion-based delivery systems for lipophilic bioactive components. *J. Food Sci.*, 72:109, 2007.
- [51] R. Wegmueller, M. B. Zimmermann, V. G. Buhe, E. J. Windhab, and R. F. Hurrell. Development, stability, and sensory testing of microcapsules containing iron, iodine, and vitamin a for use in food fortification. *J. Food Sci.*, 71:2, 2006.
- [52] B. G. De Geest, C. De Jugnat, E. Verhoeven, G. B. Sukhorukov, A. M. Jonas, J. Plain, J. Demeester, and S. C. De Smedt. Layer-by-layer coating of degradable microgels for pulsed drug delivery. *J. Controlled Release*, 116:159, 2006.

Bibliography

- [53] G. Ibarz, L. Dahne, E. Donath, and H. Mohwald. Smart micro- and nanocontainers for storage, transport, and release. *Adv. Mater.*, 13:1324, 2001.
- [54] S. Ye, C. Wang, X. Liu, Z. Tong, B. Ren, and F. Zeng. New loading process and release properties of insulin from polysaccharide microcapsules fabricated through layer-by-layer assembly. *J. Controlled Release*, 112:79, 2006.
- [55] H. Ai, S. A. Jones, M. M. Villiers, and Y. M. Lvov. Nano-encapsulation of furosemide microcrystals for controlled drug release. *J. Controlled Release*, 86:59, 2003.
- [56] S. H. Hu, C. H. Tsai, C. F. Liao, D. M. Liu, and S. Y. Chen. Controlled rupture of magnetic polyelectrolyte microcapsules for drug delivery. *Langmuir*, 24:11811, 2008.
- [57] D. G. Shchukin, D. A. Gorin, and H. Mohwald. Ultrasonically induced opening of polyelectrolyte microcontainers. *Langmuir*, 22:7400, 2006.
- [58] B. G. De Geest, A. G. Skirtach, A. A. Mamedov, A. A. Antipov, N. A. Kotov, S. C. De Smedt, and G. B. Sukhorukov. Ultrasound-triggered release from multilayered capsules. *Small*, 3:804, 2007.
- [59] C. H. Choi, J. H. Jung, D. W. Kim, Y. M. Chung, and C. S. Lee. Novel one-pot route to monodisperse thermosensitive hollow microcapsules in a microfluidic system. *Lab on a Chip*, 8:1544, 2008.
- [60] T. He, K. Zhang, X. Mu, T. Luo, Y. Wang, and G. Luo. A modified microfluidic chip for fabrication of paclitaxel-loaded poly(l-lactic acid) microspheres. *Microfluid. Nanofluid.*, 10:1289, 2011.
- [61] R. Karnik, F. Gu, P. Basto, C. Cannizzaro, L. Dean, W. Kyeimanu, R. Langer, and O. C. Farokhzad. Microfluidic platform for controlled synthesis of polymeric nanoparticles. *Nano Lett.*, 8:2906, 2008.
- [62] S. Leclercq, K. R. Harlander, and G. A. Reineccius. Formation and characterization of microcapsules by complex coacervation with liquid or solid aroma cores. *Flavour and Fragrance Journal*, 24:17, 2008.
- [63] K. Miyazawa, I. Yajima, I. Kaneda, and T. Yanaki. Preparation of a new soft capsule for cosmetics. *J. Cosmet. Sci.*, 51:239, 2000.
- [64] M. Jacquemond, N. Jeckelmann, L. Ouali, and O. P. Haefliger. Perfume-containing polyurea microcapsules with undetectable levels of free isocyanates. *J. Appl. Polymer Sci.*, 114:3074, 2009.

Bibliography

- [65] T. Feczko, V. Kokol, and B. Voncina. Preparation and characterization of ethylcellulose-based microcapsules for sustaining release of a model fragrance. *Macromolecular Research*, 18:636, 2010.
- [66] R. Badulescu, V. Vivod, D. Jausovec, and B. Voncina. Grafting of ethylcellulose microcapsules onto cotton fibers. *Carbohyd. Polym.*, 71:85, 2008.
- [67] G. Orive, R. M. Hernandez, A. R. Gascon, R. Calafiore, T. M. S. Chang, P. de Vos, G. Hortelano, D. Hunkeler, I. Lacik, A. M. Shapiro, and J. L. Pedraz. Cell encapsulation: promise and progress. *Nat. Med.*, 9:104, 2003.
- [68] N. C. Hunt and L. M. Grover. Cell encapsulation using biopolymer gels for medical applications. *Biotechnol. Lett.*, 32:733, 2010.
- [69] T. Joki, M. Machluf, A. Atala, J. Zhu, N. T. Seyfried, I. F. Dunn, T. Abe, and R. S. Carroll. Continuous release of endostatin from microencapsulated engineered cells for tumor therapy. *Nat. Biotechnol.*, 19:35, 2001.
- [70] T. M. S. Chang. Therapeutic applications of polymeric artificial cells. *Nat. Rev. Drug Discov.*, 4:221, 2005.
- [71] T. Vermonden, N. E. Fedorovich, D. van Geemen, J. Alblas, C. F. van Nostrum, W. J. A. Dhert, and W. E. Hennink. Photopolymerized thermosensitive hydrogels: synthesis, degradation, and cytocompatibility. *Biomacromolecules*, 9:919, 2008.
- [72] H. Uludag, P. de Vos, and P. A. Tresco. Technology of mammalian cell encapsulation. *Adv. Drug Deliv. Rev.*, 42:29, 2000.
- [73] W. Qi, X. Yan, L. Duan, Y. Cui, Y., Yang, and J. Li. Glucose-sensitive microcapsules from glutaraldehyde cross-linked hemoglobin and glucose oxidase. *Biomacromolecules*, 10:1212, 2009.
- [74] M. J. McShane, J. Q. Brown, K. B. Guice, and Y. M. Lvov. Polyelectrolyte microshells as carriers for fluorescent sensors: loading and sensing properties of a ruthenium-based oxygen indicator. *Nanoscience and Nanotechnology*, 2:411, 2002.
- [75] L. I. Kazakova, L. I. Shabarchina, and G. B. Sukhorukov. Co-encapsulation of enzyme and sensitive dye as a tool for fabrication of microcapsule based sensor for urea measuring. *Phys. Chem. Chem. Phys.*, 13:11110, 2011.
- [76] L. E. Sinks, G. P. Robbins, E. Roussakis, T. Troxler, D. A. Hammer, and S. A. Vinogradov. Two-photon microscopy of oxygen: polymersomes as probe carrier vehicles. *J. Phys. Chem. B*, 114:14373, 2010.
- [77] S. L. Poe, M. Kobaslija, and D. T. McQuade. Mechanism and application of a microcapsule enabled multicatalyst reaction. *J. Am. Chem. Soc.*, 129:9216, 2007.

Bibliography

- [78] C. Ramaraoa, S. V. Ley, S. C. Smith, I. M. Shirley, and N. DeAlmeida. Polyurea encapsulated palladium acetate: a robust and recyclable catalyst for use in conventional and supercritical media. *Chem. Commun.*, 13:1132, 2002.
- [79] B. J. Blaiszik, M. M. Caruso, D. A. McIlroy, J. S. Moore, S. R. White, and N. R. Sottos. Microcapsules filled with reactive solutions for self-healing materials. *Polymer*, 50:990, 2009.
- [80] E. N. Brown, S. R. White, and N. R. Sottos. Microcapsule induced toughening in a self-healing polymer composite. *J. Mater. Sci.*, 39:1703, 2004.
- [81] M. A. White. The chemistry behind carbonless copy paper. *J. Chem. Educ.*, 75:1119, 1998.
- [82] B. Comiskey, J. D. Albert, H. Yoshizawa, and J. Jacobson. An electrophoretic ink for all- printed reflective electronic displays. *Nature*, 394:253, 1998.
- [83] C. A. Kim, M. J. Joung, S. D. Ahn, G. H. Kim, S. Y. Kang, I. K. You, J. Oh, H. J. Myoung, K. H. Baek, and K. S. Suh. Microcapsules as an electronic ink to fabricate color electrophoretic displays. *Synthetic Metals*, 151:181, 2005.
- [84] Y. Chen, J. Au, P. Kazlas, A. Ritenour, H. Gates, and M. McCreary. Electronic paper: flexible active-matrix electronic ink display. *Nature*, 136:423, 2003.
- [85] T. J. Plona. Observation of a second bulk compressional wave in a porous medium at ultrasonic frequencies. *Appl. Phys. Lett.*, 36:259, 1980.
- [86] K. M. Ng, H. T. Davis, and L. E. Scriven. Visualization of blob mechanics in flow through porous media. *Chem. Eng. Sci.*, 33:1009, 1978.
- [87] R. J. Mannheimer and C. J. Oswald. Development of transparent porous media with permeabilities and porosities comparable to soils, aquifers, and petroleum reservoirs. *Ground Water*, 31:781, 1993.
- [88] M. Stohr, K. Roth, and B. Jahne. Measurement of 3D pore-scale flow in index-matched porous media. *Exp. in Fluids*, 35:159, 2003.
- [89] P. Sharma, P. Aswathi, A. Sane, S. Ghosh, and S. Bhattacharya. Three-dimensional real-time imaging of bi-phasic flow through porous media. *Rev. Sci. Instrum.*, 82:113704, 2011.
- [90] T. Walmann. Visualization of transport phenomena in three-dimensional porous media. Master's thesis, University of Oslo, 1992.
- [91] V. Frette, J. Feder, T. Jossang, P. Meakin, and K. J. Maloy. Fast, immiscible fluid-fluid displacement in three-dimensional porous media at finite viscosity contrast. *Phys. Rev. E*, 50:2881, 1994.

Bibliography

- [92] W. C. Lyons. *Standard Handbook of Petroleum and Natural Gas Engineering*. Gulf Professional Publishing, Oxford, 1996.
- [93] Y. Gueguen and V. Palciauskas. *Introduction to the Physics of Rocks*. Princeton, Princeton, 1994.
- [94] A. P. Philipse and C. Pathmamanoharan. Liquid permeation (and sedimentation) of dense colloidal hard-sphere packings. *J. Coll. Int. Sci.*, 159:96, 1993.
- [95] A. T. Krummel, S. S. Datta, S. Munster, and D. A. Weitz. Visualizing multiphase flow and trapped fluid configurations in a model three-dimensional porous medium. *AIChE J.*, 59:1022, 2013.
- [96] P. G. Toledo, L. E. Scriven, and H. T. Davis. Equilibrium and stability of static interfaces in biconical pore segments. *SPE Form. Eval.*, 9:46, 1994.
- [97] G. Mason and N. Morrow. Meniscus displacement curvatures of a perfectly wetting liquid in capillary pore throats formed by spheres. *J. Coll. Int. Sci.*, 109:46, 1986.
- [98] R. Lenormand and C. Zarcone. Invasion percolation in an etched network: measurement of a fractal dimension. *Phys. Rev. Lett.*, 54:2229, 1985.
- [99] K. J. Maloy, L. Furuberg, J. Feder, and T. Jossang. Gravity invasion percolation in two dimensions: experiment and simulation. *Phys. Rev. Lett.*, 68:2161, 1992.
- [100] N. Martys, M. Cieplak, and M. O. Robbins. Critical phenomena in fluid invasion of porous media. *Phys. Rev. Lett.*, 66:1058, 1991.
- [101] B. Xu, Y. C. Yortsos, and D. Salin. Invasion percolation with viscous forces. *Phys. Rev. E*, 57:739, 1998.
- [102] L. Xu, S. Davis, A. B. Schofield, and D. A. Weitz. Dynamics of drying in 3D porous media. *Phys. Rev. Lett.*, 101:094502, 2008.
- [103] W. E. Galloway and D. K. Hobday. *Terrigenous clastic depositional systems: applications to fossil fuel and groundwater resources*. Springer, New York, 1996.
- [104] S. E. Gasda and M. A. Celia. Upscaling relative permeabilities in a structured porous medium. *Adv. Water Resour.*, 28:493, 2004.
- [105] H. Hoteit and A. Firoozabadi. Numerical modeling of two-phase flow in heterogeneous permeable media with different capillarity pressures. *Adv. Water Resour.*, 31:56, 2008.
- [106] B. H. Keuper and E. O. Frind. Two-phase flow in heterogeneous porous media: 1. Model development. *Water Resour. Res.*, 27:1049, 1991.

Bibliography

- [107] G. F. Pinder and W. G. Gray. *Essentials of multiphase flow and transport in porous media*. Wiley, 2008.
- [108] N. Shokri, P. Lehmann, and D. Or. Evaporation from layered porous media. *J. Geophys. Res.*, 115:B06204, 2010.
- [109] J. A. Neufeld and H. E. Huppert. Modelling carbon dioxide sequestration in layered strata. *J. Fluid Mech.*, 625:353, 2009.
- [110] H. M. Selim and L. Ma. *Physical nonequilibrium in soils: modeling and application*. Ann Arbor Press, Chelsea, 1998.
- [111] M. Romano, M. Chabert, A. Cuenca, and H. Bodiguel. Strong influence of geometrical heterogeneity on drainage in porous media. *Phys. Rev. E*, 84:065302, 2011.
- [112] K. K. Mohanty, H. T. Davis, and L. E. Scriven. Physics of oil entrapment in water-wet rock. *SPE Reservoir Engineering*, 2:113, 1987.
- [113] R. Al Raoush. *Extraction of physically-realistic pore network properties from three-dimensional synchrotron microtomography images of unconsolidated porous media*. PhD thesis, Louisiana State University, 2002.
- [114] K. E. Thompson, C. S. Willson, C. D. White, S. Nyman, J. Bhattacharya, and A. H. Reed. Application of a new grain-based reconstruction algorithm to microtomography images for quantitative characterization and flow modeling. *SPE*, 95887, 2005.
- [115] J. P. Stokes, D. A. Weitz, J. P. Gollub, A. Dougherty, M. O. Robbins, P. M. Chaikin, and H. M. Lindsay. Interfacial stability of immiscible displacement in a porous medium. *Phys. Rev. Lett.*, 57:1718, 1986.
- [116] T. S. Ramakrishnan and D. T. Wasan. Two-phase distribution in porous media: An application of percolation theory. *Int. J. Multiphase Flow*, 12:357, 1986.
- [117] C. E. Diaz, I. Chatzis, and F. A. L. Dullien. Simulation of capillary pressure curves using bond correlated site percolation on a simple cubic network. *Transp. Porous Media*, 2:215, 1987.
- [118] M. J. Blunt, M. J. King, and H. Scher. Simulation and theory of two-phase flow in porous media. *Phys. Rev. A*, 46:7680, 1992.
- [119] M. J. Blunt. Pore level modeling of the effects of wettability. *SPE J.*, 2:70, 1997.
- [120] M. J. Blunt. Physically-based network modeling of multiphase flow in intermediate-wet porous media. *J. Pet. Sci. Eng.*, 20:117, 1998.
- [121] K. Mogensen and E. H. Stenby. A dynamic two-phase pore-scale model of imbibition. *Transp. Porous Media*, 32:299, 1998.

Bibliography

- [122] P. E. Oren, S. Bakke, and O. J. Arntzen. Extending predictive capabilities to network models. *SPE J.*, 3:324, 1998.
- [123] G. N. Constantinides and A. Payatakes. Effects of precursor wetting films in immiscible displacement through porous media. *Transp. Porous Media*, 38:291, 2000.
- [124] R. G. Hughes and M. J. Blunt. Pore scale modeling of rate effects in imbibition. *Transp. Porous Media*, 40:295, 2000.
- [125] T. W. Patzek. Verification of a complete pore network simulator of drainage and imbibition. *SPE J.*, 6:144, 2001.
- [126] N. A. Idowu and M. J. Blunt. Pore-scale modeling of rate effects in water-flooding. *Transp. Porous Media*, 83:151, 2010.
- [127] L. Furuberg, K. J. Maloy, and J. Feder. Intermittent behavior in slow drainage. *Phys. Rev. E*, 53:966, 1996.
- [128] F. Moebius and D. Or. Interfacial jumps and pressure bursts during fluid displacement in interacting irregular capillaries. *J. Coll. Int. Sci.*, 377:406, 2012.
- [129] M. Ferer, G. S. Bromhal, and D. H. Smith. Pore-level modeling of drainage: crossover from invasion percolation fingering to compact flow. *Phys. Rev. E*, 67:051601, 2003.
- [130] M. S. Al Gharbi and M. J. Blunt. Dynamic network modeling of two-phase drainage in porous media. *Phys. Rev. E*, 71:016308, 2005.
- [131] T. C. Ransohoff, P. A. Gauglitz, and C. J. Radke. Snap-off of gas bubbles in smoothly constricted noncircular capillaries. *AICHE J.*, 33:753, 1987.
- [132] T. C. Tsakiroglou and A. C. Payatakes. Mercury intrusion and retraction in model porous media. *Adv. Coll. Int. Sci.*, 75:215, 1998.
- [133] G. J. Hirasaki. *Interfacial Phenomena in Petroleum Recovery*. Marcel Dekker, 1991.
- [134] S. G. Huling and J. W. Weaver. Dense nonaqueous phase liquids. *Dense Nonaqueous Phase Liquids; EPA Ground Water Issue*, EPA/540/4-91-002 US Environmental Protection Agency, Ada, OK, 1991.
- [135] S. L. Bryant, P. R. King, and D. W. Mellor. Network model evaluation of permeability and spatial correlation in a real random sphere packing. *Transp. Porous Media*, 11:53, 1993.
- [136] Y. Meheust, G. Lovoll, K. J. Maloy, and J. Schmittbuhl. Interface scaling in a two-dimensional porous medium under combined viscous, gravity, and capillary effects. *Phys. Rev. E*, 66:051603, 2002.

Bibliography

- [137] N. El Khatib. The effect of crossflow on waterflooding of stratified reservoirs. *SPE J.*, 25:291, 1985.
- [138] J. T. Birkholzer, Q. Zhou, and C. F. Tsang. Large-scale impact of CO₂ storage in deep saline aquifers: A sensitivity study on pressure response in stratified systems. *Int. J. Greenhouse Gas Control*, 3:181, 2009.
- [139] H. J. Bertin, O. G. Apaydin, L. M. Castanier, and A. R. Kovscek. Foam flow in heterogeneous porous media: Effect of cross flow. *SPE J.*, 4:75, 1999.
- [140] Y. Huang, P. S. Ringrose, and K. S. Sorbie. Capillary trapping mechanisms in water-wet laminated rocks. *SPE Reservoir Engineering*, 10:287, 1995.
- [141] L. Chaudhari, N. Hadia, S. K. Mitra, and M. Vinjamur. Experimental investigation of use of horizontal wells in waterflooding. *Energy Sources*, 33:948, 2011.
- [142] J. Bear and A. H. D. Cheng. *Modeling Groundwater Flow and Contaminant Transport*. Springer, 2010.
- [143] H. E. Dawson and P. V. Roberts. Influence of viscous, gravitational, and capillary forces on dnapl saturation. *Ground Water*, 35:261, 1997.
- [144] E. Saadatpoor, S. L. Bryant, and K. Sepehrnoori. New trapping mechanism in carbon sequestration. *Transp. Porous Media*, 82:3, 2010.
- [145] J. J. Tabor. Dynamic and static forces required to remove a discontinuous oil phase from porous media containing both oil and water. *Soc. Pet. Eng. J.*, 9:3, 1969.
- [146] G. L. Stegemeier. *Improved oil recovery by surfactant and polymer flooding*. Academic Press, 1977.
- [147] I. Chatzis, M. S. Kuntamukkula, and N. R. Morrow. Blob-size distribution as a function of capillary number in sandstones. *SPE Annual Technical Conference and Exhibition*, pages SPE-13213, 1984.
- [148] N. R. Morrow. Measurement and correlation of conditions for entrapment and mobilization of residual oil. *United States Department of Energy, Final Report*, pages DOE/BC/10310-38, 1984.
- [149] N. R. Morrow, I. Chatzis, and J. J. Taber. Entrapment and mobilization of residual oil in bead packs. *SPE Reservoir Engineering*, 3:927, 1988.
- [150] A. C. Payatakes, K. M. Ng, and R. W. Flummerfelt. Oil ganglia dynamics during immiscible displacement. model formulation. *AICHE J.*, 26:430, 1980.
- [151] N. C. Wardlaw and M. Mckellar. Oil blob populations and mobilization of trapped oil in unconsolidated packs. *Can. Soc. Chem. Eng.*, 63:525, 1985.

Bibliography

- [152] R. G. Larson, L. E. Scriven, and H. T. Davis. Percolation theory of residual phases in porous media. *Nature*, 268:409, 1977.
- [153] K. M. Ng and A. C. Payatakes. Stochastic simulation of the mobilization, breakup and stranding of oil ganglia in water-wet granular porous media during immiscible displacement. *AICHE J.*, 26:419, 1980.
- [154] R. G. Larson, H. T. Davis, and L. E. Scriven. Displacement of residual non-wetting fluid from porous media. *Chem. Eng. Sci.*, 36:75, 1981.
- [155] P. T. Imhoff, P. R. Jaffe, and G. F. Pinder. An experimental study of complete dissolution of a nonaqueous phase liquid in saturated porous media. *Water Resour. Res.*, 30:307, 1994.
- [156] N. A. Sahloul, M. A. Ioannidis, and I. Chatzis. Dissolution of residual non-aqueous phase liquids in porous media: pore-scale mechanisms and mass transfer rates. *Adv. Water Resour.*, 25:33, 2002.
- [157] L. Yu and N. C. Wardlaw. The influence of wettability and critical pore-throat size ratio on snap-off. *J. Coll. Int. Sci.*, 109:461, 1986.
- [158] J. G. Roof. Snap-off of oil droplets in water-wet pores. *Soc. Pet. Eng. J.*, 10:85, 1970.
- [159] V. H. Nguyen, A. P. Sheppard, M. A. Knackstedt, and V. W. Pinczewski. The effect of displacement rate on imbibition relative permeability and residual saturation. *J. Pet. Sci. Eng.*, 52:54, 2006.
- [160] A. Setiawan, H. Nomura, and T. Suekane. Microtomography of imbibition phenomena and trapping mechanism. *Transp. Porous Media*, 92:243, 2012.
- [161] D. S. Gaunt. Percolation exponent for lattice dimensionality $d \geq 3$. *J. Phys. A: Math. Gen.*, 10:807, 1977.
- [162] J. Hoshen, D. Stauffer, G. H. Bishop, R. J. Harrison, and G. D. Quinn. Monte Carlo experiments on cluster size distribution in percolation. *J. Phys. A: Math. Gen.*, 12:1285, 1979.
- [163] D. Stauffer. Scaling theory of percolation clusters. *Phys. Rep.*, 54:1, 1979.
- [164] S. Iglesias, M. A. Ferno, P. Shearing, and M. J. Blunt. Comparison of residual oil cluster size distribution, morphology and saturation in oil-wet and water-wet sandstone. *J. Coll. Int. Sci.*, 375:187, 2012.
- [165] D. Wilkinson. Percolation model of immiscible displacement in the presence of buoyancy forces. *Phys. Rev. A*, 30:520, 1984.

Bibliography

- [166] I. I. Gardesu. Behavior of gas bubbles in capillary spaces. *Trans. AIME*, 86:351, 1930.
- [167] T. S. Ramakrishnan and D. T. Wasan. Effect of capillary number on the relative permeability function for two-phase flow in porous media. *Powder Technol.*, 48:99, 1986.
- [168] T. S. Ramakrishnan. *Application of fractional flow theory to high pH flooding*. PhD thesis, IIT Chicago, 1985.
- [169] M. Tyagi and P. Jenny. Probability density function approach for modelling multi-phase flow with ganglia in porous media. *J. Fluid Mech.*, 688:219, 2011.
- [170] S. Saleh, J. F. Thovert, and P. M. Adler. Measurement of two-dimensional velocity fields in porous media by particle image displacement velocimetry. *Exp. in Fluids*, 12:210–212, 1992.
- [171] S. Saleh, J. F. Thovert, and P. M. Adler. Flow along porous media by particle image velocimetry. *AICHE J.*, 39:1765–1776, 1993.
- [172] A. Cenedese and P. Viotti. Lagrangian analysis of nonreactive pollutant dispersion in porous media by means of the particle image velocimetry technique. *Water Resour. Res.*, 48:13–21, 1993.
- [173] M. A. Northrup, T. J. Kulp, S. M. Angel, and G. F. Pinder. Direct measurement of interstitial velocity field variations in a porous medium using fluorescent-particle image velocimetry. *Chem. Eng. Sci.*, 48:13–21, 1993.
- [174] M. Rashidi, L. Peurrung, A. F. B. Tompson, and T. J. Kulp. Experimental analysis of pore-scale flow and transport in porous media. *Adv. Water Resour.*, 19:163–180, 1996.
- [175] M. Moroni and J. H. Cushman. Statistical mechanics with three-dimensional particle tracking velocimetry experiments in the study of anomalous dispersion. II. Experiments. *Phys. Fluids*, 13:81–91, 2001.
- [176] M. Moroni and J. H. Cushman. Three-dimensional particle tracking velocimetry studies of the transition from pore dispersion to Fickian dispersion for homogeneous porous media. *Water Resour. Res.*, 37:873–884, 2001.
- [177] A. Lachhab, Y. K. Zhang, and M. V. I. Muste. Particle tracking experiments in match-index- refraction porous media. *Ground Water*, 46:865–872, 2008.
- [178] A. Y. L. Huang, M. F. Y. Huang, H. Capart, and R. H. Chen. Optical measurements of pore geometry and fluid velocity in a bed of irregularly packed spheres. *Exp. in Fluids*, 45:309–321, 2008.

Bibliography

- [179] Y. A. Hassan and E. E. Dominguez-Ontiveros. Flow visualization in a pebble bed reactor experiment using PIV and refractive index matching techniques. *Nuclear Engineering and Design*, 238:3080–3085, 2008.
- [180] J. K. Arthur, D. W. Ruth, and M. F. Tachie. PIV measurements of flow through a model porous medium with varying boundary conditions. *J. Fluid Mech.*, 629:343–374, 2009.
- [181] D. Sen, D. S. Nobes, and S. K. Mitra. Optical measurement of pore scale velocity field inside microporous media. *Microfluid. Nanofluid.*, 12:189–200, 2012.
- [182] M. D. Shattuck, R. P. Behringer, G. A. Johnson, and J. G. Georgiadis. Convection and flow in porous media. Part 1. Visualization by magnetic resonance imaging. *J. Fluid Mech.*, 332:215–245, 1996.
- [183] Y. E. Kutsovsky, L. E. Scriven, H. T. Davis, and B. E. Hammer. NMR imaging of velocity profiles and velocity distributions in bead packs. *Phys. Fluids*, 8:863–871, 1996.
- [184] A. J. Sederman, M. L. Johns, A. S. Bramley, P. Alexander, and L. F. Gladden. Magnetic resonance imaging of liquid flow and pore structure within packed beds. *Chem. Eng. Sci.*, 52:2239–2250, 1997.
- [185] A. J. Sederman and L. F. Gladden. Magnetic resonance visualisation of single- and two-phase flow in porous media. *Magn. Reson. Imag.*, 19:339–343, 2001.
- [186] B. Bijeljic, A. Raeini, P. Mostaghimi, and M. J. Blunt. Predictions of non-Fickian solute transport in different classes of porous media using direct simulation on pore-scale images. *Phys. Rev. E*, 87:013011, 2013.
- [187] C. Fleurant and J. van der Lee. A stochastic model of transport in three-dimensional porous media. *Mathematical Geology*, 33:449, 2001.
- [188] B. Audoly, P. N. Sen, S. Ryu, and Y. Q. Song. Correlation functions for inhomogeneous magnetic field in random media with application to a dense random pack of spheres. *J. Magn. Reson.*, 164:154, 2003.
- [189] T. A. Angelini, E. Hannezo, X. Trepat, J. J. Fredberg, and D. A. Weitz. Cell migration driven by cooperative substrate deformation patterns. *Phys. Rev. Lett.*, 104:168104, 2010.
- [190] P. N. Segre, E. Herbolzheimer, and P. M. Chaikin. Long-range correlations in sedimentation. *Phys. Rev. Lett.*, 79:2574, 1997.

Bibliography

- [191] P. de Anna, T. Le Borgne, M. Dentz, A. M. Tartakovsky, D. Bolster, and P. Davy. Flow intermittency, dispersion, and correlated continuous time random walks in porous media. *Phys. Rev. Lett.*, 110:184592, 2013.
- [192] D. R. Nelson and F. Spaepen. *Solid State Physics*. Academic Press, 1989.
- [193] D. L. Johnson, T. J. Plona, C. Scala, F. Pasierb, and H. Kojima. Tortuosity and acoustic slow waves. *Phys. Rev. Lett.*, 49:1840–1844, 1982.
- [194] E. Charlaix, A. P. Kushnick, and J. P. Stokes. Experimental study of dynamic permeability in porous media. *Phys. Rev. Lett.*, 61:1595–1598, 1988.
- [195] R. W. Mair, G. P. Wong, D. Hoffmann, M. D. Hurlimann, S. Patz, L. M. Schwartz, and R. L. Walsworth. Probing porous media with gas diffusion NMR. *Phys. Rev. Lett.*, 83:3324–3327, 1999.
- [196] B. Manz, L. F. Gladden, and P. B. Warren. Flow and dispersion in porous media: Lattice-Boltzmann and NMR studies. *AIChE J.*, 45:1845–1854, 1999.
- [197] C. J. Davies, J. D. Griffith, A. J. Sederman, L. F. Gladden, and M. L. Johns. Rapid surface-to-volume ratio and tortuosity measurement using difftrain. *J. Magn. Reson.*, 187:170–175, 2007.
- [198] E. Charlaix and H. Gayvallet. Hydrodynamic dispersion in networks of capillaries of random permeability. *EPL*, 16:259–264, 1991.
- [199] P. N. Sen, L. M. Schwartz, P. P. Mitra, and B. I. Halperin. Surface relaxation and the long-time diffusion coefficient in porous media: Periodic geometries. *Phys. Rev. B*, 49:215–225, 1994.
- [200] I. Okamoto, S. Hirai, and K. Ogawa. MRI velocity measurements of water flow in porous media containing a stagnant immiscible liquid. *Meas. Sci. Technol.*, 12:1465–1472, 2001.
- [201] P. G. De Gennes. Hydrodynamic dispersion in unsaturated porous media. *J. Fluid Mech.*, 136:189–200, 1983.
- [202] N. T. Burdine. Relative permeability calculations from pore size distribution data. *Trans. AIME*, 198:71–77, 1952.
- [203] L. A. Richards. Capillary conduction of liquids through porous mediums. *Physics*, 1:318, 1931.
- [204] M. C. Leverett. Capillary behavior in porous solids. *Trans. AIME*, 142:152, 1941.
- [205] M. Honarpour, L. Koederitz, and A. H. Harvey. *Relative permeability of petroleum reservoirs*. CRC Press, 1986.

Bibliography

- [206] D. G. Avraam and A. C. Payatakes. Flow regimes and relative permeabilities during steady-state two-phase flow in porous media. *J. Fluid Mech.*, 293:207, 1995.
- [207] K. T. Tallakstad, H. A. Knudsen, T. Ramstad, G. Lovoll, K. J. Maloy, R. Toussaint, and E. G. Flekkoy. Steady-state two-phase flow in porous media: statistics and transport properties. *Phys. Rev. Lett.*, 102:074502, 2009.
- [208] C. M. Elsik and C. A. Miller. *Surfactant-Based Mobility Control*. ACS Symposium Series, 1988.
- [209] A. Chatenever and J. C. Calhoun. Visual examinations of fluid behavior in porous media - part i. *Pet. Trans. AIME*, 195:149, 1952.
- [210] E. Amstad, S. S. Datta, and D. A. Weitz. The microfluidic arrayed-post device: high throughput production of viscous single drops. *submitted*, 2013.
- [211] A. S. Utada, A. Fernandez-Nieves, H. A. Stone, and D. A. Weitz. Dripping to jetting transitions in coflowing liquid streams. *Phys. Rev. Lett.*, 99:094502, 2007.
- [212] R. F. Meyer and J. C. Crocker. Universal dripping and jetting in a transverse shear flow. *Phys. Rev. Lett.*, 102:194501, 2009.
- [213] A. S. Utada, A. Fernandez-Nieves, J. M. Gordillo, and D. A. Weitz. Absolute instability of a liquid jet in a coflowing stream. *Phys. Rev. Lett.*, 100:014502, 2008.
- [214] S. Protiere, M. Z. Bazant, D. A. Weitz, and H. A. Stone. Droplet breakup in flow past an obstacle: A capillary instability due to permeability variations. *EPL*, 92:54002, 2010.
- [215] L. Salkin, L. Courbin, and P. Panizza. Microfluidic breakups of confined droplets against a linear obstacle: The importance of the viscosity contrast. *Phys. Rev. E*, 86:036317, 2012.
- [216] S. S. Datta, H. Chiang, T. S. Ramakrishnan, and D. A. Weitz. Spatial fluctuations of fluid velocities in flow through a three-dimensional porous medium. *Phys. Rev. Lett.*, 111:064501, 2013.
- [217] S. Bryant and M. J. Blunt. Prediction of relative permeability in simple porous media. *Phys. Rev. A*, 46:2004, 1992.
- [218] R. A. Fulcher, T. Ertekin, and C. D. Stahl. Effect of capillary number and its constituents on two-phase relative permeability curves. *J. Petr. Tech.*, 37:249, 1985.
- [219] T. G. Mason, J. Bibette, and D. A. Weitz. Elasticity of compressed emulsions. *Phys. Rev. Lett.*, 75:2051, 1995.

Bibliography

- [220] T. G. Mason, J. Bibette, and D. A. Weitz. Yielding and flow of monodisperse emulsions. *J. Coll. Int. Sci.*, 179:439, 1996.
- [221] H. M. Wyss, K. Miyazaki, J. Mattsson, Z. Hu, D. R. Reichman, and D. A. Weitz. Strain-rate frequency superposition: A rheological probe of structural relaxation in soft materials. *Phys. Rev. Lett.*, 98:2383, 2007.
- [222] P. Hebraud, F. Lequex, J. P. Munch, and D. J. Pine. Yielding and rearrangements in disordered emulsions. *Phys. Rev. Lett.*, 78:4657, 1997.
- [223] T. G. Mason, A. H. Krall, J. Bibette, Hu Gang, and D. A. Weitz. *Encyclopedia of Emulsion Technology*, volume 4. Marcell Dekker, New York, 1996.
- [224] P. Poulin, J. Bibette, and D. A. Weitz. From colloidal aggregation to spinodal decomposition in sticky emulsions. *Eur. Phys. J. B*, 7:277, 1999.
- [225] J. Bibette, T. G. Mason, H. Gang, D. A. Weitz, and P. Poulin. Structure of adhesive emulsions. *Langmuir*, 9:3352, 1993.
- [226] T. B. J. Blijdenstein, E. van der Linden, T. van Vliet, and G. A. van Aken. Scaling behavior of delayed demixing, rheology, and microstructure of emulsions flocculated by depletion and bridging. *Langmuir*, 20:1132, 2004.
- [227] L. Becu, S. Manneville, and A. Colin. Yielding and flow in adhesive and nonadhesive concentrated emulsions. *Phys. Rev. Lett.*, 96:1383, 2006.
- [228] P. Alexandridis and B. Lindman. *Amphiphilic Block Copolymers: Self-Assembly and Applications*. Elsevier, Amsterdam, 2000.
- [229] L. Yang and P. Alexandridis. Sans investigation of the temperature dependent aggregation behavior of the block copolymer Pluronic L64 in aqueous solution. *Langmuir*, 16:4819, 2000.
- [230] J. Bibette, D. Roux, and F. Nallet. Depletion interactions and fluid-solid equilibrium in emulsions. *Phys. Rev. Lett.*, 65:2470, 1990.
- [231] A. Vrij. Polymers at interfaces and the interactions in colloidal dispersions. *Pure Appl. Chem.*, 48:471, 1976.
- [232] G. Andersson, E. Carey, and C. Stubenrauch. Disjoining pressure study of formamide foam films stabilized by surfactants. *Langmuir*, 26:7752, 2010.
- [233] A. Imhof and D. J. Pine. Stability of nonaqueous emulsions. *J. Coll. Int. Sci.*, 192:368, 1997.
- [234] A. J. C. Ladd. Hydrodynamic transport coefficients of random dispersions of hard spheres. *J. Phys. Chem.*, 93:3484, 1990.

Bibliography

- [235] P. G. de Gennes. Polymers at an interface; a simplified view. *Adv. Coll. Int. Sci.*, 27:189, 1987.
- [236] T. G. Mason, M. D. Lacasse, G. S. Grest, D. Levine, J. Bibette, and D. A. Weitz. Osmotic pressure and viscoelastic shear moduli of concentrated emulsions. *Phys. Rev. E*, 56:3150, 1997.
- [237] R. S. Farr and R. D. Groot. Close packing density of polydisperse hard spheres. *J. Chem. Phys.*, 131:2441, 2009.
- [238] W. H. Shih, W. Y. Shih, S. I. Kim, J. Liu, and I. A. Aksay. Scaling behavior of the elastic properties of colloidal gels. *Phys. Rev. A*, 42:4772, 1990.
- [239] A. Zaccone, H. Wu, and E. Del Gado. Elasticity of arrested short-ranged attractive colloids: Homogeneous and heterogeneous glasses. *Phys. Rev. Lett.*, 103:2083, 2009.
- [240] M. Laurati, G. Petekidis, N. Koumakis, F. Cardinaux, A. B. Schofield, J. M. Brader, M. Fuchs, and S. U. Egelhaaf. Structure, dynamics, and rheology of colloid-polymer mixtures: From liquids to gels. *J. Chem. Phys.*, 130:1349, 2009.
- [241] E. Lerner and I. Procaccia. Locality and nonlocality in elastoplastic responses of amorphous solids. *Phys. Rev. E*, 80:026128, 2009.
- [242] J. Sprakel, S. B. Lindstrom, T. E. Kodger, and D. A. Weitz. Stress enhancement in the delayed yielding of colloidal gels. *Phys. Rev. Lett.*, 106:248303, 2011.
- [243] K. N. Pham, G. Petekidis, D. Vlassopoulos, S. U Egelhaaf, W. C. K. Poon, and P. N. Pusey. Yielding behavior of repulsion-and attraction-dominated colloidal glasses. *J. Rheol.*, 52:649, 2008.
- [244] S. Simovic, P. Heard, H. Hui, Y. Song, F. Peddie, A. Davey, A. Lewis, T. Rades, and C. A. Prestidge. Dry hybrid lipid silica microcapsules engineered from submicron lipid droplets and nanoparticles as a novel delivery system for poorly soluble drugs. *Molecular Pharmaceutics*, 6:861, 2009.
- [245] A. R. Studart, U. T. Gonzenbach, I. Akartuna, E. Tervoort, and L. J. Gauckler. Materials from foams and emulsions stabilized by colloidal particles. *J. Mater. Chem.*, 17:3283, 2007.
- [246] A. Cervantes Martinez, E. Rio, G. Delon, A. Saint-Jalmes, D. Langevin, and B. P. Binks. On the origin of the remarkable stability of aqueous foams stabilised by nanoparticles: link with microscopic surface properties. *Soft Matter*, 4:1531, 2008.
- [247] D. Georgieva, V. Schmitt, F. Leal-Calderon, and D. Langevin. On the possible role of surface elasticity in emulsion stability. *Langmuir*, 25:5565, 2009.

Bibliography

- [248] P. A. Kralchevsky and K. Nagayama. *Particles at Fluid Interfaces and Membranes*. Elsevier Science, 2001.
- [249] D. Vella, P. Aussillous, and L. Mahadevan. Elasticity of an interfacial particle raft. *EPL*, 68:212, 2004.
- [250] K. Stratford, R. Adhikari, I. Pagonabarraga, J. C. Desplat, and M. E. Cates. Colloidal jamming at interfaces: A route to fluid-bicontinuous gels. *Science*, 309:2198, 2005.
- [251] S. Arditty, V. Schmitt, F. Lequeux, and F. Leal-Calderon. Interfacial properties in solid-stabilized emulsions. *Eur. Phys. J. B*, 44:381, 2005.
- [252] B. Madivala, S. Vandebril, J. Fransaer, and J. Vermant. Exploiting particle shape in solid stabilized emulsions. *Soft Matter*, 5:1717, 2009.
- [253] R. Aveyard, J. H. Clint, D. Nees, and V. N. Paunov. Compression and structure of monolayers of charged latex particles at air/water and octane/water interfaces. *Langmuir*, 16:1969, 2000.
- [254] R. Aveyard, J. H. Clint, D. Nees, and N. Quirke. Structure and collapse of particle monolayers under lateral pressure at the octane/aqueous surfactant solution interface. *Langmuir*, 16:8820, 2000.
- [255] D. Zang, D. Langevin, B. P. Binks, and B. Wei. Shearing particle monolayers: Strain-rate frequency superposition. *Phys. Rev. E*, 81:011604, 2010.
- [256] P. Cicuta, E. J. Stancik, and G. G. Fuller. Shearing or compressing a soft glass in 2D: time-concentration superposition. *Phys. Rev. Lett.*, 90:236101, 2003.
- [257] T. A. Witten. Stress focusing in elastic sheets. *Rev. Mod. Phys.*, 79:643, 2007.
- [258] C. Quilliet, C. Zoldesi, C. Riera, A. van Blaaderen, and A. Imhof. Anisotropic colloids through non-trivial buckling. *Eur. Phys. J. E*, 27:13, 2008.
- [259] N. Tsapis, E. R. Dufresne, S. S. Sinha, C. S. Riera, J. W. Hutchinson, L. Mahadevan, and D. A. Weitz. Onset of buckling in drying droplets of colloidal suspensions. *Phys. Rev. Lett.*, 94:018302, 2005.
- [260] P. J. Colver, T. Chen, and S. A. F. Bon. Supracolloidal structures through liquidliquid interface driven assembly and polymerization. *Macromol. Symp.*, 245:34, 2006.
- [261] A. R. Studart, H. C. Shum, and D. A. Weitz. Arrested coalescence of particle-coated droplets into nonspherical supracolloidal structures. *J. Phys. Chem. B*, 113:3914, 2009.

Bibliography

- [262] C. Gao, E. Donath, S. Moya, V. Dudnik, and H. Mohwald. Elasticity of hollow polyelectrolyte capsules prepared by the layer-by-layer technique. *Eur. Phys. J. E*, 5:21, 2000.
- [263] H. C. Shum, J. W. Kim, and D. A. Weitz. Microfluidic fabrication of monodisperse biocompatible and biodegradable polymersomes with controlled permeability. *J. Am. Chem. Soc.*, 130:9543–9549, 2008.
- [264] H. Xu, S. Melle, K. Golemanov, and G. Fuller. Shape and buckling transitions in solid-stabilized drops. *Langmuir*, 21:10016, 2005.
- [265] B. P. Binks. Particles as surfactants – similarities and differences. *Curr. Opin. Colloid Interface Sci.*, 7:21, 2002.
- [266] P. Pieranski. Two-dimensional interfacial colloidal crystals. *Phys. Rev. Lett.*, 45:569, 1980.
- [267] R. M. Wiley. Limited coalescence of oil droplets in coarse oil-in-water emulsions. *J. Coll. Sci.*, 9:427, 1954.
- [268] S. O. Asekomhe, R. Chiang, J. H. Masliyah, and J. A. W. Elliott. Some observations on the contraction behavior of a water-in-oil drop with attached solids. *Ind. Eng. Chem. Res.*, 44:1241, 2005.
- [269] S. R. Raghavan, J. Hou, G. L. Baker, and S. A. Khan. Colloidal interactions between particles with tethered nonpolar chains dispersed in polar media: direct correlation between dynamic rheology and interaction parameters. *Langmuir*, 16:1066, 2000.
- [270] M. Berhanu and A. Kudrolli. Heterogeneous structure of granular aggregates with capillary interactions. *Phys. Rev. Lett.*, 105:098002, 2010.
- [271] A.R. Bausch, M.J. Bowick, A. Cacciuto, A.D. Dinsmore, M.F. Hsu, D.R. Nelson, M.G. Nikolaides, A. Travesset, and D. A. Weitz. Grain boundary scars and spherical crystallography. *Science*, 299:1716, 2003.
- [272] S. Fortuna, C. A. L. Colard, A. Troisi, and S. A. F. Bon. Packing patterns of silica nanoparticles on surfaces of armored polystyrene latex particles. *Langmuir*, 25:12399, 2009.
- [273] J. H. Jellett. On the properties of inextensible surfaces. *Trans. R. Irish Acad.*, 22:343, 1855.
- [274] A. V. Pogorelov. *Bendings of Surfaces and Stability of Shells*. AMS Bookstore, Providence RI, 1988.

Bibliography

- [275] C. Monteux, J. Kirkwood, H. Xu, E. Jung, and G. G. Fuller. Determining the mechanical response of particle-laden fluid interfaces using surface pressure isotherms and bulk pressure measurements of droplets. *Phys. Chem. Chem. Phys.*, 9:6344, 2007.
- [276] B. D. Leahy, L. Pocivavsek, M. Meron, K. L. Lam, D. Salas, P. J. Viccaro, K. Y. C. Lee, and B. Lin. Geometric stability and elastic response of a supported nanoparticle film. *Phys. Rev. Lett.*, 105:058301, 2010.
- [277] A. B. Subramaniam, M. Abkarian, L. Mahadevan, and H. A. Stone. Colloid science: Non-spherical bubbles. *Nature*, 438:930, 2005.
- [278] J. Lidmar, L. Mirny, and D. R. Nelson. Virus shapes and buckling transitions in spherical shells. *Phys. Rev. E*, 68:051910, 2003.
- [279] J. W. Hutchinson. Imperfection sensitivity of externally pressurized spherical shells. *J. Appl. Mech.*, 34:49, 1967.
- [280] P. S. Clegg, E. M. Herzig, A. B. Schofield, S. U. Egelhaaf, T. S. Horozov, B. P. Binks, M. E. Cates, and W. C. K. Poon. Emulsification of partially miscible liquids using colloidal particles: Nonspherical and extended domain structures. *Langmuir*, 23:5984, 2007.
- [281] H. L. Cheng and S. S. Velankar. Controlled jamming of particle-laden interfaces using a spinning drop tensiometer. *Langmuir*, 25:4412, 2009.
- [282] S. R. Keller and R. Skalak. Motion of a tank-treading ellipsoidal particle in a shear flow. *J. Fluid Mech.*, 120:27, 1982.
- [283] A. Vaziri and L. Mahadevan. Localized and extended deformations of elastic shells. *Proc. Natl. Acad. Sci.*, 105:7913, 2008.
- [284] D. L. Blair and A. Kudrolli. Geometry of crumpled paper. *Phys. Rev. Lett.*, 94:166107, 2005.
- [285] E. Katifori, S. Alben, E. Cerda, D. R. Nelson, and J. Dumais. Foldable structures and the natural design of pollen grains. *Proc. Natl. Acad. Sci.*, 107:7635, 2010.
- [286] T. Mora and A. Boudaoud. Thin elastic plates: On the core of developable cones. *EPL*, 59:41, 2002.
- [287] S. Chaieb and F. Melo. Experimental study of crease formation in an axially compressed sheet. *Phys. Rev. E*, 56:4736, 1997.
- [288] A. M. A. van der Heijden. *W. T. Koiter's Elastic Stability of Solids and Structures*. Cambridge University Press, Cambridge, 2009.

Bibliography

- [289] G. A. Vliegenthart and G. Gompper. Forced crumpling of self-avoiding elastic sheets. *New J. Phys.*, 13:045020, 2011.
- [290] S. Knoche and J. Kierfeld. Buckling of spherical capsules. *Phys. Rev. E*, 84:046608, 2011.
- [291] L. Pauchard and S. Rica. Contact and compression of elastic spherical shells: the physics of a ping-pong ball. *Phil. Mag. B*, 78:225, 1998.
- [292] V. Papadopoulos and M. Papadrakakis. The effect of material and thickness variability on the buckling load of shells with random initial imperfections. *Comput. Methods Appl. Mech. Engrg.*, 194:1405, 2005.
- [293] G. Vernizzi, R. Sknepnek, and M. Olvera de la Cruz. Platonic and Archimedean geometries in multicomponent elastic membranes. *Proc. Natl. Acad. Sci.*, 108:4292, 2011.
- [294] M. A. Krenzke and R. M. Charles. The elastic buckling strength of spherical glass shells. *David Taylor Model Basin Report*, 1759, 1963.
- [295] D. Bushnell. Symmetric and nonsymmetric buckling of finitely deformed eccentrically stiffened shells of revolution. *AIAA Journal*, 5:1455, 1967.
- [296] Y. K. Hwang, U. Jeong, and E. C. Cho. Production of uniform-sized polymer core-shell microcapsules by coaxial electrospraying. *Langmuir*, 24:2446, 2008.
- [297] C. J. Park, Y. K. Hwang, D. C. Hyun, and U. Jeong. In situ localization of molecules in crosslinked particles during electrohydrodynamic process: Simple route to produce microcapsules and fibers with controlled release. *Macromol. Rapid Commun.*, 31:1713, 2010.
- [298] L. B. Petrovic, V. J. Sovilj, J. M. Katona, and J. L. Milanovic. Influence of polymer-surfactant interactions on o/w emulsion properties and microcapsule formation. *J. Coll. Int. Sci.*, 342:333, 2010.
- [299] R. Bocanegra, A. G. Gaonkar, A. Barrero, I. G. Loscertales, D. Pechack, and M. Marquez. Production of cocoa butter microcapsules using an electrospray process. *J. Food Sci.*, 70:8, 2005.
- [300] H. Chen, Y. Zhao, Y. Song, and L. Jiang. One-step multicomponent encapsulation by compound-fluidic electrospray. *J. Am. Chem. Soc.*, 130:7800, 2008.
- [301] Y. Fukui, T. Maruyama, Y. Iwamatsu, A. Fujii, T. Tanaka, Y. Ohmukai, and H. Matsuyama. Preparation of monodispersed polyelectrolyte microcapsules with high encapsulation efficiency by an electrospray technique. *Colloids and Surfaces A*, 370:28, 2010.

Bibliography

- [302] F. V. Lamberti, R. A. Evangelista, J. Blysniuk, M. A. Wheatley, and M. V. Sefton. Microencapsulation of mammalian cells in polyacrylates. *Microencapsulation and Artificial Cells*, 7:101, 1985.
- [303] J. R. Hwang and M. V. Sefton. Microencapsulated human hepatoma (HepG2) cells: capsule-to-capsule variations in protein secretion and permeability. *J. Controlled Release*, 49:217, 1997.
- [304] Q. Wen-Tao, Y. Wei-Ting, X. Yu-Bing, and M. Xiaojun. Optimization of *Saccharomyces cerevisiae* culture in alginate–chitosan–alginate microcapsule. *Biochemical Engineering Journal*, 25:151, 2005.
- [305] K. Bouchemal, S. Briancon, E. Perrier, H. Fessi, I. Bonnet, and N. Zydowicz. Synthesis and characterization of polyurethane and poly (ether urethane) nanocapsules using a new technique of interfacial polycondensation combined to spontaneous emulsification. *Int. J. Pharmaceutics*, 269:89, 2004.
- [306] T. Dobashi, F. J. Yeh, Q. C. Ying, K. Ichikawa, and B. Chu. An experimental investigation on the structure of microcapsules. *Langmuir*, 11:4278, 1995.
- [307] T. Dobashi, T. Furukawa, T. Narita, S. Shimofure, K. Ichikawa, and B. Chu. Determination of the swelling ratio of poly(urea-urethane) microcapsules by single-particle light scattering. *Langmuir*, 17:4525, 2001.
- [308] A. Loxley and B. Vincent. Preparation of poly (methylmethacrylate) microcapsules with liquid cores. *J. Coll. Int. Sci.*, 208:49, 1998.
- [309] P. J. Dowding, R. Atkin, B. Vincent, and P. Bouillot. Oil corepolymer shell microcapsules prepared by internal phase separation from emulsion droplets. i. characterization and release rates for microcapsules with polystyrene shells. *Langmuir*, 20:11374, 2004.
- [310] N. G. Balabushevich, O. P. Tiourina, D. V. Volodkin, N. I. Larionova, and G. B. Sukhorukov. Loading the multilayer dextran sulfate/protamine microsized capsules with peroxidase. *Biomacromolecules*, 4:1191, 2003.
- [311] D. Shchukin, T. Shutava, G. Sukhorukov, and Y. M. Lvov. Modified polyelectrolyte microcapsules as smart defense systems. *Chem. Mater.*, 16:3446, 2004.
- [312] K. Akamatsu, W. Chen, Y. Suzuki, T. Ito, A. Nakao, T. Sugawara, R. Kikuchi, and S. Nakao. Preparation of monodisperse chitosan microcapsules with hollow structures using the spg membrane emulsification technique. *Langmuir*, 26:14854, 2010.
- [313] Q. Yuan, R. A. Williams, and S. Biggs. Surfactant selection for accurate size control of microcapsules using membrane emulsification. *Colloids and Surfaces A*, 347:97, 2009.

Bibliography

- [314] A. Fernandez-Nieves, V. Vitelli, A. S. Utada, D. R. Link, M. Marquez, D. R. Nelson, and D. A. Weitz. Novel defect structures in nematic liquid crystal shells. *Phys. Rev. Lett.*, 99:1578, 2007.
- [315] T. H. Lin, W. H. Huang, I. K. Jun, and P. Jiang. Bioinspired assembly of colloidal nanoplatelets by electric field. *Chem. Mater.*, 21:2039, 2009.
- [316] S. H. Kim, S. J. Jeon, and S. M. Yang. Optofluidic encapsulation of crystalline colloidal arrays with spherical membranes. *J. Am. Chem. Soc.*, 130:6040–6046, 2008.
- [317] L. D. Landau and E. M. Lifshitz. *Theory of Elasticity, 3rd ed.* Elsevier, New York, 1986.
- [318] P. G. Kim and H. A. Stone. Dynamics of the formation of antibubbles. *EPL*, 83:5400, 2008.
- [319] D. Vella, A. Ajdari, A. Vaziri, and A. Boudaoud. Wrinkling of pressurized elastic shells. *Phys. Rev. Lett.*, 107:1743, 2011.
- [320] S. Sacanna, W. T. M. Irvine, P. M. Chaikin, and D. J. Pine. Lock and key colloids. *Nature*, 464:575, 2010.
- [321] S. H. Kim, H. Hwang, C. H. Lim, J. W. Shim, and S. M. Yang. Packing of emulsion droplets: Structural and functional motifs for multicored microcapsules. *Adv. Funct. Mater.*, 21:1608, 2011.
- [322] D. Vella, A. Ajdari, A. Vaziri, and A. Boudaoud. The indentation of pressurized elastic shells: from polymeric capsules to yeast cells. *J. R. Soc. Int.*, 9:448, 2011.
- [323] D. A. Fletcher and R. D. Mullin. Cell mechanics and the cytoskeleton. *Nature*, 463:485, 2010.
- [324] W. A. Nash. *Hydrostatically Loaded Structures*. Pergamon, 1995.
- [325] P. T. Pederson and J. J. Jensen. Buckling behaviour of imperfect spherical shells subjected to different load conditions. *Thin-Walled Structures*, 23:41, 1995.
- [326] P. Kearey and F. J. Vine. *Global Tectonics*. Blackwell, Oxford, 1996.
- [327] D. N. Pinder. Shape of human red cells. *J. Theor. Biol.*, 34:407, 1972.
- [328] M. A. Greenfield, L. C. Palmer, G. Vernizzi, M. Olvera de la Cruz, and S. I. Stupp. Buckled membranes in mixed-valence ionic amphiphile vesicles. *J. Am. Chem. Soc.*, 131:1203, 2009.

Bibliography

- [329] A. Touhami, B. Nysten, and Y. F. Dufresne. Nanoscale mapping of the elasticity of microbial cells by atomic force microscopy. *Langmuir*, 19:4539, 2003.
- [330] F. Julicher and R. Lipowsky. Domain-induced budding of vesicles. *Phys. Rev. Lett.*, 70:2964, 1993.
- [331] V. D. Gordon, X. Chen, J. W. Hutchinson, A. R. Bausch, M. Marquez, and D. A. Weitz. Self-assembled polymer membrane capsules inflated by osmotic pressure. *J. Am. Chem. Soc.*, 126:14117, 2004.
- [332] H. M. Wyss, T. Franke, E. Mele, and D. A. Weitz. Capillary micromechanics: Measuring the elasticity of microscopic soft objects. *Soft Matter*, 6:4550, 2010.
- [333] A. Fery, F. Dubreuil, and H. Mohwald. Mechanics of artificial microcapsules. *New J. Phys.*, 6:18, 2004.
- [334] W. T. S. Huck. Responsive polymers for nanoscale actuation. *Materials Today*, 11:24, 2008.
- [335] Z. Suo. Mechanics of stretchable electronics and soft machines. *MRS Bull.*, 37:218, 2012.
- [336] B. G. De Geest, S. De Koker, J. Demeester, S. C. De Smedt, and W. E. Hennink. Self-exploding capsules. *Polym. Chem.*, 1:137, 2010.
- [337] B. S. Kim and O. I. Vinogradova. pH-controlled swelling of polyelectrolyte multi-layer microcapsules. *J. Phys. Chem. B*, 108:8161, 2004.
- [338] K. Kohler, P. M. Biesheuvel, R. Weinkamer, H. Mohwald, and G. B. Sukhorukov. Salt-induced swelling-to-shrinking transition in polyelectrolyte multilayer capsules. *Phys. Rev. Lett.*, 97:188301, 2006.
- [339] A. S. Utada, E. Lorenceau, D. R. Link, P. D. Kaplan, H. A. Stone, and D. A. Weitz. Monodisperse double emulsions generated from a microcapillary device. *Science*, 308:537–541, 2005.
- [340] A. San Miguel, J. Scrimgeour, J. E. Curtis, and S. H. Behrens. Smart colloidosomes with a dissolution trigger. *Soft Matter*, 6:3163–3166, 2010.
- [341] S. S. Datta, H. C. Shum, and D. A. Weitz. Controlled buckling and crumpling of nanoparticle-coated droplets. *Langmuir*, 26:18612–18616, 2010.
- [342] J. Eisele, G. Haynes, and T. Rosamilia. Characterisation and toxicological behaviour of basic methacrylate copolymer for GRAS evaluation. *Regulatory Toxicology and Pharmacology*, 61:32–43, 2011.

Bibliography

- [343] R. I. Moustafine, I. M. Zaharov, and V. A. Kemenova. Physicochemical characterization and drug release properties of Eudragit E PO/Eudragit L 100-55 interpoly-electrolyte complexes. *European Journal of Pharmaceutics and Biopharmaceutics*, 63:26–36, 2006.
- [344] H. Liu, P. Wang, X. Zhang, F. Shen, and C. G. Gogos. Effects of extrusion process parameters on the dissolution behavior of indomethacin in Eudragit E PO solid dispersions. *Int. J. Pharmaceutics*, 383:161–169, 2010.
- [345] A. Abbaspourrad, S. S. Datta, and D. A. Weitz. Controlling release from pH-responsive microcapsules. *submitted*, 2013.
- [346] A. Siber and R. Podgornik. Role of electrostatic interactions in the assembly of empty spherical viral capsids. *Phys. Rev. E*, 76:061906, 2007.
- [347] J. N. Israelachvili. *Intermolecular and surface forces*. Academic Press, 2011.
- [348] T. L. Anderson. *Fracture Mechanics: Fundamentals and Applications*. CRC Press, third edition, 2004.
- [349] W. K. Kegel and P. van der Schoot. Competing hydrophobic and screened-coulomb interactions in hepatitis B virus capsid assembly. *Biophys. J.*, 86:3905, 2004.
- [350] A. L. Bozic, A. Siber, and R. Podgornik. Electrostatic self-energy of a partially formed spherical shell in salt solution: Application to stability of tethered and fluid shells as models for viruses and vesicles. *Phys. Rev. E*, 83:041916, 2011.
- [351] M. D. Betterton and M. P. Brenner. Electrostatic edge instability of lipid membranes. *Phys. Rev. Lett.*, 82:1598, 1999.